POLITECNICO DI TORINO

I Facoltà di ingegneria

Master's Degree In

Biomedical Engineering

Master's Degree Thesis

Microstructural and technical constraints of drug infusion within the brain: a Diffusion MRI-based study

Relatore: Filippo Molinari

Correlatore: Antonella Castellano

Candidato: Nicolò Pecco

December 2019

Ringraziamenti

Vorrei ringraziare innanzitutto la dottoressa A. Castellano per avermi dato la possibilità di far parte di questo gruppo di ricerca e di svolgere la tesi di laurea in un'azienda di grande spessore. Ringrazio la mia famiglia che oltre ad avermi dato l'opportunità di studiare all'Università di Cagliari e al Politecnico di Torino mi hanno sempre sostenuto e aiutato non solo nel contesto universitario ma anche nella vita di tutti i giorni. Grazie a tutte le persone che mi sono state vicine sia fisicamente che mentalmente e che, in tutti questi anni, sono riuscite a darmi la carica per portare a termine questo bellissimo percorso.

Index

INTRODUCTION **7**

MRI AND DIFFUSION **9**

BASIC PRINCIPLES OF MRI 9
Contrast *16*
DIFFUSION PRINCIPLES 19
DIFFUSION IN MRI 21
Diffusion Tensor Imaging (DTI) *26*
TRACTOGRAPHY 31
ARTIFACTS 35
IMAGE PROCESSING 36
Correction of artifacts *37*
Image coregistration *37*

OVINE BRAIN ANATOMY **41**

CONVECTION ENHANCED DELIVERY (CED) **45**

PRINCIPLE OF OPERATION OF CED 45
CONSTRAINTS OF CED 46
Backflow *47*
Air bubbles *47*
Flow rate and Volume of distribution and infusion *48*
Visualization of volume distribution *48*
CLINICAL TRIALS EFFICACY EXPLOITING CED 49
PRECLINICAL TRIALS EXPLOITING CED: ASSESSMENT OF DRUG DISTRIBUTION 50

AIMS OF THE PROJECT **53**

MATERIALS AND METHODS **54**

STUDY POPULATION 54
EXPERIMENTAL SETTING: WORKFLOW 55
Experimental procedure *55*
Post-infusion image pre-processing *60*
Post-infusion image analyses *67*
STATISTICAL ANALYSIS 72

RESULTS **73**

AUTOMATIC SEGMENTATION AND INCLUSION CRITERIA 73
FINAL DATASET 75
INFUSATE DISTRIBUTIONS WITHIN WHITE MATTER FIBERS 78
EFFECTS OF CATHETER POSITIONING ON INFUSATE DISTRIBUTIONS 79
OFF-TARGET INFUSIONS 85

DISCUSSION **87**

CONCLUSION **91**

REFERENCES **92**

Introduction

The main obstacle for the focal delivery of systemic therapeutic agents within the brain is due to the natural defense of the brain. Particularly, the brain's vascular system called Blood-Brain-Barrier (BBB) keeps various substances found in the bloodstream out of the brain parenchyma while being permeable to substances essential to metabolic function such as O_2, CO_2 and hormones. The BBB is composed of several cell types, in particular the presence of astrocytic peduncle and pericyte outside the endothelial cells and the tight junctions between endothelial cells give to the BBB the role of protective barrier hindering the entry of most drugs in the cerebral parenchyma. However, the BBB can be bypassed with different local drug delivery techniques that have been developed in order to increase local drug concentration without increasing systemic side effects. Among these, a promising technique in the field of local delivery is the *convection enhanced delivery* (CED), developed in the early 1990s by Edward Oldfield et al. [3].

CED is an infusion technique which exploit a pressure-driven infusion, representing an innovative approach for personalized treatment and it is effective in bypassing the blood-brain barrier through specialized catheters placed by a neurosurgical procedure directly within the brain tissue [3]. However, confirmatory evidence of CED efficacy in clinics is still scarce, due to haphazard catheter positioning, unsuitable protocols, and inaccurate prediction of drug distribution [26]. The latter may be affected by catheter geometry and placement, infusions parameters and underlying tissue microstructure.

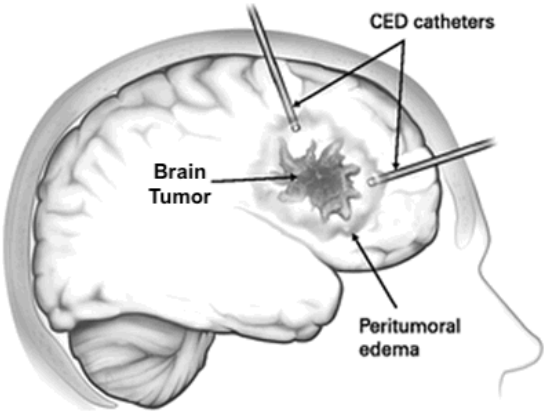

Figure 1. The surgeon inserts one or more catheters through bur holes into the interstitial spaces of the brain. A pressure gradient is generated using an infusion pump, and the agent displaces extracellular fluid after being directly infused into the extracellular space. The tumor is often highly vascularized, and this, as well as a number of factors, can affect the delivery of the infusate (white matter vs *gray matter, backflow, etc.) [158].*

This project was aimed to study the distribution of a known infusate at consecutive timepoints and its comparison to microstructural properties as depicted by DTI, demonstrating the impact of brain tissue features and catheter positioning on drug distribution *in vivo* during CED approach in brain ovine models.

This thesis project has been carried out during an internship at the Department of Neuroradiology at IRCCS San Raffaele Hospital and Vita-Salute San Raffaele University, Milan, in collaboration with the Faculty of Veterinary Science, the University of Milan, the Department of Electronics, Information and Bioengineering, the Politecnico di Milano, and Fondazione La Cittadina Studi e Ricerche Veterinarie, in Romanengo (LO) which allowed all the experiments and the acquisition of Magnetic Resonance Imaging (MRI) studies on a dedicated 1.5T scanner. The thesis is focused on a fraction of the EU's Horizon EDEN2020 (Enhanced Delivery Ecosystem for Neurosurgery in 2020) project.

MRI and Diffusion

The phenomenon of diffusion was noticed in 1827 by the British botanist Robert Brown, who was the first to report the random motions of pollen grains while studying them under the microscope. Diffusion represents a fundamental physical process for the normal functioning of most biological systems and has been studied for decades, allowing to investigate the structure and physiology of living cells. Human tissues are mostly composed of liquid components and finely regulated by an innumerable number of processes in which water diffusion plays a fundamental role, for example transport of enzymes, metabolic substrates and metabolites. The diffusion of water molecules is not completely free but hindered and restricted as it will be explained later in this chapter. The *in vivo* measurement of natural displacements of water molecules that occur within biological tissues as part of the physical diffusion process is possible by using Magnetic Resonance Imaging techniques. As such, after a brief introduction on the basic principles of MRI, this chapter will focus on the use of Diffusion MRI to depict the complex structural organization of the brain tissue. Brain tissue is composed by neuronal cells and myelin sheaths, which significantly affect the diffusion of water within the tissue. Different type of water diffusion within the nervous tissue are highly related to the structural organization of brain tissue, in particular to the structural difference between gray matter (GM), containing neuronal cell bodies, white matter (WM), containing myelinated axonal processes, and cerebrospinal fluid (CSF).

Basic principles of MRI

Magnetic resonance (MR) is a non-invasive imaging technology that produces three dimensional image by examining atoms and molecules within the body. It is based upon the interaction between an applied magnetic field and a particle that possesses spin and charge. The use of MR techniques for studying nuclear spin is formally known as Nuclear Magnetic Resonance, or NMR. Nuclear spin, or more precisely nuclear spin angular momentum, is one of several intrinsic properties of an atom and its value depends on the precise atomic composition. Magnetic resonance imaging (MRI) is based on the NMR signal of nucleus of the hydrogen atom (^{1}H) or, more precisely, on the positively charged proton contained in the hydrogen nucleus [133]. The human body is made up of about 65% water molecules comprising

two hydrogen atoms each. The high concentration of water molecules in biological tissues, particularly in soft tissues, allows to exploit the magnetic energy of hydrogen protons for the recognition of tissues that cannot be distinguished with other diagnostic equipment [133]. Each atomic nucleus is associated with a spin characterized by its own angular momentum or spin momentum $\vec{I}$. Hydrogen exhibits two opposite spin momentum which modulus is defined as 'I' and the relative energy levels are $(2I + 1)$ (Fig.2).

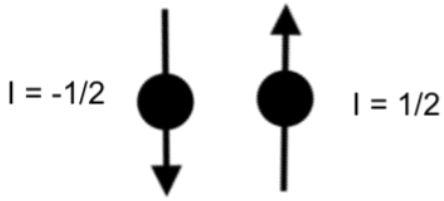

Figure 2. Spin number and their relative orientation referred to the Hydrogen proton.

However, if the number of protons and neutrons inside the nucleus are equal, the spin moment is equal to zero [134]. On the contrary, if the number of protons and neutrons inside the nucleus are different, the magnetic moment (1) can be defined as:

$$\vec{\mu} = \gamma * \vec{I} \qquad (1)$$

Where γ [MHz/T] is the gyromagnetic ratio, defined as the amount of magnetic field produced per revolution of the proton. The gyromagnetic ratio of the hydrogen atom has the highest values if compared with other elements within the human body (42.57 MHz/T) [130]. In the absence of an external magnetic field, the single magnetic moment of hydrogen atoms are randomly oriented in space, producing a sum vector, called 'Net magnetization vector' ($\vec{M}$). In this case $\vec{M}$ is equal to zero (Fig.3).

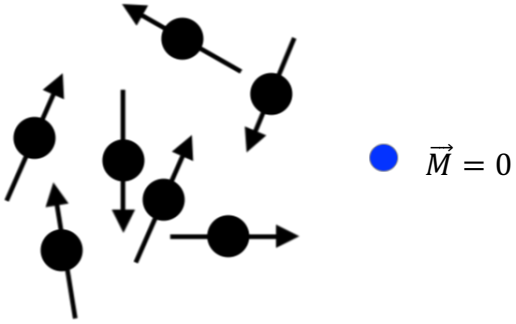

Figure 3. Net magnetization vector (blue dot) with modulus equal to zero in the absence of external magnetic field.

Conversely, when a tissue is placed inside a constant and homogeneous magnetic field, called static magnetic field (B_0) and always directed towards the Z axis of the MR scanner reference system, all magnetic moments tend to align in the direction of B_0. In this case $\vec{M}$ modulus will be greater than zero because the matter has been magnetized. The modulus of the net magnetization $\vec{M}_0$ vector does not depend only on B_0 but also on the water content within the tissue (proton density), which may be different across tissues.

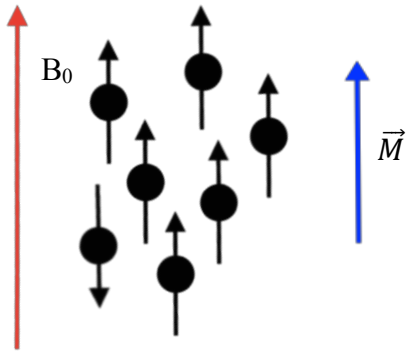

Figure 4. Net magnetization vector (blue arrow) with modulus greater than zero in the presence of external magnetic field B_0.

Protons magnetic moments have the same direction, but different orientations due to the opposite energy levels of hydrogen protons. These two configurations are described in terms of energy levels, indeed the orientation parallel to B_0 is the energy level with the lowest energy (spin-up), while the anti-parallel verse to B_0 is the one with the highest energy (spin-down). Consequently, the number of magnetic moments processing in spin-up is greater than the number of magnetic moments in spin-down direction, being spin-up the energy level with the lowest energy. This greater number of protons in spin-up direction is called 'prevalence'.

In the presence of the external, static magnetic field B_0, the individual protons also begin to rotate perpendicular to, or precess about, the magnetic field. The spin vectors for the protons are tilted slightly away from the axis of the magnetic field, but each axis of precession is parallel to the main axis of B_0. This precession is at a constant rate and occurs because of the interaction of the magnetic field with the spinning positive charge of the nucleus (Fig. 5).

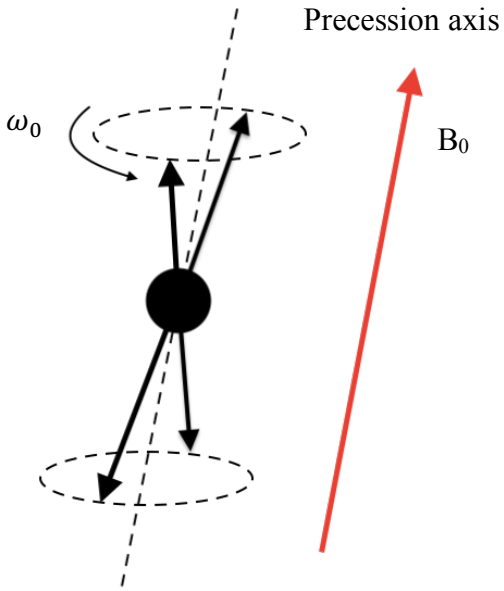

Figure 5. In the presence of B_0 magnetic field protons spin rotate around one parallel axes of B_0 with a precession frequency equal to ω_0 (Larmor's frequency).

The procession frequency is proportional to the strength of the magnetic field and is expressed by the following equation, known as the 'Larmor equation' [130]:

$$\omega_0 = \gamma * B_0 \qquad (2)$$

The only presence of B_0 forces the magnetization vector to have only the component along the z axis and no component in the xy plane. The manipulation of the net magnetization M_0 with the application of a short burst, or pulse, of radiofrequency (RF) energy allows to obtain the MR signal. In particular, RF is activated together with another gradient (called 'Slice selective gradient'), that allowed to gives energy only to protons in a particular space region (slice). RF pulse, referred to as an excitation pulse, typically contains a narrow range or bandwidth of frequencies centered around a central frequency. During the pulse, the protons absorb a portion of this energy at a particular frequency that is proportional to the magnetic field B_0; the equation relating the two is the Larmor equation, equation (2). In a rotating frame of reference, the RF pulse broadcast at the resonant frequency ω_0 can be treated as an additional magnetic field B_1 oriented perpendicular to B_0. Once B_1 is switched on, protons are brought to the highest energy level (spin-down orientation), maintaining phase coherence and a constant precession motion at the frequency ω_0. The amount of resulting rotation of $\vec{M}$ is known as the pulse flip angle. If

the RF transmitter is left on long enough and at a high enough amplitude, the absorbed energy causes M_0 to rotate entirely into the transverse plane, a result known as a 90° pulse [130].

When the RF transmitter is turned off, the protons immediately begin to realign themselves and return to their original equilibrium orientation. They reemit energy at the same Larmor frequency ω_0 as they do so. In addition, the net magnetization will begin to precess about B_0 similar to the behavior of a gyroscope when tilted away from a vertical axis (Fig.6). If a loop of wire (receiver) is placed perpendicular to the transverse plane, M_0 will induce a voltage in the wire during its precession. This induced voltage, the MR signal, is known as the FID, or free induction decay (see below).

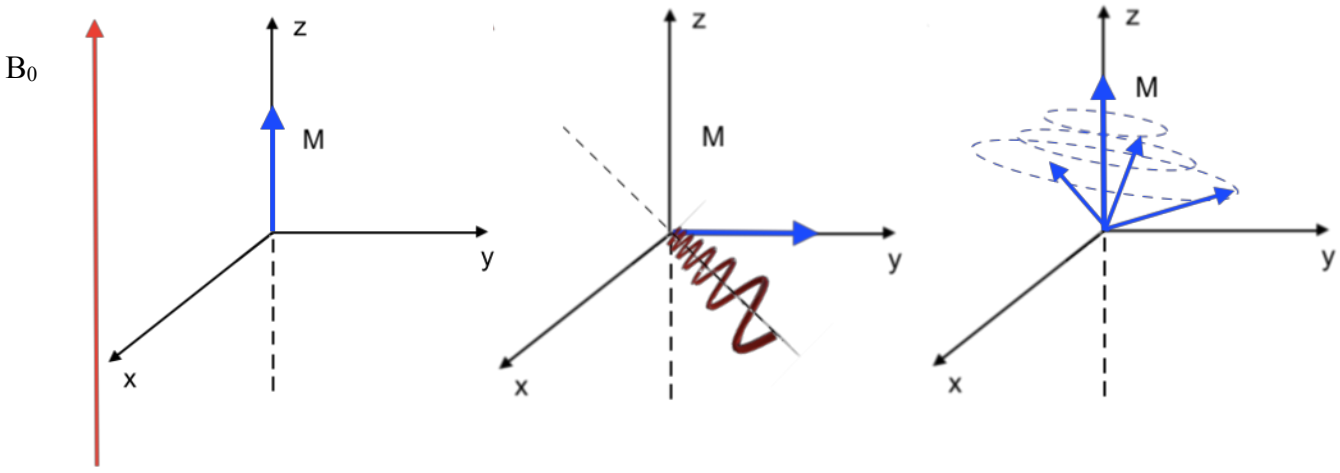

Figure 6. Proton resonance mechanism: On the right the vector starts from a situation parallel to the z axis, B_0 on and B_1 off. In the middle, the RF is turned on long enough and at a high enough amplitude to rotate the magnetization vector on the xy plane. On the left the spiral trajectory of the net magnetization when returning to the original equilibrium orientation when the RF pulse is turned off..

The process by which the protons release the energy that they absorbed from the RF pulse is known as relaxation. Relaxation is a time-dependent process and is characterized by a rate constant known as the relaxation time. Two relaxation times can be measured, known as T1 and T2 [136]:

- The relaxation time T1 is the time required for the z component of net magnetization to return to 63% of its original value following an excitation pulse [133]. It is also known as the spin-lattice relaxation time or longitudinal relaxation time. The term spin-lattice refers to the fact that the excited proton ("spin") transfers its energy to its surroundings ("lattice") rather than to another proton. The energy absorbed by the protons during the RF excitation is thus exchanged

with the surrounding tissues until its depletion. T1 therefore results in the restoration of $\vec{M}$ in the z direction, called longitudinal component ($\overrightarrow{M_{long.}}$).

- The relaxation time T2 is the time required for the transverse component of net magnetization to decay to 37% of its initial value. It is also known as the spin–spin relaxation time or transverse relaxation time. Spin–spin relaxation refers to this energy transfer from an excited proton to another nearby proton until it is dispersed; the T2 time is therefore relative to the transverse component of $\vec{M}$ ($\overrightarrow{M_{trasv.}}$). When the RF pulse is active, all the protons present a phase coherence. When the RF pulse is turned off, protons begin to exchange energy between them; furthermore, intermolecular and intramolecular interactions such as vibrations or rotations cause transient fluctuations in the magnetic field and thus cause ω_0 to fluctuate. This fluctuation produces a gradual, irreversible loss of phase coherence to the spins as they exchange the energy and reduce the magnitude of the transverse magnetization and the generated signal. Thus, the module of $\overrightarrow{M_{trasv.}}$ tends to zero as a result of the loss of phase coherence (Fig. 8).

The abovementioned loss of phase coherence is essentially due to two factors, the intrinsic properties of the tissue (T2) and external factors such as the nonuniformity of B_0 or static magnetic field inhomogeneity [135]. The combination of the T2 timing, due only to the spin-spin phenomenon, and magnetic field inhomogeneity leads to the appearance of a new time called T2* which represents the total transverse relaxation time that is actually measured. The relation between the relaxation times is therefore the following:

$$T2^* \leq T2 \leq T1$$

In Fig. 10 is shown the decay of the magnetization vector in its two components, following the shutdown of the variable magnetic field B_1, after a 90° RF pulse. The $\overrightarrow{M_{trasv.}}$ reaches zero faster than the recovery of $\overrightarrow{M_{long.}}$ in the longitudinal plane [132].

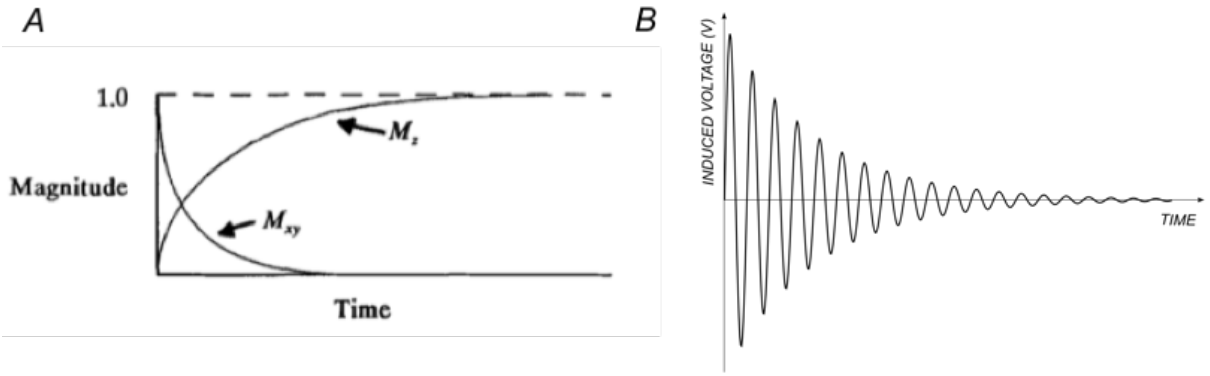

Figure 7. A) Time-course of the two components of the net magnetization vectors [132] and B) Time-course of the FID signal .

As previously mentioned, the induced voltage on the receiver recorded during the relaxation phase of the net magnetization vector M_0 (Fig.6) is called FID (free induction decay). The relaxation times T1 and T2 simultaneously govern the decay of the FID signal (Fig.7) according to the following relation:

$$A_{FID} = DP * e^{-\frac{t}{T1}} * e^{-\frac{t}{T2}} \quad (5)$$

Where DP is the proton density. The ability to discriminate tissues lies in the ability to favor one time constant over the other and this is done by using a specific 'sequence' of RF pulses.

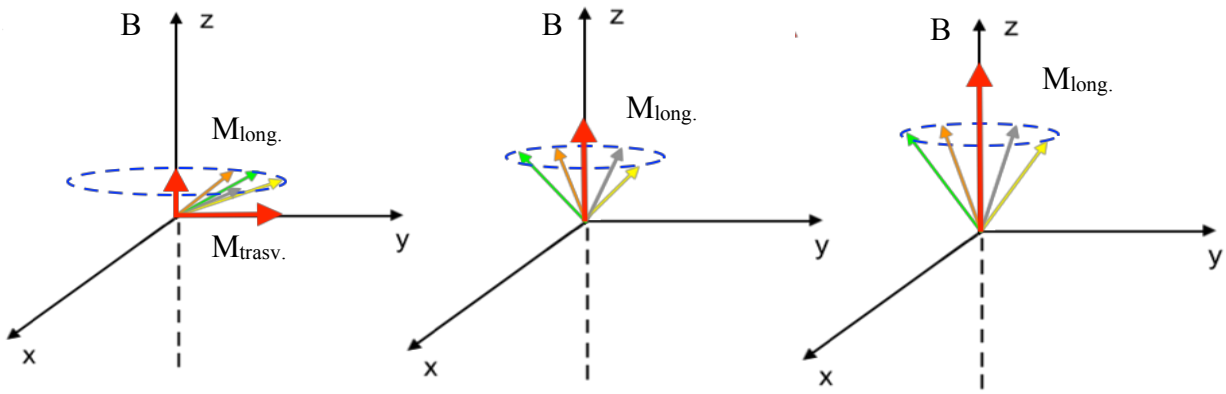

Figure 8. Different magnetic moments (orange, green, yellow ,gray) which sum in the z direction is Mlong while sum in the xy plane is Mtrasv representing T1 and T2 relaxation mechanism. On the right, the vector is projected on the xy plane and on the z axis. The relaxation time T1 is greater than the relaxation time T2.

Longitudinal and transverse relaxation are independent phenomena that happen simultaneously. Thus, images will have a *predominant* T1 or T2 weighting according to the different intervals between successive RF pulses. In order to emphasize one mechanism of relaxation with respect to another, pulse sequences are used in order to acquire specific FID. There are different types of sequences differentiated according to the activation times of B_1, acquisition time or echo time of the FID (TE), repetition time of the pulse sequence (TR). Before FID acquisition, however, it is necessary to choose the reference slice and encode the signal in phase and frequency in order to obtain information regarding the spatial position of the received information. The time data related to FID signals is inserted in a numerical matrix with different filling techniques, and this matrix is called k-space. A subsequent 2D Fourier transform (2DFT) applied to the k-space produces the final image. Further information about magnetic gradients, k-space and different acquisition sequences are not the subject of this thesis.

Contrast

MRI contrast can be chosen by employing one particular sequence. However, as mentioned above, it is not possible to obtain a single T1, T2 or DP weighted-image without a minimum contrast related to the other two parameters [137]. The factors involved in changing the image contrast are TR, TE, flip angle, while constant parameters are T1, T2 and DP and they depend on the tissue proprieties.

The use of a short TR and TE (ms) provides image-weightings more dependent on the T1 time constant of the tissues under examination [139]. When TE is short, differences in signal intensity due to differences in T2 have not had enough time to become pronounced yet, in other words relaxation phenomena have not decrease the magnetization vector yet, which will be read with almost the same amplitude it had before the RF excitation pulse. Likewise, with a short TR, tissues have not recovered their longitudinal magnetization, thus differences in T1 will show up in form of signal intensity differences (Fig.9). The combination of short TE and TR allows to weight the image with a predominant T1 contrast weighting of the involved tissues, in particular white matter, gray matter and the CSF. Angle $\alpha \leq 90°$ can be used to preserve the longitudinal component even after several TRs.

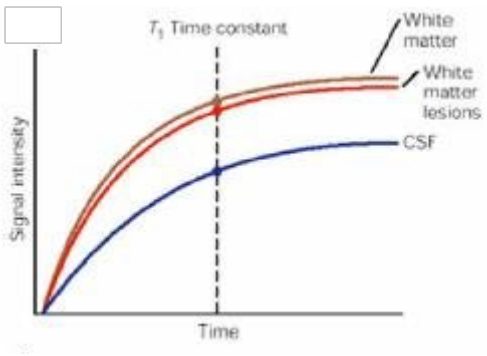

Figure 9. Spin-lattice relaxation time curse after 90° RF pulse. Short TE allows to obtain contrast predominantly weighted in T1 [74].

Longer TR (2-3 s), associated with a short TE, will make the contrast largely depend on the DP of the tissues under examination. In fact, the relatively short TE prevents T2-dependent phenomena to start, while the longer TR allows sufficient time for the longitudinal magnetizations of the voxels to recover almost totally until its maximum value, that is proportional to the proton density of the tissue [138]. A sufficiently long TR will avoid the effects of T1 relaxation, allowing the tissue to recover much of the longitudinal magnetization, while long TR and long TE will allow transverse magnetization to decay for T2-dependent effects, and the contrast will depend mainly on T2.

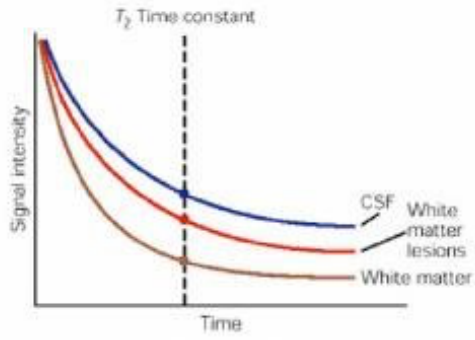

Figure 10. Spin-spin relaxation time course after 90° RF pulse. Long TR and TE allows to obtain contrast predominantly T2-weighted [74].

Short TR associated with long TE are not used due to the very low SNR: the short TR allows very short time for longitudinal magnetization to recover. Therefore, the successive 90° pulse further reduces the limited recovered part of the magnetization vector.

The contrast variations that can be obtained by setting the parameters explained before are showed in Fig.11, where the same brain cross-section is represented with proton density (PD), T2-weighted and T1-weighted contrast.

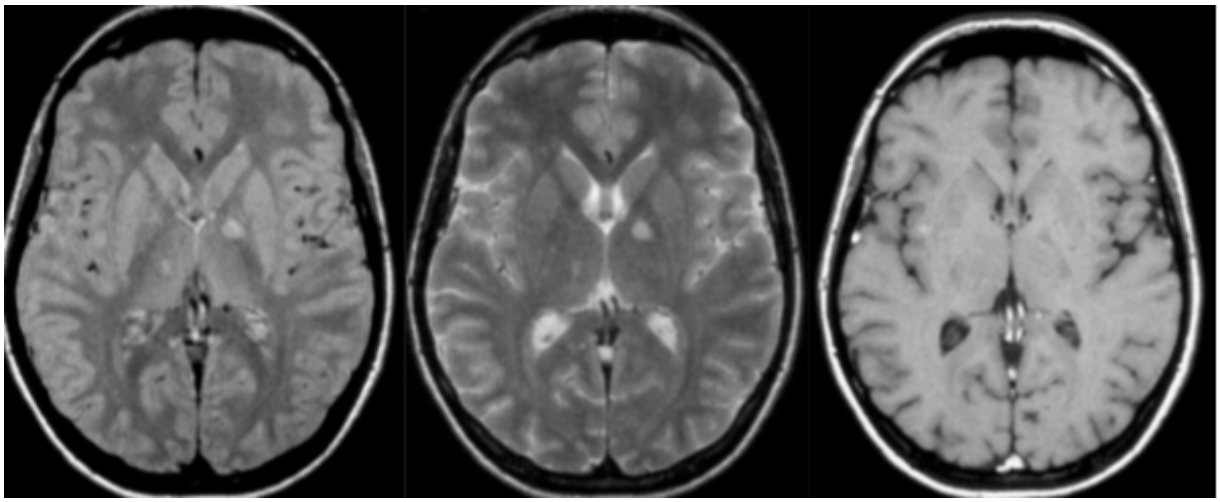

Figure 11. From right to left images weighted in DP, T2 e T1 respectively.

Contrast media

Contrast media are often used in MRI to discriminate tissues or organs that normally have very similar relaxation times and thus are not distinguishable on MR images.
Contrast media are paramagnetic substances having small local magnetic fields, which cause a shortening of the relaxation times of the protons in their neighborhood. Indeed, they modify the proton precession frequency by acting on the nearby magnetic fields [140]. The most used MRI contrast medium is Gadolinium (Gd), which has unpaired electrons and therefore a negative charge. When Gadolinium and protons are sufficiently close (≤ 3 Å[1]), the probability of spin-reticulum relaxation increases and shortening of the time constant T1 is obtained.
Contrast media also exhibit magnetic susceptibility behavior, in particular, paramagnetic materials produce an additional magnetic field of modulus in the range $[10^{-5},10^{-3}]$, while diamagnetic materials produce a negative magnetic field of modulus $[-10^{-6},-10^{-5}]$. Defining magnetic susceptibility with χ, the new protons frequency of precession due to the contrast agents will be:

[1] Angstrom (Å); 1 Å = 10^{7} millimiters.

$$\omega_{cont.} = \gamma * B_0 * (1 + \chi) \quad (8)$$

Equation (8) illustrates how contrast agents magnetic susceptibility influences the protons precession frequency of an infinitesimal amount.

Diffusion principles

Diffusion process is due to the motion of atoms, molecules or microparticles caused by their own thermal energy, which determines chaotic movements also known as Brownian motions. Being a random motion, the velocity vectors sum of each element is close to zero, unless there is an "external force".

The external force is a physical quantity and can be of various nature, for example it can be represented by a pressure difference (pressure gradient) which, as it will explained in the chapter dedicated to the 'CED', is one of the basic principles of some local delivery techniques. The application of an external force determines an effective transport of material, i.e. an oriented movement of the atoms, molecules or microparticles and no longer random as in the Brownian diffusion case. Diffusion is governed by a concentration difference and it is described by Fick's law which states that the solute flow between two surfaces is proportional to the difference in concentration between the surfaces and inversely proportional to their distance according to a proportionality factor D, called diffusion coefficient.

$$\mathrm{J} = -\mathrm{D} * \nabla \mathrm{C} \quad (9)$$

Diffusion coefficient is a function of temperature, physical and chemical characteristics (viscosity, molecular weight) of both solvent and solute, and expresses the speed at which the solute molecular concentration changes over time.

The considerations made so far about the diffusion of the solute in the solvent are equally valid when considering the spontaneous motions that occur in a pure liquid or gaseous solvent even in the absence of concentration gradients. This is the case with the movement of water molecules within biological tissues. In this regard, in 1905 Albert Einstein demonstrated that Brownian motion and diffusion could be identified as substantially the

same phenomenon whose cause is the thermal agitation of the molecules. Einstein's model of Brownian motion in known as a random walk formalization [141]. Einstein proved a direct proportionality between mean square displacement of particles and time, corrected by a factor D (Diffusion coefficient); mean square displacement takes a Gaussian distribution centered on zero (average displacement equal to zero). This relationship, in the three-dimensional case, is given by:

$$\bar{x}^2 = 6Dt \tag{10}$$

That is:

$$|x| = \sqrt{6Dt} \tag{11}$$

Relation (11) indicates that in a random walk the displacement of molecules is a linear function of the square root of time, therefore the knowledge of x for a determined diffusion time t allows to obtain D. D is a constant depending only on the size (mass) of the molecules, the temperature and the nature (viscosity) of the medium. For example, in the case of 'free' water molecules diffusing in water at 37 °C, the diffusion coefficient is 3×10^{-9} m^2/s, which translates to a diffusion distance of 17 μm during 50 ms [142].

MRI provides a unique probe to noninvasively quantify the diffusional characteristics of water molecules *in vivo*, as explained in the next paragraph. However, during typical diffusion times of about 50-100 ms, water molecules move in brain tissues bouncing off, crossing or interacting with many tissue components, such as cell membranes, fibers and macromolecules. Because the movement of water molecules is impeded by such obstacles, the actual diffusion distance is reduced with respect to the free water, and the displacement distribution is no longer Gaussian. In other words, the Brownian motion of extracellular water molecules may be hindered by biological obstacles such as cells, and inside each cell, diffusion may be restricted by the cellular membranes. Thus, the non-invasive observation of the water diffusion-driven displacement distributions in vivo provides unique clues to the fine structural features and geometric organization of neural tissues, and also to changes in these features with physiological and pathological states.

Diffusion in MRI

Although early water diffusion measurements were made in biological tissues using NMR in the 1960s [48] original diffusion-weighted MR imaging of *in vivo* systems was initially performed in the mid-1980s [34,143]. Basically, MRI is able to measure water diffusivity by modifying T2-weighted spin-echo sequences through the use of a pair of magnetic field gradient pulses, the duration and the separation of which can be adjusted, with echo-planar readouts of the data [46].

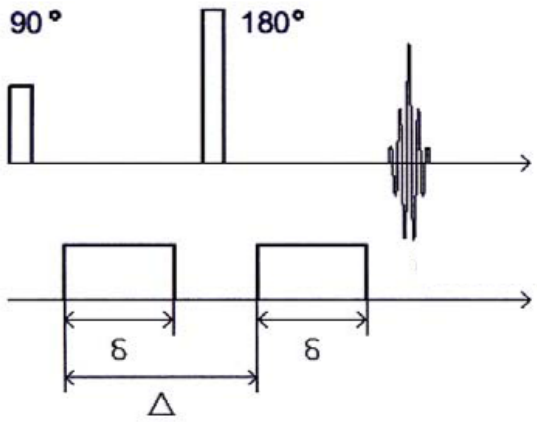

Figure 12. Schematic representation of the DWI pulsed gradient sequence.

Paired magnetic field gradient pulses serve to *encode* initial locations of water molecules' protons within a medium. That is, the first pulse magnetically 'labels' protons that are carried by water molecules according to their spatial location, as, for a short time, the magnetic field slowly varies along the gradient direction. The second pulse is introduced slightly later (typically after tens of milliseconds) to detect the changes in the location of protons; that is, the displacement of the protons that occurred during the time interval (or 'diffusion time') between the two pulses. As an example, if a proton has speed equal to zero, the proton's phase accumulation due to the first gradient pulse will be exactly the same in module but opposite in sign in respect to the second gradient pulse application due to the effect of the 180° interposed RF pulse (Fig. 12). Therefore, independently from the position, protons fixed in the position x_0 (linked, for example, to a macromolecule) will undergo a net phase change equal to zero. Protons moving along the gradient direction will receive different pulse amplitude during the application of the two consecutive gradient pulses. Therefore, proton spin will not be exactly back in phase with the other spin causing loss of coherence that results in signal amplitude attenuation, which is proportional to the displacement. Indeed, water molecules interact with

the gradient and consequently the phase (φ) of their spin, accumulated in the time interval t during which it travels the distance x, takes the value:

$$\varphi_{x(t)} = \int_0^t \omega \, dt = \int_0^t (\gamma B_0 + \gamma G_x x) dt \tag{12}$$

The phase change and the consequent signal loss is the fundamental principle behind Diffusion-Weighted Imaging (DWI), in particular the greater the displacement between the two pulses, the greater the attenuation of the signal. Highly mobile molecules tend to lose signal, whereas immobile ones yield relatively strong signal on diffusion-weighted sequences. In particular, equation (11) proved that the displacement in a given time interval depends on the diffusion coefficient. Accordingly, signal loss will be influenced only by the value of D and will be greater if the diffusion coefficient increases. In particular, it can be demonstrated that signal loss is an exponential function of D:

$$S_i = S_0 e^{-bD} \tag{13}$$

where S_0 is the signal in the absence of the diffusion-sensitized gradients, S_i is the signal in the presence of the diffusion-sensitizing gradients and the factor *b* is the *'b-value'* which indicates the diffusion-weighting of the image and is a function of the strength and duration of the diffusion-sensitizing gradients. Considering the simplified version where $\Delta \gg \delta$:

$$b = (\gamma * G_x * \delta)^2 * \Delta \tag{14}$$

where G_x represents the gradient intensity (mT/mm), δ its duration (sec.) and Δ the time interval (sec.) between the two gradients (Fig.12). Generally, a range of b values (2 or more) is used in a diffusion MRI study to interrogate the water diffusion properties of tissues. Typically, the b-values used in clinics for diffusion-weighted sequences are between 800 and 1500 s/mm^2 [75]. Since the *b-value* depends on the square of the gradient intensity, it is essential to have MRI equipment capable of providing high intensity gradients to acquire diffusion-weighted sequences. In general, magnetic field gradients of at least 20 mTm^{-1} and with extremely fast *slew rate* are required. Consequently, the echo time will increase and, as explained in the paragraph 'Contrast', this determine a T2-weighting of the images. As such, diffusion-weighted

images DW images will be both diffusion- and T2-weighted, an effect known as "T2-shine through" [32,33]. To reduce this effect, it is necessary to acquire a further image just T2-weighted in the absence of diffusion sensitizing gradients (*b-value*=0 s/mm^2) and leaving the other parameters unchanged. The signal of this diffusion-weighted signal image is divided from the b_0 image, allowing to have a quantitative estimation of diffusion in each voxel [34].

The degree of signal loss at various *b-values* allows to calculate molecular mobility in the medium, that is, the diffusion coefficient is precisely measurable in simple fluids. However, in complex systems such as biological tissues made of multiple intra- and extracellular compartments separated by semi-permeable membranes, the overall signal observed in a diffusion-weighted image voxel, at a millimetric resolution, results from the integration, on a statistical basis, of all the microscopic displacement distributions of the water molecules present in that voxel. In this scenario the concept of a single diffusion coefficient is no longer valid. Thus, when performing diffusion-sensitive sequences on biological tissues we quantify an "apparent diffusion coefficient" (ADC) [34], usually measured in mm^2/s, since the "true" value of D refers to the so-called "free" water, meaning water that spreads freely into tissue, and depends only on temperature and molecular weight.

Conversely, diffusion in biological systems is influenced not only by temperature, but also by other factors such as macromolecular bonds that reduces the mobility of water, the presence of hydrophobic barriers (cellular membranes, mitochondria, myelin sheaths) that limit free diffusion, as well as the structural characteristics of cells (size, presence of organelles and other membrane-lined structures) [35]. As explained above, by acquiring at least two images at different b-values and keeping constant the TE, it is possible to quantify the average ADC value for each single voxel without any presence of the T2-weighting; assigning a gray scale to the interval of the ADC values the so-called Apparent Diffusion Coefficient map is obtained [36], where the ADC in each voxel is calculated as follows:

$$\mathrm{ADC}_i = -\frac{\ln\left(\frac{\mathrm{S_i}}{\mathrm{S_0}}\right)}{\mathrm{b}} \tag{15}$$

In Fig.13 diffusion gradient is applied in a particular direction, so the sequence will be sensitized to the diffusion in that direction.

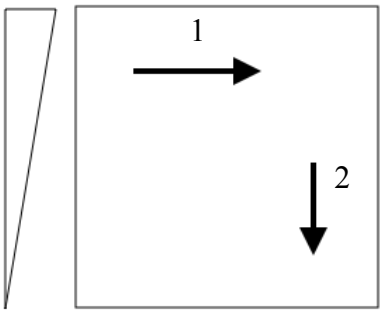

Figure 13. Diffusion gradient application along the vertical direction. The signal loss is verified in water molecules whose displacement is not orthogonal to the direction of application of the gradient.

The fiber bundles with parallel course (2) to the gradient will present a maximum signal loss, while the effect will be minimal when the gradient is applied orthogonal to their course (1). This is because the phase does not change when the gradient is constant in a given line or a given spatial plane, according to equation (12).

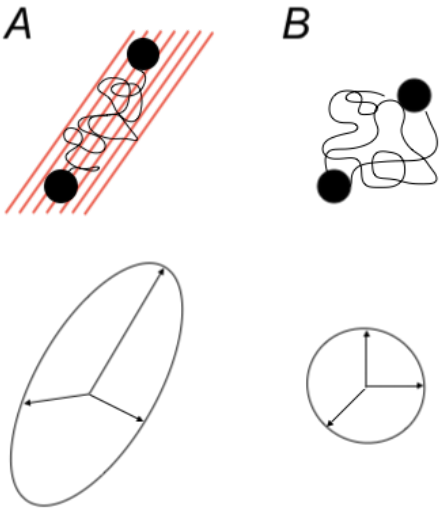

Figure 14. A) Anisotropic diffusion and its relative diffusion ellipsoid; B) Isotropic diffusion and its relative diffusion sphere.

Moreover, water diffusion can be uniformly distributed in the three orthogonal planes of space, and this diffusion is called *isotropic*; in this case, in a given time interval, the molecules will distribute according to a spherical diffusion model, therefore the measured ADC will be basically the same in all directions (Fig.14B). Conversely, in the presence of highly *oriented* barriers, such as myelin sheaths surrounding axons, the diffusion of water molecules will be mainly facilitated in the spaces between membranes (parallel to the course of the axon) and limited through them (perpendicularly to the course of the axon) with consequent reduction of the diffusion; this diffusion is called *anisotropic*, and consequently the ADC measured along a

parallel axis to the myelinated fibers direction will be greater than that measured along its orthogonal axis (Fig. 14A). As such, equation (13) can be reformulated as following:

$$S_i = S_0 e^{-bADC} \tag{16}$$

In equation (16), the signal loss depends on the i-th gradient direction, therefore, in order to have images that are not dependent on the direction, DWI sequences are acquired along three perpendicular gradient directions and then images are averaged to give back the mean ADC.

$$S_{DWI} = S_0 e^{-bADC} = S_0 e^{-b\left(\frac{ADC_x + ADC_y + ADC_z}{3}\right)} = \sqrt[3]{S_1 + S_2 + S_3} \tag{17}$$

The different ADC values in various tissues reflect changes in cellularity, membrane permeability, intra- and extra-cellular diffusion and tissue structure.

Figure 15 shows different DWIs in which the attenuation of the intensity of the MRI signal depends directly on the amplitude of the molecular displacement along the direction of the applied gradient and on the intensity and duration of the gradient itself; the gradients are oriented in the three directions of space, orthogonal to each other.

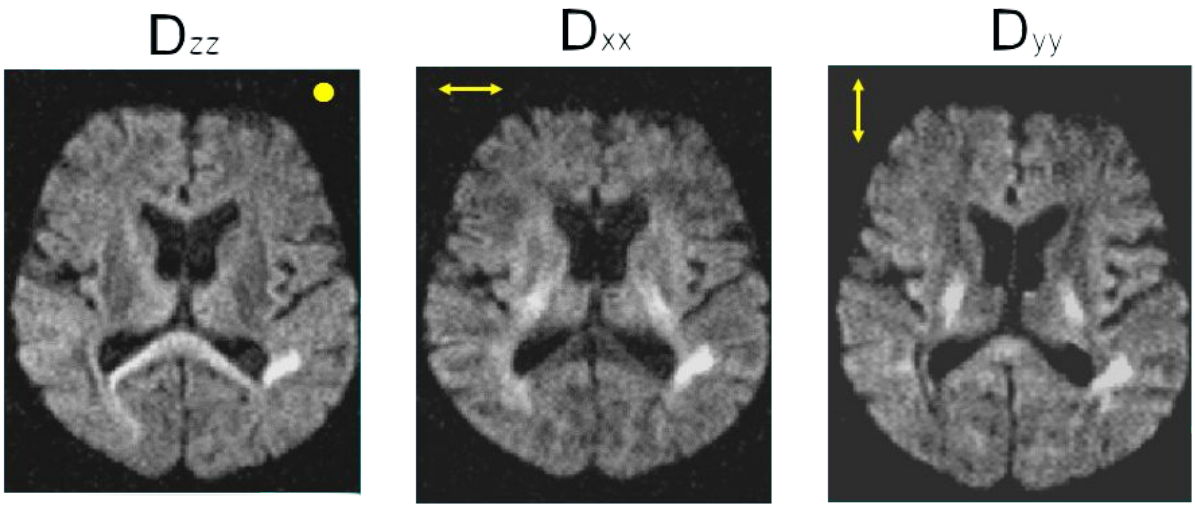

Figure 15. Diffusion-weighted images of the human brain acquired along three orthogonal gradient directions (Dxx,Dyy and Dzz).

Diffusion Tensor Imaging (DTI)

Diffusion within the human brain depends on the structure in which water molecules spread. Diffusion of water in the brain grey matter is isotropic and it is about 2.5 times lower than pure water at the same temperature; instead, diffusion in the cerebrospinal fluid (CSF) is similar to water diffusion [37]. In the brain white matter, the presence of intact axonal membranes influences the direction of water diffusion within fiber bundles, while the degree of myelinization, the diameter of the axon and the density of the fibers modulate the degree of anisotropy [38]. In general, three types of diffusion are recognized: free, restricted and hindered [120]. Free diffusion occurs when the molecules of the medium spreads without intercept any type of obstacle other than the solvent in which it spreads.

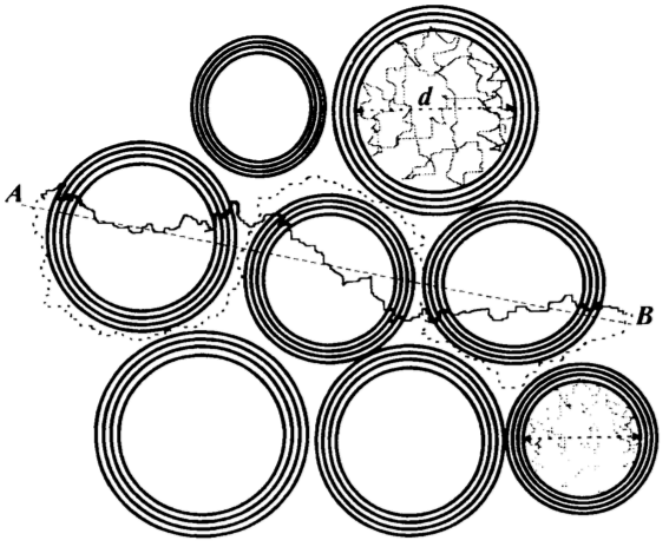

Figure 15. Restricted (d) and hindered (from A to B) diffusion in white matter [120]

As such, it can be deduced that ADC values measured along multiple directions allows to obtain important information about the WM structure and on the entire brain structure. In the case of an isotropic medium, the diffusion model is substantially spherical and characterized only by one ADC value, which represents the diameter of the sphere (Fig.16B); vice versa, in an oriented structure, such as the WM, the diffusion is no longer spherical, but it is better described by an ellipsoid, whose main axis is aligned to the direction along which the diffusion *hindrance* is lower, meaning that is along the major axis of the fibers (Fig.16A) [40].

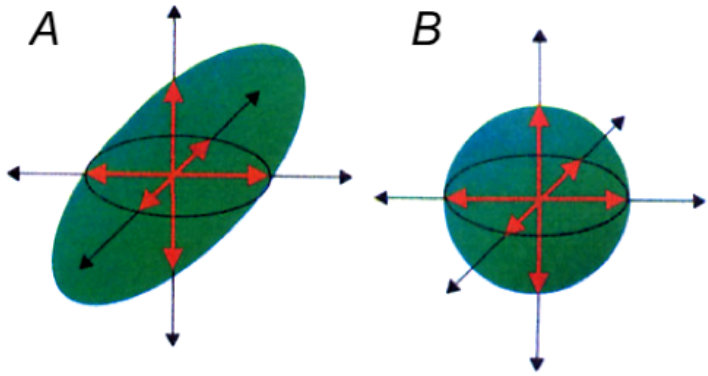

Figure 16. Example of diffusion measurements along three axes in an anisotropic (A) and isotropic (B) medium.

Diffusion anisotropy can be better evaluated by Diffusion Tensor MR Imaging (DTI), that allows to visualize the amount and the orientation of water diffusion within brain tissues [40]. In order to map anisotropy, diffusion sensitizing gradients must be applied along multiple non-collinear directions (at least six diffusion gradient axes), plus the mandatory b value=0 s/mm^2 to determine diffusion tensor elements, although, often, many more directions are sampled to improve tensor calculations. Indeed, the diffusion ellipsoid needs at least six parameters to be defined (Fig.17): three lengths λ_1, λ_2, λ_3, called *eigenvalues,* defining its shape, and three vectors ε_1, ε_2, ε_3, called *eigenvectors,* defining its orientation.

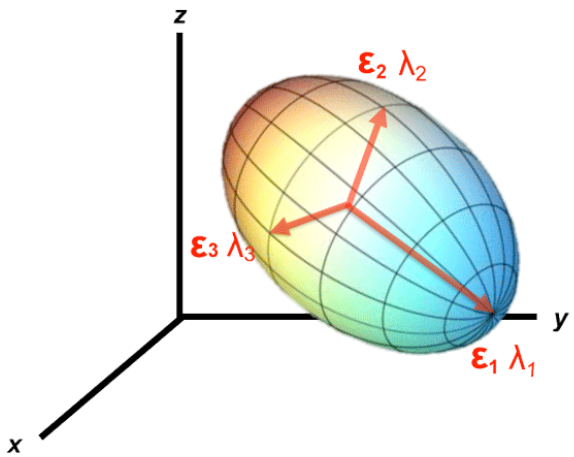

Figure 17. Graphical representation of the six parameters used to define the ellipsoid, namely eigenvalues and eigenvectors.

Therefore, 6 volumes are needed with b≠0 to identify the water diffusion ellipsoid within tissues (Fig.18) and one more volume without application of the gradient (b=0). These volumes are then mathematically elaborated to provide the shape (spherical or elliptical) and the space orientation.

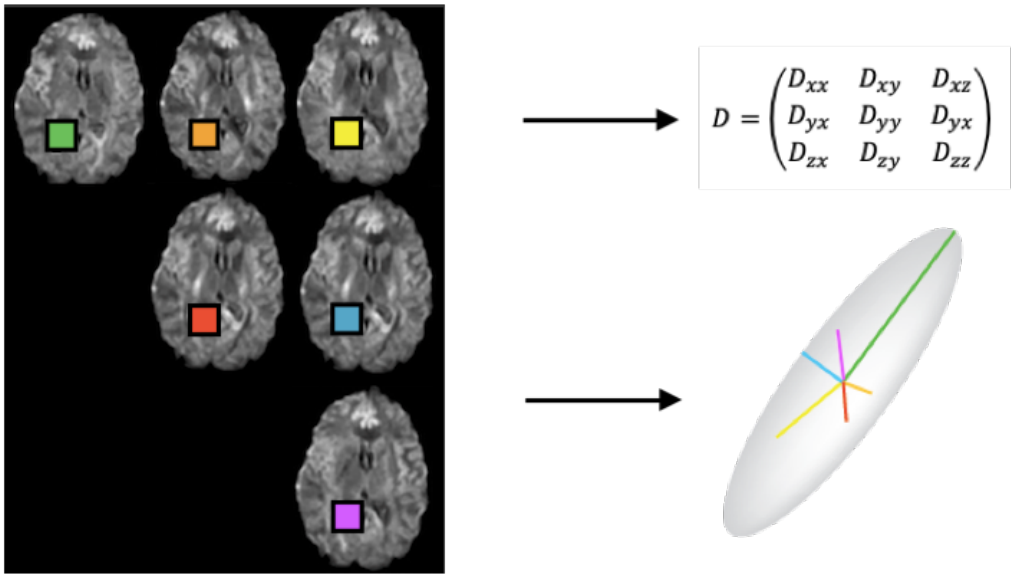

Figure 18. On the left the six DWI volumes with the i-th voxel highlighted. At the top right the respective tensor for that voxel and at the bottom right the representation of the direction module of the diffusion coefficients.

Tensor analysis allows to reconstruct the actual shape and orientation of the ellipsoid through a square matrix of size 3 called *diffusion tensor*. Mathematically, the diffusion tensor fully describes the mobility of the molecules in anisotropic systems [144-146]. The tensor analysis solves a set of equations obtained from equation (13) that are solved using linear algebra. Each voxel can then be represented with a diffusion tensor that contains the intensities relative to the different DWI acquired with different gradient orientations.

The diagonal elements D_{xx}, D_{yy}, D_{zz}, represent the molecular mobility in the three acquisition directions x, y, z, while the non-diagonal elements, such as D_{xy}, D_{xz}, D_{yz} reflect the correlations of the molecular displacement between the orthogonal directions. Since the diffusion tensor is symmetric ($D_{ij} = D_{ji}$), there are only six independent terms that configure the diffusion ellipsoid. A subsequent mathematical process, called matrix diagonalization, allows the x,y,z original coordinate system (acquisition reference system) to be rotated in a new reference system x ' y ' z ' where the axes coincide with the eigenvector directions. Therefore, the main vector is aligned with the main direction of the fibers. In particular, if the elements outside the diagonal matrix are equal to zero, the elements of the diagonal correspond to the eigenvalues. On the other hand, if they are different from zero the diagonalization process defined as follows shall be used:

$$(D - \lambda_i I)\varepsilon_i = 0 \qquad (19)$$

Expressed in matrix form as:

$$\begin{pmatrix} D_{xx} - \lambda_i & D_{xy} & D_{xz} \\ D_{yx} & D_{yy} - \lambda_i & D_{yx} \\ D_{zx} & D_{zy} & D_{zz} - \lambda_i \end{pmatrix} \begin{pmatrix} \varepsilon_{ix} \\ \varepsilon_{iy} \\ \varepsilon_{iz} \end{pmatrix} = \begin{pmatrix} 0 \\ 0 \\ 0 \end{pmatrix} \quad (20)$$

The non-trivial solutions for this set of equations are obtained by imposing determinant of the matrix $(D - \lambda_i I)$ equal to 0 [43]. The result is a 3rd order polynomial equal to the size of the matrix, whose solutions are the eigenvalues; The roots of the eigenvalues correspond to axes length. Afterwards, the three eigenvectors can be obtained from the equations system $(D - \lambda_i I)\varepsilon_i$ [39].

The eigenvalues (λ_1, λ_2, and λ_3) represent the diffusivities along directions of greatest structural anisotropy established by cytoarchitecture. Each eigenvalue is associated with an eigenvector (ε_1, ε_2, and ε_3), where the largest of the three eigenvalues (λ_1) corresponds to the eigenvector ε_1 and describes the principal direction of the diffusion at that point, that is, the direction along which molecules move most freely, that is aligned with the dominant orientation of the fibers in the voxel.

Fractional Anisotropy

Eigenvalues and eigenvectors allow to obtain different diffusion maps as well as anisotropy indexes: the usefulness of such maps is to provide a diffusion measurement independent on the acquisition directions (i.e. rotationally invariant). The simplest maps are the 'tensor trace', i.e. the sum of the three eigenvalues and the so-called mean diffusivity (MD) [39], i.e. the average of the three eigenvalues that is independent from the reference system. MD represents the mean mobility of water molecules in the studied tissue, averaged over all the directions, reflects the size of the diffusion ellipsoid and has the dimension of a diffusion coefficient (mm^2/s).

Anisotropy is usually represented by the fractional anisotropy (FA) [40], which is largely exploited in this thesis. FA is a measure of anisotropic diffusion weighted against total diffusion, thus representing the degree of anisotropy (i.e. how greater is diffusivity in the main direction than in the others). As such, FA represents an estimate of the anisotropy of white matter bundles. FA can be imagined as the difference between the ellipsoid and sphere shape and is mathematically defined as the normalized variance of eigenvalues:

$$FA = \frac{1}{\sqrt{2}} \frac{\sqrt{(\lambda_1 - \hat{\lambda})^2 + (\lambda_2 - \hat{\lambda})^2 + (\lambda_3 - \hat{\lambda})^2}}{\sqrt{(\lambda_1)^2 + (\lambda_2)^2 + (\lambda_3)^2}} \quad (21)$$

Where $\hat{\lambda}$ is the MD:

$$\hat{\lambda} = \frac{\lambda_1 + \lambda_2 + \lambda_3}{3} \quad (22)$$

The FA measurement provides information about the shape of the diffusion ellipsoid associated to the tensor. FA is a dimensionless parameter which may assume in a voxel values ranging from zero for isotropic diffusion (spherical shape) up to a maximum value of 1 when the anisotropy is maximum (shape of the ellipsoid elongated in the direction of the fibers) [45]. As such, bright regions in the FA maps reflect areas in which the diffusion is anisotropic and fibers are highly aligned, while dark regions reflect areas in which the diffusion is isotropic (Fig. 19B). The brighter the anisotropic structures, the greater the degree of anisotropy, thus the white matter has high FA values. Particularly, when fibers are arranged in parallel bundles, the anisotropy is higher than in regions where fibers are incoherently oriented within the voxel, such as in subcortical areas. Highly aligned white matter regions will be characterized by very low MD values, while the CSF will have very low values of anisotropy and extremely high values of MD, being practically constituted by free water, so the ellipsoids of diffusion will have spherical shape and great radius if compared to other ellipsoids. Finally, diffusion within the cortex will be more hindered than in the CSF, but considering the size of the voxel typically used in the clinic (2 x 2 x 2 mm^3), there will be no preferential direction of diffusion; therefore, in the cortex the shape of diffusion is spherical but with an higher MD than CSF. Finally, knowing the main orientation of the diffusion ellipsoids (i.e. the direction of the eigenvector ε_1 associated to the largest eigenvalue λ_1), it is possible to obtain a color-coded map modulated by FA, in which the main diffusion direction within each voxel is represented in a different color [46-47], and the color intensity represents the degree of anisotropy. Conventionally, red is assigned to the latero-lateral diffusion direction, green to the antero-posterior diffusion direction and blue to the cranio-caudal diffusion direction [44] (Fig.19E).

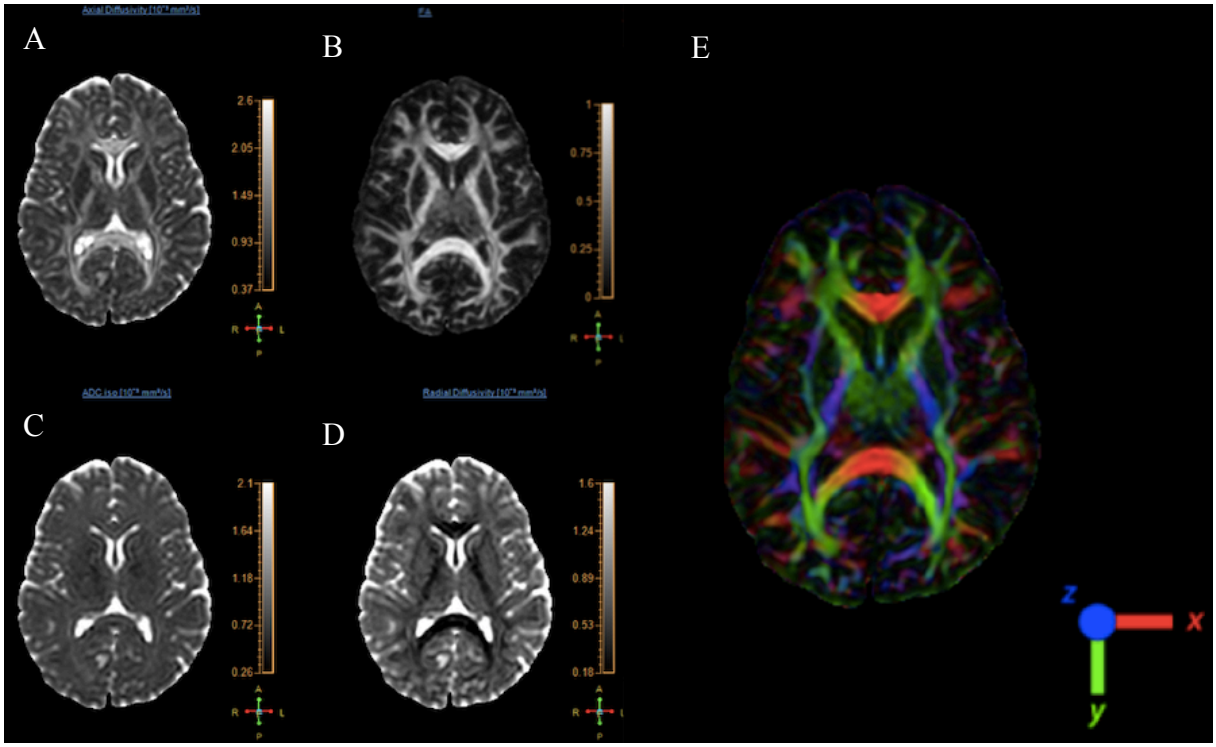

Figure 19. DTI maps of the human brain: A) Axial diffusivity (AD);B) gray-scale FA; c) ADC; D) Radial diffusivity (RD);E) FA color-scale.

Tractography

The information provided by the diffusion tensor allows the identification of the dominant orientation of the WM bundles within each voxel under investigation by analyzing the main eigenvector: this allows to create a three-dimensional vectorial field, from which the architecture of the main WM bundles can be reconstructed by means of a *voxel-by-voxel* interpolation of these principal eigenvectors. This process of integrating voxel-wise tract orientations into a trajectory that connects remote brain regions is called fiber-tracking or tractography.

The main assumption underpinning DTI tractography is that the principal axis of this tensor aligns with the predominant fiber orientation within each voxel; in WM regions, where the fascicles are compact and parallel, the orientation of the principal eigenvector does not change much from one voxel to the next. An algorithm is then used to generate a trajectory connecting consecutive coherently ordered ellipsoids within the brain by following the direction of maximum diffusion from a given voxel into a neighbouring voxel [147]. Starting from a seed voxel, three-dimensional trajectories are generated in all directions from the information contained in the 3D vectorial field until *stopping*

criteria, that reduce errors in the virtual reconstruction of pathways, are satisfied. This is the case of deterministic streamline tractography, the simplest approach for tractography. The most common underlying algorithm is the Fiber Assignment by Continuous Tracking (FACT) [50-92]. However, other methods such as the Euler's method, which works with a constant pitch by means of vectorial field interpolation, are used [41].

Deterministic algorithms start with a properly chosen voxel (seed point) (Fig. 20, voxel indicated with the star inside) and then connect it to the nearest voxel in the direction of the principal eigenvector of the starting voxel; however, using this method, the estimated trajectory often differs from the real orientation of the fibers as the choice of the directional propagation is limited to a range of 26 possible connections for each voxel. The solution to this problem consists in transforming the discrete vector field in a continuous vector field of these data using an appropriate mathematical algorithm [41]: in this way, tracking starts from the center of the chosen voxel and it proceeds inside of that voxel in the retrograde and anterograde coherently to the main eigenvector direction until it reaches its border. At this point, the main eigenvectors of the two voxels are taken as reference to continue the tracking process (Fig. 20).

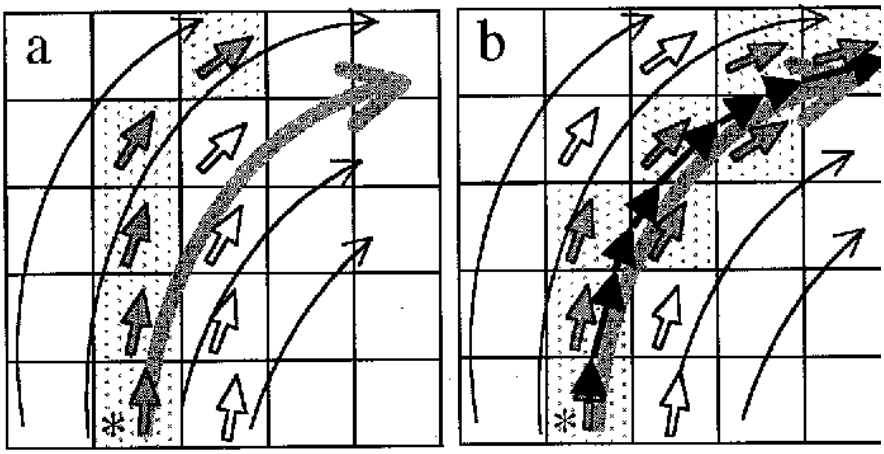

Figure 20. A) Discrete Tracking of fibers using information from diffusion tensor imaging in a discrete field. B) Graphical representation of the FACT algorithm steps for the tracts reconstruction; Voxels with blak dots inside, are the voxel from which the tracking starts (seed point) and continues, the direction of the main eigenvector in each voxel is represented by a black arrow. [149].

The algorithm makes two important assumptions that are known as the FA and the angle thresholds. Trajectories cannot extend to voxels with relatively low FA, to limit tracking to white-matter regions. Typically, the gray matter FA values are between 0.1 and 0.2, thus a simple criterion for ending the tracking is to establish an FA threshold of 0.2.

Trajectories are also interrupted when in consecutive voxels the angle formed by the intersection of their respective principal eigenvectors is smaller than a set angle (i.e., angle threshold <35-60°), to avoid unrealistic fiber bending [50].

WM fiber tracts are reconstructed by the identification of one or more ROI (Region of Interest), which represents a set of voxels presumably crossed by the bundle of interest: the positioning of these ROI is based on a priori anatomical knowledge of the WM areas containing the tracts of interest [52,53]. In general, the entire number of voxels constitute a set of starting points for tracking, however only the tracts passing through the chosen ROI will be displayed [54]. This approach requires a longer processing time but allows for more detailed reconstructions and a more exhaustive representation of the multiple branches of the bundle [52,55], as is evident from Fig. 21.

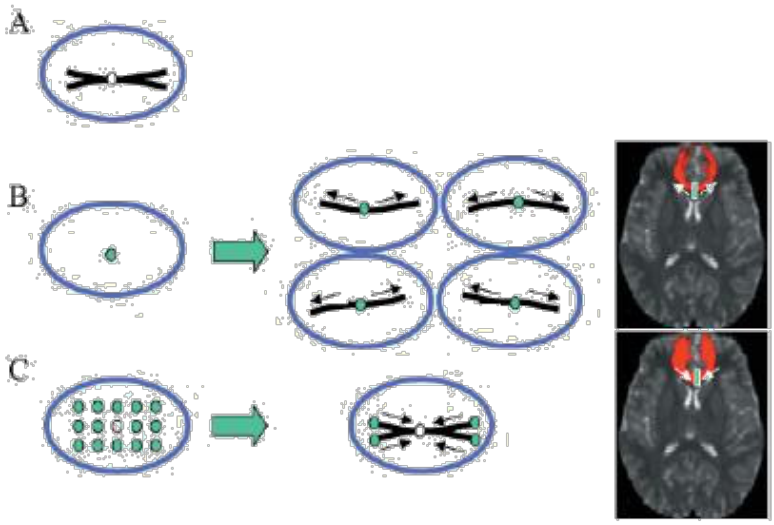

Figure 21. (a) Schematic representation of the bundle of interest; if the tracking starts from the seed point marked by the green circle (b), there will be 4 possible results, each of which will represent only a part of the bundle itself; instead, using multiple seed points (green circles), and displaying bundle that cross the white circle (region of interest), there will be a more correct representation of the bundle analyzed, as shown by the results obtained by the two approaches in the representation of the fibers that cross the genu of the corpus callosum [56].

The obtained trajectories reproduce in a precise way the white matter structure, showing a good correlation with the histological data [50,51]. Projection tracts such as the cortico-spinal tract, connecting the motor cortex to the spinal cord, as well as intra-hemispheric associative tracts and inter-hemispheric commissural fibers can be reconstructed (Fig. 21).

Some limits of tractography should be taken into account: firstly, this technique is not able to distinguish the afferent from the efferent fibers [50] and provides, at this moment, only an analysis of the macroscopic architecture of the white matter tracts due to the relatively low resolution of diffusion MR imaging (2 x 2 x 2 mm^3) if compared to axon dimensions. This

resolution does not allow to detect individual axons orientation whose diameter is typically less than 10 μm. Furthermore, more than one fibers orientation may be present in a given voxel: the estimation of the diffusion tensor in these voxels provides an "average" of such directions, with the net result of an anisotropy reduction in the points where the fibers cross, join or at the level of the cortico-subcortical junction [42,57,58]. This problem result in a low FA value that can be below the established minimum threshold [41] leading to the termination of the tracking algorithm. This limit could be resolved by an improvement in voxel resolution, which involves the use of very high gradients modulus [93]. Moreover, new diffusion approaches allowing to model multiple fiber directions within each voxel have been developed, together with probabilistic tractography methods able to estimate the confidence of each reconstructed streamline. A detailed description of these methods is beyond the scope of this thesis, but it is worth of note that probabilistic methods can track fibers also through regions with high uncertainty in the determination of the principal direction and quantify this uncertainty. However, deterministic streamline tractography is easier to be implemented and its more intuitive approach has contributed to its large diffusion in a clinical setting. In this thesis, deterministic tractography of the corticospinal tract has been exploited in a large animal model, as exploited in the 'Ovine brain anatomy' Chapter.

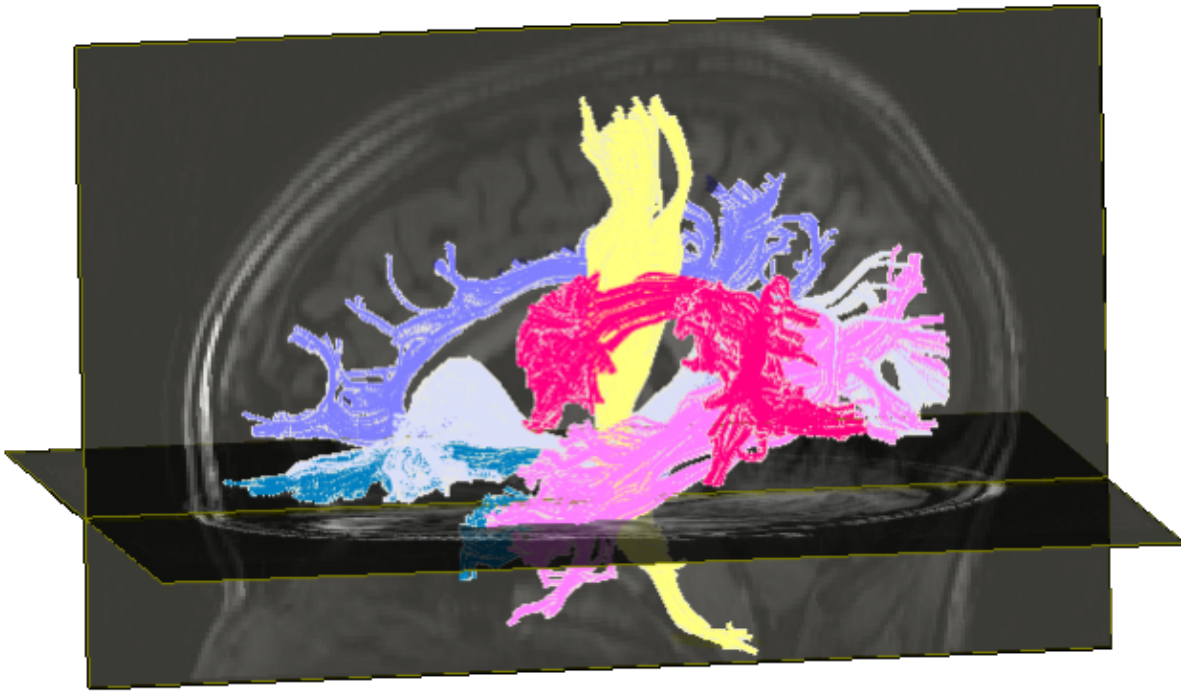

Figure 22.Representation of tractography of different WM tracts of human yellow: CST, magenta arcuate, violet cingulate, grey inferior fronto-occipital fascicle, blue uncinate fascicle, pink inferior longitudinal fascicle .

Artifacts

This paragraph is focused on the most frequent artifacts in MRI, in particular on diffusion images artifacts and programs used for their correction. Subject-related artifacts are due to heart pulsations, pulsations of cerebrospinal fluid, breathing and movements of the head of the subject. Other sources of artifacts such as eddy current distortions are directly related to the MRI system. Moreover, depending on the sequences used for image acquisition, different artifacts' corrections may be necessary. Finally, the images are made comparable through particular pre-processing methods such as normalization and coregistration.

The induced currents, commonly called eddy current, arise from the rapidly changing gradients and RF magnetic fields during a time interval. The activation of these variable magnetic fields induces a current in different components of the MRI scanner. This effect is typical of diffusion sequences because the gradients are applied with a greater modulus compared to sequences used in morphological images. This phenomenon is described by Faraday-Lenz's law which explains how the current induced in a circuit depends on its magnitude, orientation and the rapidity of the magnetic field variation [41,59]. According to the Faraday-Lenz's law faster sequences such as single-shot gradient-echo techniques, also known as echo-planar imaging (EPI), produce major artifacts [63]. Eddy currents degrade the speed and efficiency of gradient switching; electrical pulses driving the gradients become distorted, producing a wide range of image artifacts, including shearing, shading, scaling, blurring, and spatial misregistration. Image processing can correct for spatial nonlinearities and frequency/phase shifts due to eddy currents, as explained below.

Motion artifacts are due to head movement as well as to breathing and heart pulsations [65]. Random head movements can be considered as a combination of translation and rotation. In particular, translation adds a constant phase to all spin while rotation adds a linear phase change in the direction perpendicular to the gradient direction. This linear phase change affects the organization of the data within the k-space leading to data shift [66].

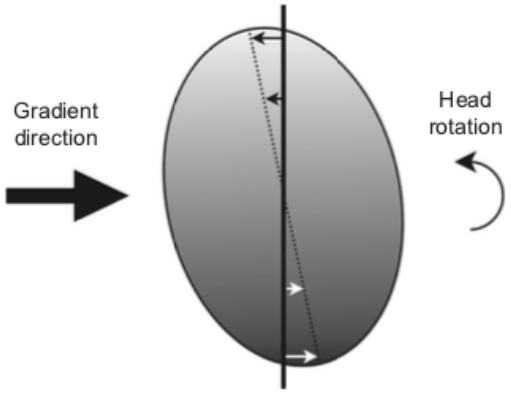

Figure 23. Head rotation and the relatively linear phase change.

Single-shot MRI pulse sequences acquire the complete k-space data required for image reconstruction after a single RF excitation, thus limit motion artifacts compared to multi-shot acquisition sequences.

Heart pulsations and breathing, on the other hand, are not comparable to movements of a rigid body as they produce non-linear phase variations. These artifacts are more complicated than head movement but can be predictable given a constant pulse. A common method to reduce these artifacts is to synchronize the acquisitions to the heartbeat [67].

Image processing

Pre-processing of MRI data is a fundamental step to ensure the correct visualization of the images and the correctness of a subsequent quantitative data analysis. Image pre-processing is often composed by different steps, some of which are common to all modalities while others are case-specific.

Pre-processing aims to correct possible artifacts and to make images geometries and intensities comparable between different acquisitions in order to carry out an accurate analysis in the post-processing phase. Below it is explained how correction of artifacts due to eddy currents, head movement artifacts, normalization of intensities and co-registration of volumes are performed. The intensity normalization process is explained in the '*Materials and Methods*' of this thesis, while the co-registration process is described in the next paragraph with particular reference to the methods used in this thesis work.

Correction of artifacts

Artifacts can be reduced before image acquisition, by choosing specific sequences and parameters, or after image acquisition by using pre-processing methods.

Before image acquisitions, a compromise between artifacts can be obtained by using single-shot EPI sequences with diffusion-weighted gradient pulses. Indeed, the EPI technique, which uses large and fast reading gradients to generate a complete set of gradient echoes, is extremely sensitive to proton diffusion. This set of echoes can be used either in a Spin Echo (SE) sequence or in a gradient echo (GE) sequence, where a pair of bipolar gradients are applied before signal acquisition [39]. These fast sequences reduce the presence of motion artifacts. Further correction that can be made before the examination is to minimize the eddy currents by modifying the diffusion sequence, such as, for example, by dividing the diffusion gradients into 2 bipolar activations [64]. Moreover, optimization of the diffusion gradients directions and their increase in number improve the signal-to-noise ratio of the DWI, allowing a more uniform sampling of the signal in the three-dimensional space and to provide a more accurate estimate of the diffusion tensor [61,62].

After image acquisitions, image pre-processing can minimize or remove artifacts by using specific algorithm. In this thesis work, artifacts' correction was carried out by exploiting different tools of the FSL software. In particular, the *eddy_correct* tool allows to correct for eddy current-induced distortions such as image stretching, shearing, and translation as well as subject movements on the basis of a classical affine transformation. The first non-diffusion-weighted image (b_0) is set as the target image, into which the remaining DWI volumes are registered. In the default setting of FSL, *eddy_correct*[2] uses a trilinear function as an interpolation method (see below).

Image coregistration

Coregistration process is essential in pre-processing of medical images. The term refers to the spatial alignment of a series of images that can be applied between volumes of the same subject (intra-subjects) or between different subjects (inter-subjects). There are different methods of image coregistration, differentiated according to the degrees of freedom (DOF) and to the cost

[2] *eddy_correct 4dinput 4doutput reference_no; input is in 4D format (means all 3D volumes in a matrix), interp is set as trilinear by default. reference_no defoault is the first image of the dataset (b=0);*

function. In addition, correction of motion artifacts within intra-subject acquisitions often use 6 degrees of freedom (DOF) registration. This rigid translation, also known as 'euclidean transformation' is a geometric transformation that preserves the distances between all copies of points [6]. The best coregistration is obtained by finding the transformation matrix that optimizes the cost function between two images. Particularly, the rigid transformation includes 3 rotations and 3 translations, one for each orthogonal spatial axis. The cost function is obtained by a similarity criterium that allows to calculate the goodness of the correspondence between two images. Thanks to their accuracy and robustness, mutual information (MI) and normalized mutual information (NMI) are the most used cost functions. Both methods measure the statistical dependence between the two images but the NMI method is less likely to cause recording errors [6]. Errors in this phase inevitably cause a mismatch between the diffusion and the anatomical information causing errors in the reconstruction of the maps, diffusion tensor and tractography and also incorrect data analysis. In particular, coregistration of the DTI data to the morphological images must be followed by a precise reorientation of the tensor i.e. gradients' table [94].

Cost Function

Normalized Mutual Information is based on histogram and entropy concepts [7]. The histogram of an image represents the frequency of each voxel intensities of the image. With the histogram it is possible to construct an occurrence probability (p_i) of the intensities by dividing each frequency by the total number of intensities (bin).

From the occurrence probability definition, 'Shannon's entropy' (H) is determined by the formula:

$$H(immagine) = -\sum_{i=1}^{n} p_i * \log_2 p_i \tag{23}$$

Where:

$$p_i = \frac{frequenza\ dell'intensità\ \ i-esima}{bin} \tag{24}$$

$H(image)$ is a number representative of the 'disorder' of the image, thus it is equal to zero for homogeneous images and increases its value as the information carried by the image increase. Joint histogram is calculated between two images and then the mutual entropy is obtained by determining H of the joint histograms.

The joint histogram can be represented graphically and it can be noticed how the visualization changes with the rotation angle of the input image with respect to the reference one. When the images are identical, all the corresponding grey tones are on the diagonal of the matrix. Fig.24 shows the entropy value and the joint histograms matrix calculated between two MRI when one is rotated by 2.5, 5 and 10 degrees, respectively [7].

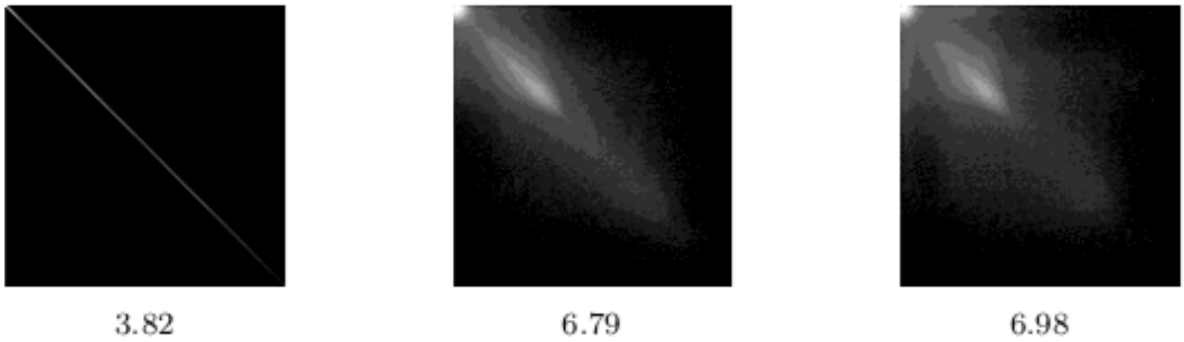

Figure 24. Joint Histogram for 2.5,5 and 10 degrees of input image rotation. Beneath the joint histogram the respective Entropy value is shown [7].

By summing up the matrix of the joint histogram, we obtain H, defined as:

$$H(immagine\_rif, immagine\_reg) = -\sum_{j=1}^{n}\sum_{i=1}^{n} p_{(i,j)} * \log_2 p_{(i,j)} \tag{25}$$

Therefore, normalized mutual information (NMI) can be defined as:

$$NMI = \frac{H(immagine\_rif) + H(immagine\_reg)}{H(immagine\_rif, immagine\_reg)} \tag{26}$$

Where $H(immagine\_rif)$ and $H(immagine\_reg)$ are Shannon's Entropy of the two images while $H(immagine\_rif, immagine\_reg)$ is the Shannon's entropy for a common

distribution of $immagine\_rif$ e $immagine\_reg$. NMI function has to be maximized thus $H(immagine\_rif, immagine\_reg)$ must theoretically be close to zero.

Through input images and transformation matrix multiplication, reference and input images can be coregistered. When the transformation matrix is applied to the input image, the new position of the voxel intensities must be determined. This process often requires a sampling of the voxel centers and then an interpolation process. FSL software uses a trilinear function as the default interpolation method. A further method is the nearest neighbour interpolation, a method that simply determines the "nearest" neighbouring voxel among surrounding voxels, and assumes the intensity value of it to estimate the value of the new voxel in the transformed image.

Ovine brain anatomy

This chapter will give a general overview of the ovine brain anatomy and its similarity with the human one, as in this thesis an ovine animal model has been exploited to study the distribution of a substance delivered through CED within the brain tissue.

The central nervous system (CNS) of human and animals is made up of the brain, its cranial nerves and the spinal cord. Brain can be divided into three anatomically distinct parts: cerebrum, cerebellum and brain stem. The cerebrum, which forms the major portion of the brain, mediates higher functions such as cognition and sensory integration, and is divided into two major parts: the right and left cerebral hemispheres [76-77]. The outermost part of the hemispheres is called the cerebral cortex and consists predominantly of gray matter; in the cortex reside all the processing centers of higher intellectual functions, such as memory and language. The cerebral cortex has sulci (small grooves), fissures (larger grooves) and bulges between the grooves called gyri. Gray matter consists predominantly of the cellular bodies of neurons, the basic processing unit of the CNS. Going through the inner part of the brain, towards the underlying layers of the cortex, there is a transition from gray (GM) to white matter (WM) (Fig. 25). Beneath the cerebral cortex or surface of the brain, connecting fibers between neurons form the white matter, which is composed of myelinated axons and glial cells. Communication between the two hemispheres is anatomically localized in a preferential area, the corpus callosum, consisting of a thick bundle of white matter.

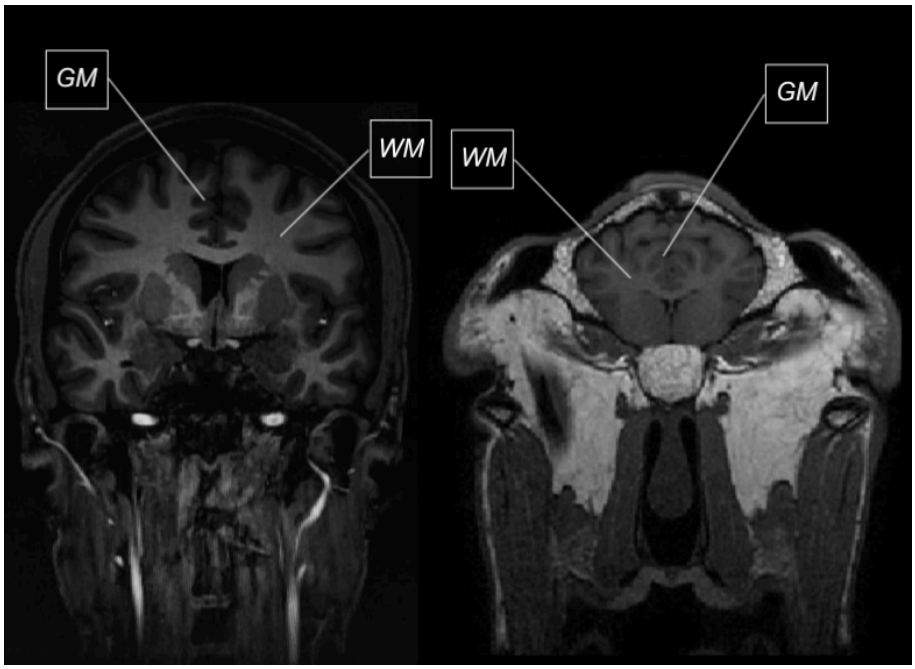

Figure 25. Gray and white matter in human (left) and ovine brain (right).

Sheep offer a great degree of research translatability into basic brain functions as they have a long lifespan, have rudimentary and well-established housing demands and are safer than primates to be managed in experimental settings, especially because they do not have hands to interfere with equipment [78]. Most importantly, sheep have heavily folded and fissured, gyrencephalic brain more similar to human if compared to the lissencephalic brain of rodents and rabbits, due to its relatively large size and the presence of sulci [79].

Fig. 26 shows different brain region that are both present in human and ovine brain structure as the cingulum, thalamus, hippocampus, corpus callosum, and internal capsule that include the projection motor fibers of the cortico-spinal tract (CST).

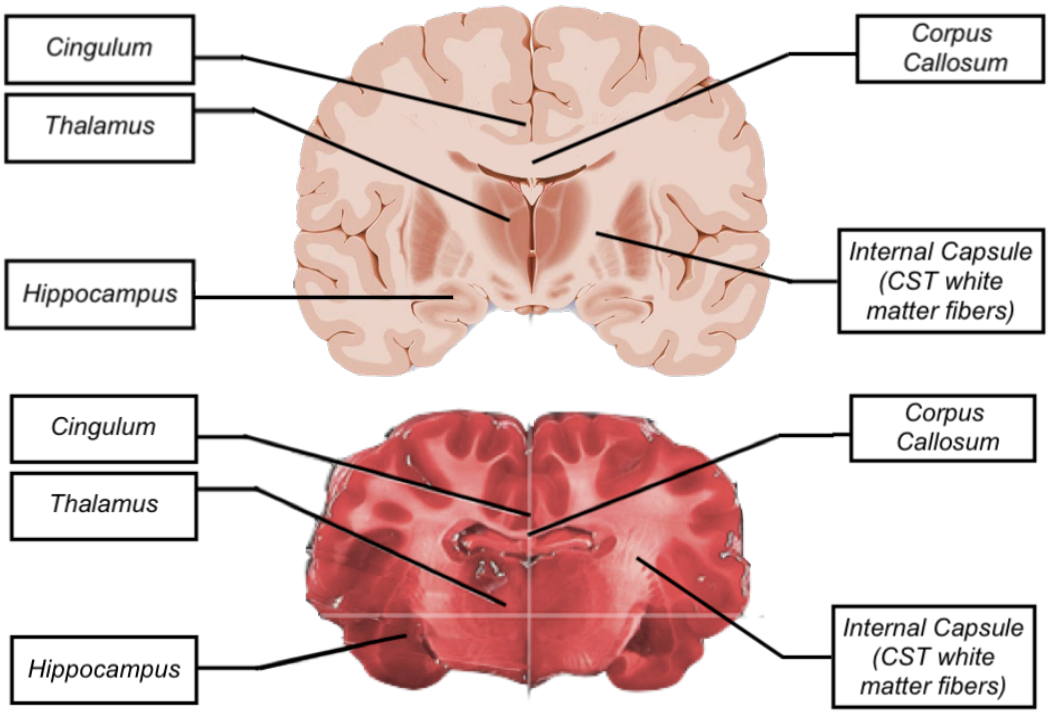

Figure 26. Comparative anatomy between human (A) and ovine (B) brain.

Again, the similarities between caudate nucleus, putamen and substantia nigra in the sheep and human brains, provide a valuable and valid tool for modelling basal ganglia diseases [85].

Further similar features to humans are evident in electroencephalographic records, neuroradiological features, and neurovascular structures [80], thus making the ovine model of particular relevance in the field of experimental neuroscience. For example, it has been studied in the context of epilepsy [81], neuropsychiatry [82], traumatic brain injury [83], and neurodegenerative diseases [84].

Intriguingly, studies recently demonstrated neurofibrillary accumulation in normal aged sheep, extremely similar to the tau deposits associated to Alzheimer's disease (AD) in humans, so that researchers are now testing the fitness of the ovine for future genetic manipulation to generate AD animal model [86].

Furthermore, due to these similarities with human brain, the ovine model can be particularly valuable in the context of neurosurgical research to test new devices and peri-operative technologies. In this scenario, the possibility to explore *in vivo* the imaging features of the ovine brain becomes relevant for pre-surgical planning and intraoperative neuro-navigation, for example in the case of CED. Despite the growing interest in using sheep as a model of large mammals with complex central nervous system, comprehensive ovine MRI studies are rather limited, presumably because they are hardly feasible and require a well-organized and specialized multidisciplinary team [87].

Ovine brain structure and even the fundamental white matter bundles are similar to the homologous structures of human and other mammals, which is pivotal for the translational purpose of using sheep models in neuroscience and thus in this thesis project.

Indeed, white matter fibers have been conventionally classified into different categories depending on their paths, both in humans and in animals [88-89]. For instance, tracts in the brainstem comprise the motor fibers of the CST and its cerebellar connections, while projection fibers include the suprathalamic portion of CST that connects cortical to subcortical white matter. With respect to the other primates, the CST in sheep is smaller and composed of thinner fibers [90]. In this work, CSTs have been reconstructed by means of DTI tractography *in vivo* to be used as a target for the CED infusion experiments. An Atlas of the Ovine White Matter Fiber Bundles was created in 2019 [148], showing different WM fiber bundles that are comparable with humans tracts.

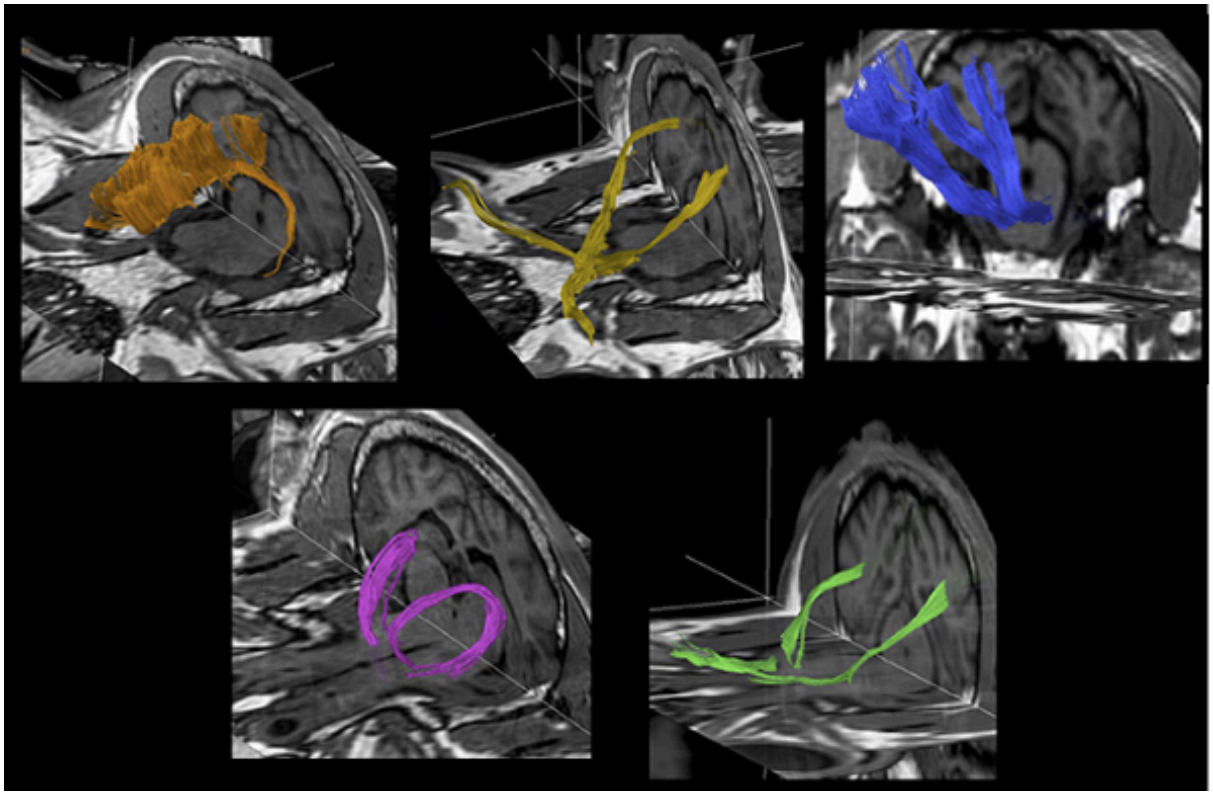

Figure 27.Representation of tractography of different WM tracts of sheep brain [148]: Corpus callosum (CC, orange). Visual pathway (VP, yellow), CST (blue), Fornix (FX, pink) and Occipitofrontal fasciculus (OF, green).

Convection enhanced delivery (CED)

Convection enhanced delivery (CED) is a minimally invasive technique for local delivery of substances within the brain. CED represents an efficient method to bypass the Blood-Brain-Barrier (BBB), a selective semipermeable hedge surrounding brain capillaries that obstacles the penetrance of most therapeutics in the brain. In order to overcome this barrier, CED enables the release of therapeutic agents directly inside the brain for treating many different diseases, including malignant gliomas, Alzheimer's disease, Parkinson's disease, epilepsy and ischemic stroke [124]. However, clinical trials exploiting CED techniques have been largely unsuccessful [26]. In the following paragraphs, the principle of operation, the limits and the feasible applications of CED are discussed.

Principle of operation of CED

The therapeutic agent is released through one or more stereotactically positioned catheters connected to an infusion pump that keeps a constant pressure at the tip of the catheter, thus allowing the substance to be released in a particular brain area at a controlled rate.

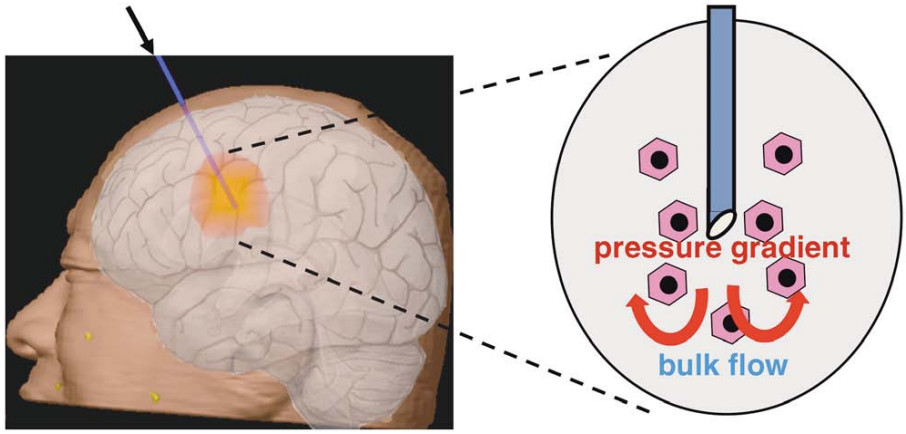

Figure 28. Principle of operation of CED technique. The continuous positive pressure is maintained at the tip of the catheter, releasing the infusate through convective flow [2].

Convection includes two distinct phenomena: diffusion and advection. Diffusion phenomenon is described by Fick's law, and has already been extensively explained in the *'Principles of diffusion'* chapter. On the other hand, advection is the movement of a substance along the pressure gradient and is described by Darcy's law:

$$v = -K * \nabla p \tag{27}$$

Where v is the molecule speed, directly proportional to the pressure gradient and to the hydraulic conductivity. The latter describes the fluid ability to move through spaces (in this case through the catheter lumen). Compared to diffusion, advective flow is largely independent from drug molecular weight.

In Fig. 29 it can be noticed how the advection factor gives a greater contribution to the volume distribution than the diffusive factor.

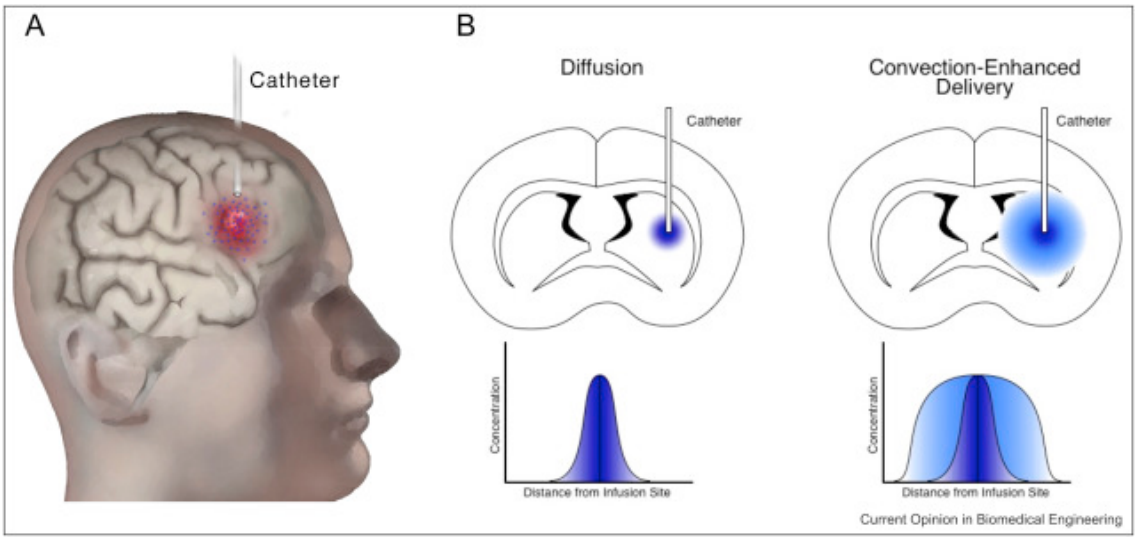

Figure 29. Infusate concentration is much higher for CED technique than for simple diffusion. [73]

Constraints of CED

CED physical principles are rather simple, while the development of different infusion strategies is required for the several existing infusion methods [2]. In this regard, CED techniques strongly depend on different physical constraints. In fact, besides the difficulty of surgery and catheter insertion, infusion parameters should be carefully tailored in accordance to the specific drug half-life and tissue clearance rate. These constraints can cause different complications during CED, such as backflow, air in the syringe, and partial destruction of the parenchyma during catheter insertion, especially if the choice of infusion variables has not been finely tuned for the specific case-scenario.

Backflow

Backflow, also known as reflux, is the infusate flow in the opposite direction with respect to the one of catheter insertion. Backflow occurs when the pressure at the tip of the catheter equals the pressure of the underlying tissue, or when part of brain tissue is damaged by catheter insertion, creating an empty space around the outer surface of the catheter in which the infusate can penetrate [17]. Reflux consequences are mainly associated with low drug concentration in the targeted brain area, excess of toxicity in areas surrounding the target, and lack of predictability of the distribution volume in the region of interest.

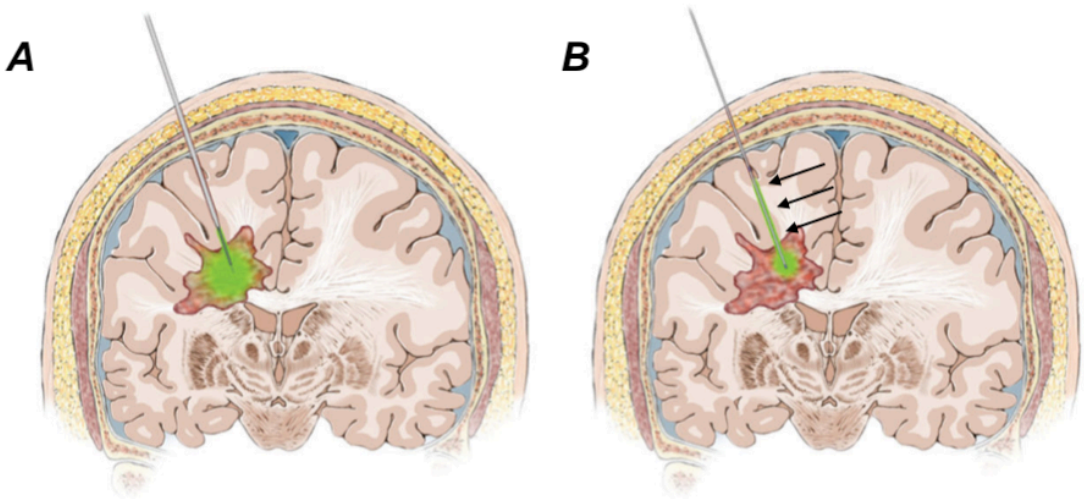

Figure 30. A) CED without backflow. B) Backflow in the infusion direction along the catheter (black arrows - green in cannula) with diffusion occurring with a non-convected injection [17].

Design and catheter size can be optimized to reduce the backflow phenomenon. In particular, catheter diameter of 27 G (0.36 mm) or less significantly reduces the presence of backflow [12]. Infusion parameters and settings can influence the probability of backflow as well, in particular when the infusion rate is high or when the stiffness of the catheter increases [18].

Air bubbles

The presence of air in the tip of the syringe may damage the underlying tissues and increase the likelihood of backflow [18]. It may also alter local pressure at the infusion site, affecting the final distribution volume. In addition, MR images acquired in the presence of air bubbles could lead to artifacts. For instance, in case of T1-weighed images, rounded areas of marked hypointensity are present close to the catheter tip, limiting the underlying structure visualization. Therefore, it is necessary to ensure that the tip of the syringe and any of its channels are free of air bubbles before

inserting the catheter. Finally air bubbles can leads to unpredictable flow path within the brain structure.

Flow rate and Volume of distribution and infusion

One of the parameters that should be carefully adjusted in CED is the 'infusion rate', which is positively correlated to the distribution volume (V_d), and also to the probability of backflow. However, due to the current modern design of catheters, an infusion rate of 50 µL/min can be reached without causing reflux [19]. Nonetheless, the likelihood of brain tissues damage remains high [13]. V_d and volume of infusion (V_i) ratio is different according to distinct anatomical brain locations and specific for each pathology, and is a key variable to predict the required V_i [3]. Recently, several articles reported that volume distribution is strongly dependent from different features of the infused molecules, such as size, molecular weight, hydrophobicity, charge and viscosity [20-22]. As an example, high molecular weight compounds, such as an antibodies, may take up to 3 days for only 1 mm spatial spread, that is not a reasonable time for a therapeutic treatment [25]. Furthermore, V_d increases linearly with V_i [26], except in cases of excessive flow rate. In general, the drug transport during CED is governed by bulk flow, diffusion and clearance loss due to permeation and reaction.
It has been reported that, along the fiber direction, the white matter has a lower resistance to convection rather than the grey matter, which exhibit more tissue homogeneity [2,26]. In this concern, the V_d / V_i ratio was 4:1 in gray matter while the ratio of compacted white matter ranges from 6:1 to 10:1, meaning that drug distribution is greater in WM than GM thanks to increase permeability of WM that leads to conduct fluid flow at a different rate [159].
It still remains unclear if a difference in resistance can be appreciated in the white matter if the infusion is specifically delivered *along* (parallel to) the fiber direction or *orthogonal* to the fiber direction in the same target point.

Visualization of volume distribution

Gadolinium (Gd) is a MRI contrast agent used in solution with other substances to monitor volumetric distribution during CED infusions [15-16]. Gadolinium has been used in various formulations, including Magnevist, Omniscan or Prohance [23]. In T1-weighted images, these solutions result hyperintense and therefore visible as a bright and clear region.

Clinical Trials efficacy exploiting CED

Despite technological developments in medical and biomedical field, clinical trials with CED procedure have been largely unsuccessful. These failures have been helpful in order to identify a number of pivotal parameters that still needed standardization for successful clinical applications, such as specific drug biodistributions, most appropriate needle diameter, flow rate and volume distribution [26], as well as to improve effective catheter positioning and patient-tailored protocols.

Nowadays, CED has been mainly exploited for the treatment of glioblastoma (GBM), and the majority of the ongoing experimentations are focused on tumors rather than on neurodegenerative diseases. The first clinical demonstration of CED therapeutic efficacy was reported in the early 1990s by Edward Oldfield's group [3]. In this study, a chemotherapeutic agent selectively targeting transferrin receptor was used to induce tumoral cells death. The authors reported that 9 of 15 patients with recurrent GBM showed a 50% tumor reduction without systemic toxicity. However, 3 participants that were treated with higher concentration suffered of complications. Furthermore, the PRECISE study aimed to treat recurrent GBM with an exotoxin agent that targeted an overexpressed GBM cell receptor and was one of the largest studies applying CED, but did not demonstrate an overall survival benefit [115]. However, the progression-free survival was better for patients treated with CED. Another clinical trial, using Topotecan as a therapeutic agent (cell division inhibitor), demonstrated tumor regression in 69% of patients at a concentration which was not toxic [26]. Lidar et al. [111] used Paclitaxel as antitumoral agent and reported a positive response rate of 73% with 5 patients exhibiting complete response, while 6 showing partial response. Further investigations demonstrated how oncolytic virus represent a promising strategy for cancer therapy that can be delivered by means of CED. Preliminary data in a Phase I study showed conflicting results with 3 patients remaining disease-free for 5 to 12 months post treatment, while others having recurrent tumor growth after two months [118].

Clinical trials using CED technique have also been proposed for Parkinson's diseases. For instance, Gill et al. [104] injected a neurotrophic factor directly in the putamen of 5 patients and an improvement in dopamine function was detected. On the contrary, Amgen et al. [121] arrested their study due to the presence of cerebellar neuronal loss and 'neutralizing antibody' in 2 of their 34 patients. Anyway, other patients did not demonstrate any clinical improvements.

Although CED could be applied to a variety of CNS disorders, different parameters still need to be standardized: in vivo monitoring, prolonged delivery, and catheter technology. Particularly, the main issues related to the CED technology are essentially three: catheter positioning, lack of flexible protocol, and prevision of drug volume distribution [23]. In the PRECISE study, just 49,8% of the catheter placements met all the established positioning criteria and the drug concentration has been locally ineffective probably due also to this specific reason [114]. Furthermore, the major obstacle in different studies, lied in the absence of a reliable method to determine *in-vivo* drug distribution [26]. Infusion catheter positioning must be improved through computer simulation software and real-time monitoring with MRI, ultrasound techniques or robotic arms [119].

Preclinical Trials exploiting CED: assessment of drug distribution

To date, *in vivo* CED studies firstly aiming at detecting drug distribution within different brain structures are limited, and investigations on the effect of catheter positioning on distribution volume are scarce. Different computer simulation based on a variety of assumption and different physiological and physical parameters have been investigated, demonstrating qualitative prediction of different drug distribution, even if they do not take into account *real case* scenarios. Furthermore, different factors may affect the diffusion such as temperature, restriction, hindrance, membrane permeability and, as mentioned before, anisotropy and tissue inhomogeneity [120].

Interestingly, some preclinical studies found that delivery within tissue structures such as white matter, gray matter, and adjacent CSF regions have complex transport characteristics, based on their underlying structure. Gray matter, which is composed mainly of neuronal cell bodies, neuropil, and glial cells, has a roughly isotropic structure and diffusivity and the hydraulic conductivity may be considered to be the same in all directions [99]. Differently, white matter is composed of bundles of myelinated axons, and referential diffusional transport has been measured to occur preferentially along the direction of aligned fiber tracts compared to radial direction [100, 125-127]. Previous CED studies also indicated that preferential convective transport also occurs along fiber tracts' directions [3,101,102]. This preferential flow has been attributed to the anisotropy of fiber tracts, with a high hydraulic conductivity in fiber axial direction compared to the radial one [96-97]. Finally, it has been suggested also that flow direction could be determined both by catheter orientation (pressure gradient direction) and from resistance to flow. The latter is location-dependent (heterogenous) and direction-dependent, so that the different structure of WM and GM dictates flow in a different way, by influencing V_d/V_i rate. Even if the careful evaluation of microstructural constraints was not the aim of previous studies, different papers reported white matter as a preferential path for drug distribution [103,109].

In the preclinical study conducted by Raghu et al. [106], Gd solution was infused at 0.5 µL/min directly into the pig WM internal capsule and the expansion remained highly localized inside the WM, with little observed changes in GM. In another study of Raghu Raghavan et al. [24], it was shown that infusion of Gd-DTPA into pig brain had an irregular shape owed to the preferential infusion path along white matter tracts (Fig 31 A). In the Jung Hwan Kim et al. study, Gd-DTPA albumin was infused near the alveus interface in rats at 0.3 µL/min, and the infusate distributed preferentially along fiber tracts of the corpus callosum, with limited penetration within adjacent gray matter [109] (Fig 31 C). In accordance to this last study, Morrison et al. [103] infused 75 µL ^{111}In-transferrin solution through a catheter placed in the corona radiata (WM) of a cats at 1.15 µL/min. Those molecules exhibited a tendency to flow in a parallel direction to the fiber tracts rather than perpendicular to them (Fig 31 B). Similar results with cats were obtained by Bobo et al. [3], where isotope-labelled transferrin was infused in cat corona radiata at 4 µL/min and infusate predominantly distributed in WM immediately after infusion (2h) while penetrated into GM over the next 24h. In the experiments conducted by Endo et al. [129], *Evans blue dye* was injected through CED in the white and gray matter in the spinal cord of rats with infusion rate and total volumes of 0.2 µL/min and 2 µL respectively. The infusate distributed over longer distances in the white matter than in gray matter, while the volume distribution was greater in gray matter. In addition, white matter infusate did not infiltrate into adjacent gray matter, while gray matter infusate partially diffused even along white matter in the lateral spinal cord. Again, infusion within the lateral CST of primates at 0.1 µL/min for 20-40 and 50 µL leaded to perfusion over several segments of the spinal cord [126].

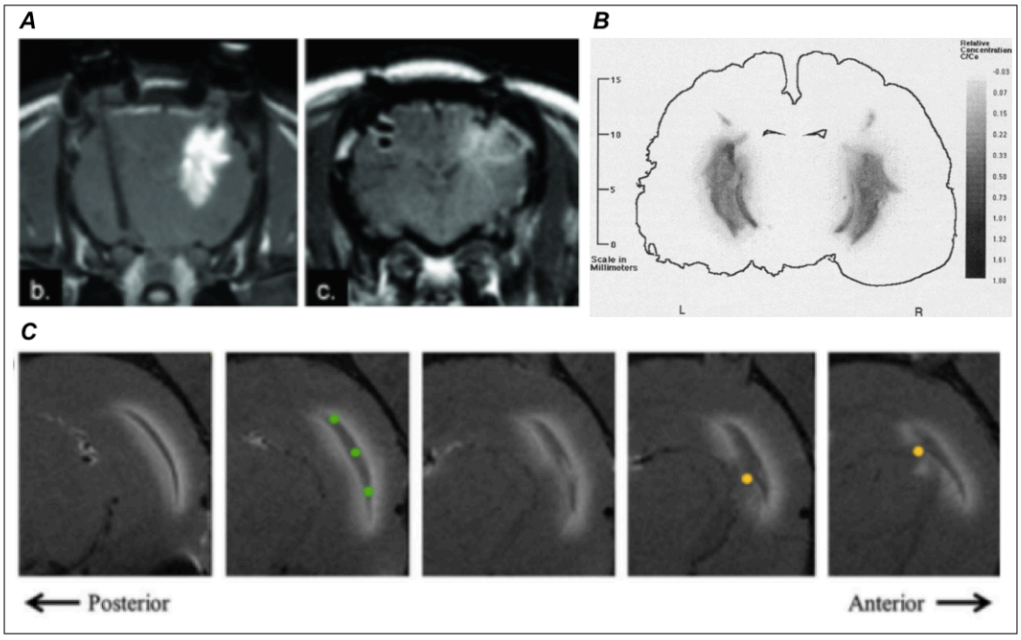

Figure 31. A) b) Results of a 90-minute infusion into a pig brain (Fig. b) followed by imaging 20 hours thereafter (Fig. c) [24]. These data were obtained from an experiment directed by Michael Moseley at Stanford University, Stanford, California, and funded by what was then Image-Guided Neurologics, Inc. B) Infusion in the Corona radiata of cat. Infusate tended to follow the parallel direction of WM fibers [103]. C) Gd-DTPA infusion into alveus interface in rats. Agents seems to follow the preferentially the WM tracts [109].

Despite exploiting different experimental settings and constraints such as flow rate, catheter positioning, total amount of infusate and different subjects, all the previous CED experiments emphasized a difference in the infusate distribution behavior within gray and white matter, showing a preferential path along fiber tract direction [3,103,126,129]. Only three of these studies demonstrated this difference by means of histological analyses: after injecting gadolinium conjugated with Evans Blue, this dye is then visible in mice histological sections [3,126,129].

Aims of the project

As shown by a variety of clinical trials, the applications of CED technique have been widely unsuccessful due to inaccurate catheter positioning, lack of flexible protocols and inaccurate prediction of drug volume distribution [23]. Thus, the main goal of the experiments conducted in the context of EU's Horizon EDEN2020 Project was to set a novel integrated platform for accurate drug delivery in the brain and to provide quantitative data for improving CED planning and integration with the surgical procedure, as well as predicting the expected drug volume of distribution, possibly leading to more successful and standardized clinical trials.

In this context, the aim of this thesis work was to precisely characterize in-vivo drug distribution in brain tissue after CED:

1. by defining the microstructural properties of the ovine brain tissue using DTI;
2. by assessing the impact of brain microstructural features, as depicted by DTI, on drug diffusion, facilitating it in any direction;
3. by studying drug distribution after infusions both parallel and orthogonal to white matter fiber tracts in order to provide quantitative measures on how different orientations of the catheter delivering the infusion may influence CED.

Materials and Methods

Study population

Seven female adult (1-year old) sheep *ovis aries* of about 70Kg have been imaged for this project. Sheep have been selected as appropriate animal models due to their anatomy, physiology, and neurological development. The choice of female gender was due to the size, weight and to the social behavior characterized by a low agonist component favoring housing and handling. All animals were treated in accordance with the European Communities Council directive (86/609/EEC), to the laws and regulations on animal welfare enclosed in D.L.G.S. 26/2014 and approved by the Italian Health Department.

Animals were anesthetized via the intravenous administration of Diazepam 0,25 mg/Kg + Ketamine 5 mg/Kg, intubated and then maintained under general anesthesia with isoflurane 2% and oxygen 2L. They were placed in prone position in the MRI scanner. For each animal, high-resolution MRI datasets have been acquired on a 1.5 Tesla Philips scanner (Achieva, Philips Healthcare) at a veterinary imaging facility [‘Fondazione La Cittadina Studi e Ricerche Veterinarie’, Romanengo (CR), Italy] and specific hardware characteristics are listed in Tab.1. The following paragraphs describe in details the subsequent protocol steps, followed for each sheep MRI acquisition.

Figure 32. Sheep prone positioning in the MRI scanner under anesthesia.

Experimental setting: workflow

The following protocol steps were carried out dedicating one day per sheep at the veterinary center ['Fondazione La Cittadina Studi e Ricerche Veterinarie'] after sheep anesthesia and sheep positioning inside the 1.5 T MRI scanner. All these boxes are explained in the next paragraphs.

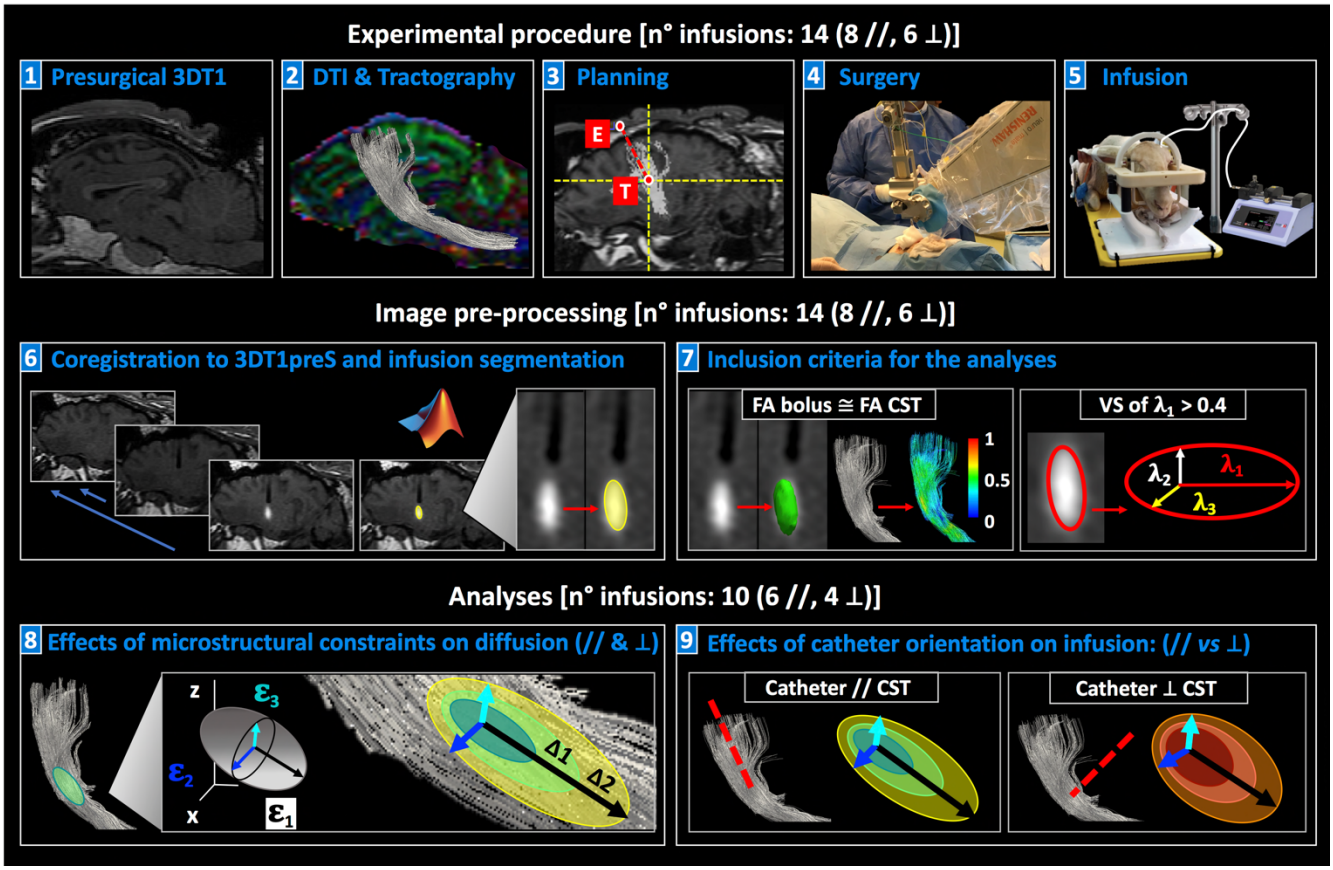

Figure 33. Workflow of Sheep MRI acquisition protocol, image pre-processing and analyses, fully explained in the following paragraph of the main text.

Experimental procedure

1- Presurgical imaging protocol: 3DT1 and DTI

MR imaging was performed on a 1.5T scanner (Achieva, Philips Healthcare). Small and medium flex coils fixed over both hemispheres were used. Diffusion Tensor Imaging (DTI) data were obtained from all the animals by using a single-shot echo planar (EPI) sequence with parallel imaging (SENSE factor R=2). Diffusion gradients were applied along 15 non-collinear directions, using a b-value of 1000 s/mm^2. The detailed imaging parameters for DTI were: TR/TE 6700 ms/84 ms; acquisition isotropic voxel size 2 × 2 × 2 mm; 45 slices. Two signal averages (NSA=2) were obtained, for a total

scan time of 5 minutes 34 seconds. A T1-weighted volumetric scan was also acquired from each animal by using a three-dimensional fast-field-echo (3D-T1 FFE) sequence with the following parameters: TR/TE 25 ms/5 ms; flip angle 40°; voxel size 0.667 × 0.667 × 1.4 mm^3; SENSE factor R=2; 150 slices; acquisition time 8 min 40 s. All the MRI sequences were oriented perpendicular to the longitudinal axis of the scanner.

DTI and 3DT1 images were acquired for each of the seven sheep (14 infusions, 8 parallel and 6 perpendicular) with image characteristics shown in Table 1.

	3DT1-preoperative	**DTI-15**
Sequence	Volumetric T1 Fast Field Echo	Diffusion-weighted Spin Echo EPI single-shot pulse
TR [ms]	25	6700
TE [ms]	5	84
Flip angle	40	90
Acquisition Matrix	288 x 288	96 x 96
Voxel size [mm^3]	0.667 x 0.667 x 1.4	2 x 2 x 2
Slice thickness	1.4	2
Slice number	150	45
SENSE factor	2	2
b-value [s/mm^2]	-	0, 1000 (15 directions)
Acquisition time [min]	8.4	5.34

Table 1. Acquisition parameters of pre-operative 3D T1 and DTI at 15 directions.

2- DTI pre-processing and Tractography

The volumes were exported from the MRI scanner and then converted from DICOM to Nifti format using the MRIcron *dcm2nii* tool (https://www.nitrc.org/projects/dcm2nii/). Once converted, motion and eddy current artifacts were corrected by means of the FMRIB Software Library (FSL, https://fsl.fmrib.ox.ac.uk/fsl/)[3]. Subsequently, diffusion maps were extracted with the *'Diffusion ToolKit'* (DTK) software (http://trackvis.org/dtk/), requiring different input parameters including b-values and gradient table values. Gradient files together with DWIs were used by the DTK program to define one diffusion tensor in each voxel.

[3] *eddy_correct DTI-15.nii.gz DTI_15_EC.nii.gz 0, where 0 identify the diffusion weighted images with b=0*

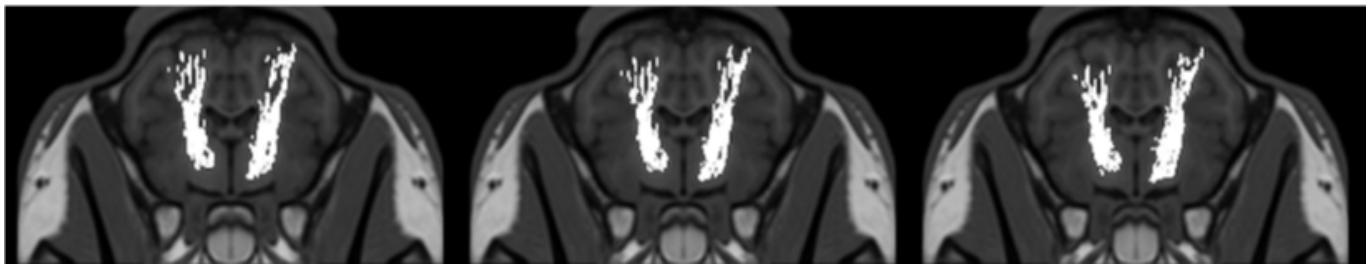

Figure 34. Transverse plane view of CST superimposed on pre-operative 3DT1

Furthermore, DTK computed a whole-brain deterministic tractography of the sheep brain, keeping an FA threshold equal to 0.15 and max angle equal to 27° as stopping parameters for the algorithm.
Then, the *whole brain* tractography was opened in *TrackVis* software (http://trackvis.org) and ROIs were manually contoured at the level of pons and internal capsule on the color-coded FA maps, in order to dissect the corticospinal fiber tracts (CSTs). Raw tracts resulting from the first tracking procedures were then refined manually, on the basis of anatomical knowledge, by removing the surfeit of fibers with excluding ROIs.

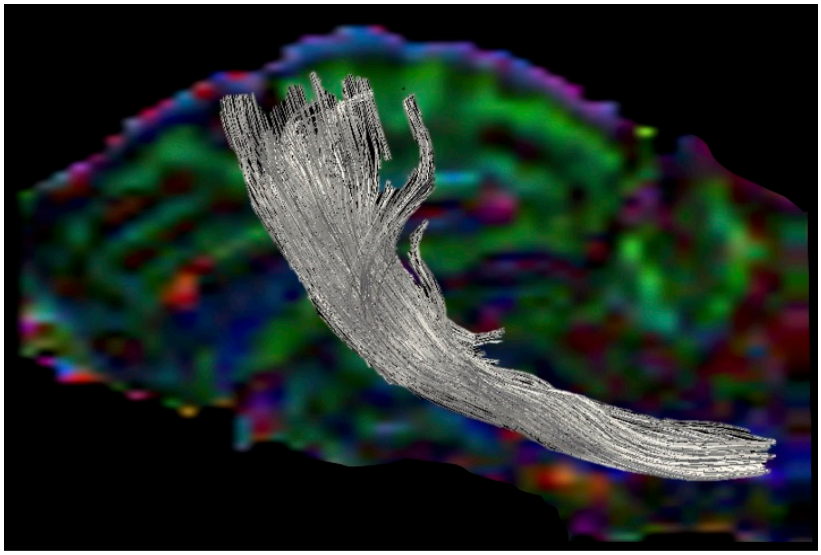

Figure 35. CSTs elaborated and visualized by means of TrackVis software..

Using an *in-house* Python script, the corticospinal tracts (CSTs) were coregistered to the 3DT1-preoperative space. The b=0 EPI volume (reference image without diffusion weighting) was registered to the 3D-T1 anatomical image volume using a 3D affine transformation (FLIRT tool) that was then applied to obtain a nifti mask of the tracts onto the anatomical images.
The resulting coregistered CSTs masks were binarized with the FSL fslmaths function[4] and overlaid on the preoperative 3DT1 images

[4] *fslmaths CSTs_to_3DT1.nii -bin CSTs_to_3DT1_bin.nii.gz*

3- Presurgical planning

Once the CSTs were coregistered and superimposed on the T1-weighted volume, the neurosurgical planning was carried out by means of the 'Neuroinspire' neurosurgical planning software supported by a 3D simulation performed with '3D Slicer' software. An expert team composed by a neurosurgeon an engineer and two veterinary surgeons selected the most compact portion of the internal capsule of CSTs as the target region for the infusions. On this region the Principal component analysis (PCA) was used to calculate the main direction of the CSTs to define the entry point in such a way that the catheter will results perpendicular or orthogonal to the CSTs. The procedure consisted in the stereotactic insertion of a rigid infusion catheter, the 'guide' catheter, that has an internal hollow in order to allow the subsequent insertion of a tiny infusion silica catheter. The latter has a diameter of 0.3 mm and has been always inserted just before the actual infusion procedure, with an offset of 5 mm from the rigid infusion catheter. The catheters reached the target inside the CST avoiding obstacles such as brain ventricles, arteries and other vital structure for human and animals.

4- Surgical procedure

The 'guide' catheter was stereotactically inserted allowing to reach the target point. The 5-mm offset between the tip of the 'guide' catheter and the tip of the infusion silica aimed at reducing the likelihood of complications during infusion such as backflow or tissue damage. Once the correct trajectory was found and the 'guide' and infusion silica catheters were inserted, infusions were performed.

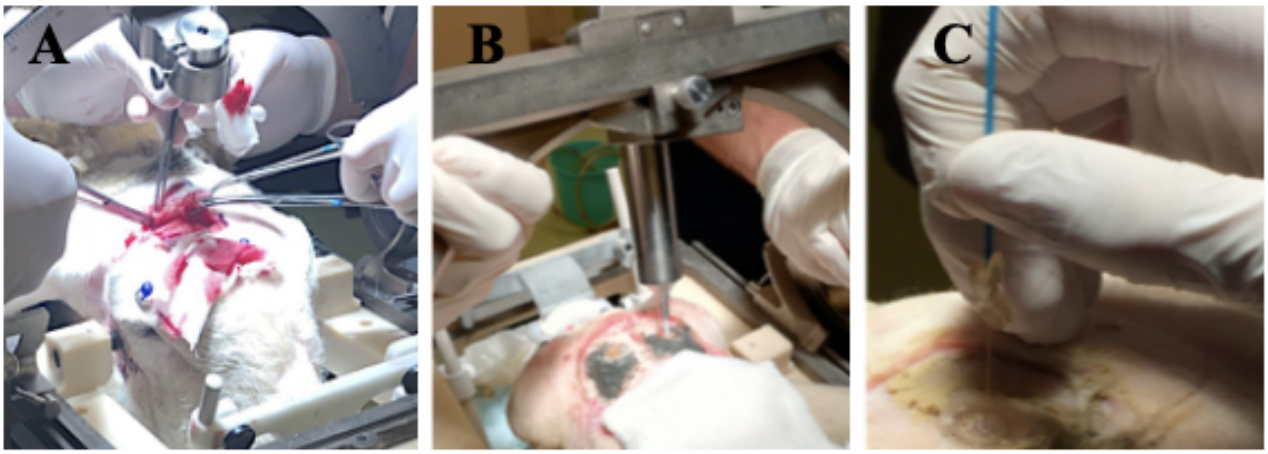

Figure 36. A, B) Stereotactic insertion of the guide catheter, after surgical procedure and placemen of the ports; C) Manual insertion of the infusion silica catheters.

5- Infusions and acquisitions at consecutive timepoints

The 'Pump 11 Elite & Pico Plus' from 'Harvard Apparatus' was used to infuse 10µL of a Gadolinium-based solution composed of Prohance® (Gadoteridol) diluted 1:80 in physiologic solution, at rate of 3µL/min at the level of the previously described CST target. A dedicated extension tube of 1.5 m (diameter 1 mm) connected the syringe to the infusion silica catheter, and air bubbles within both the syringe and the extension were carefully removed before infusion, in order to avoid any artefact caused by air. The total infusion duration was 3 minutes and 20 seconds. Due to experimental contingencies and time constraints, post-infusion acquisitions were acquired at slightly different timepoints across different sheep, resulting in a minimum of 1 and a maximum of 4 post-infusion acquisitions. Two infusions were made in each sheep, one in every hemisphere. Infusion details for each sheep are showed in Table 2, where the number of timepoints, infusion directions and timings are described. The timing is defined as the time interval between the end of the infusion procedure and the end of 3DT1 acquisition.

	CST	Timepoints Number	Timing (min)	Infusion Direction
SHEEP 08	L	3	20, 60, 90	∥
	R	1	10	
SHEEP 09	L	2	10, 25	∥
	R	3	15, 50, 65	
SHEEP 10	L	2	20, 65	∥
	R	1	15	
SHEEP 11	L	2	70, 90	∥
	R	2	15, 35	
SHEEP 12	L	3	20, 50, 90	⊥
	R	3	20, 50, 90	
SHEEP 13	L	3	20, 50, 90	⊥
	R	3	20, 50, 90	⊥
SHEEP 14	L	3	25, 55, 85	⊥
	R	4	25, 60, 90,120	

Table 2. Timepoints acquisition parameters. L and R indicate Left and Right respectively. Parallel infusion direction is represented by ∥ while orthogonal infusion is represented by ⊥.

Post-infusion image pre-processing

After the acquisition of raw data, the post-infusions images were pre-processed in order to allow intra-sheep image comparisons and to guarantee inter-sheep homogeneous data handling. In particular, for each single sheep, all the post-infusion images were aligned (coregistered) to the preoperative 3DT1 image, always kept as reference image because both the presurgical tractography and planning have been performed on it. On the other hand, for all the sheep, a common cutoff was maintained when automatic segmentations were performed. Fourteen infusions were completed, 8 with the catheter parallel to white matter fibers, 6 with the catheter orthogonal to them. In the following paragraphs, programs and methodologies used in image pre-processing will be detailed.

6A-Coregistration

For each sheep, post-infusion images were co-registered to the preoperative 3DT1 image by means of the FLIRT tool of FSL, in order to create a dataset in which the intra-sheep space was the same. Different spaces of the raw images belonging to the same sheep depended on the repeated positioning of the animal in the MRI scanner and, most importantly, by the brain shift caused by surgery. The parameters of the function[5] used are:

- *Bins*: Histogram values were calculated in a 256 gray-level scale;
- *Cost normmi*: cost function, set to 'normmi' (Normalized Mutual Information);
- *Searchrx/y/z*: angular range in each axes over which the initial optimization search is performed;
- *Interp*: interpolation method used in the final slice transformation, set to 'tri-linear';
- *Omat*: transformation matrix.

Once the images were coregistered, the raw b-vectors table was rotated in relation to the transformation matrix (DTI to 3DT1) in order to ensure correct tensor data extraction; This rotation

---

[5] *flirt -in SheepN°_3DT1timepoint.nii -ref SheepN°_3DT1preOP.nii.gz -out SheepN°_timepoint _to_3DT1preOP.nii -omat SheepN°_scan1_to_preOP.mat -bins 256 -cost normmi -searchrx -90 90 -searchry -90 90 -searchrz -90 90 -dof 6 -interp trilinear*

was obtained by the multiplication between the transformation matrix, obtained from DTI (b=0 volume) to the 3DT1 image, and each 3D vector of the 'bvecs' file. Subsequently, diffusion maps were extracted from the DTI raw data.

6B- Intensity Normalization and Bet

FSL visualization of post-infusion acquisitions highlighted different voxel intensities between intra-sheep 3DT1 images. The MRI voxel intensities do not have a fixed numerical value associated to a particular tissue, even within the same MRI protocol, for the same body region, and even for images of the same subject obtained on the same scanner at different timepoints [122].
Thus, an intensity-normalization of all 3DT1 images was necessary in order to estimate consistently and reproducibly the differences in gadolinium intensity and to perform correct automatic procedures. The open source software *'ITK-SNAP'* (http://www.itksnap.org/pmwiki/pmwiki.php) was used to create a mask on the preoperative 3DT1, in a region of homogeneous intensity in the temporal muscle. The optic chiasm was identified on the coronal plane (Fig. 37A) as the crossing point of the optic nerves, and, at this level, a cubic mask was extracted in the temporal muscle, as it is visible bot in the coronal (Fig. 37A) and axial plane (Fig. 37B).

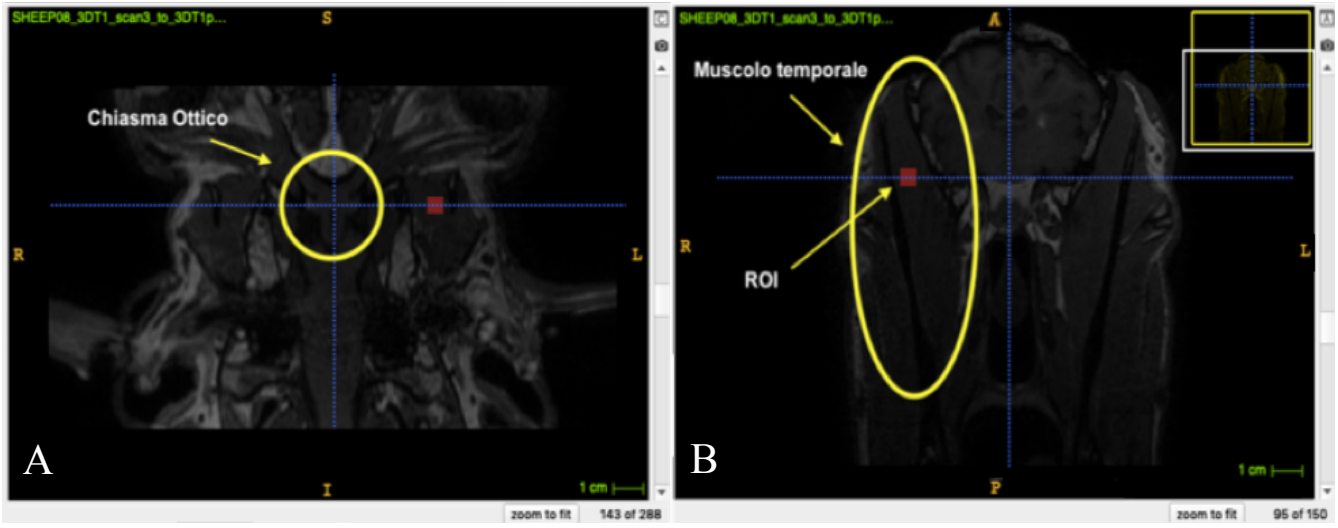

Figure 37. Identification of the optic chiasm in the coronal plane (A) and creation of a mask in of the temporal muscle region in the axial plane (B).

FSLview was used to double-check that the 3D mask was within the very same region of the temporal muscle in all post-infusion images as in the pre-operative 3DT1, but it was already expected given that all the images have already been coregistered to the preoperative 3DT1. Thus, the temporal

muscle mask was multiplied by every post-infusion image, and average values of voxel intensity within the temporal muscle was obtained through FSL. By dividing each post-infusion 3DT1 image by its corresponding average value in the temporal muscles, intensity-normalization between images was achieved and standardization of the intensities was obtained.

Finally, ovine brain masks were obtained by using the FMRIB Software Library brain extraction tool (BET[6]), setting fractional intensity threshold function at 0.4, and manually refined with ITK-SNAP (version 3.6.0). They were eventually multiplied voxel-by-voxel to the original 3DT1 images using the "Fslmaths" tool of FSL, in order to extract the whole brain of each sheep (Fig.38).
The pre-processed dataset of pre- and post-operative images, therefore, resulted in the 3DT1-preoperative space, intensity-normalized and bet.

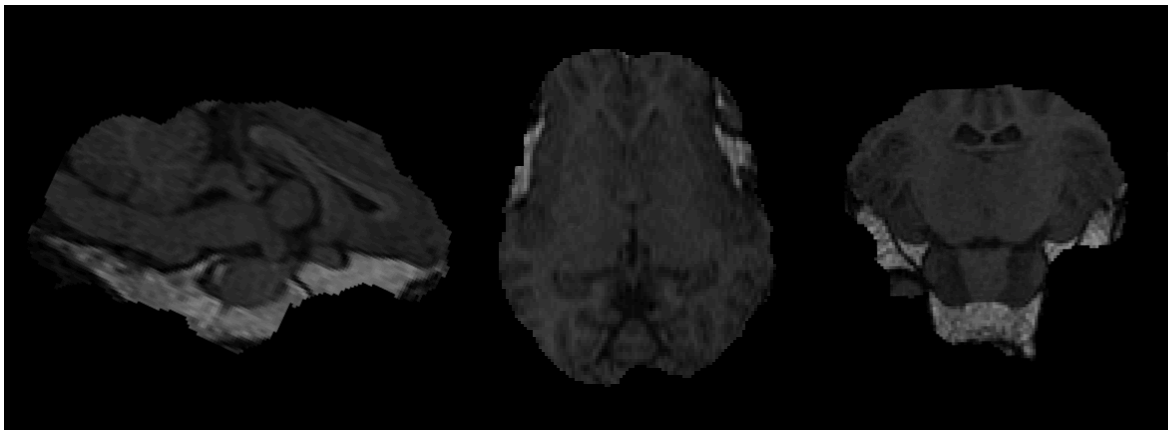

Figure 38. Skull removal using a mask created with ITK-snap. The brain is relative to sheep 11.

6C- Automatic segmentation of infusion

An automatic segmentation algorithm ('*Region Growing'*) was created in *Matlab2019* (Matlab R2019a, Mathworks inc.), with the aim to extract the mask of the bolus of the gadolinium-based solution from all the post-infusion acquisitions of each sheep. The input parameters of the script are:

- Sheep under investigation: *sheepnumber*;
- Bolus maximum voxel intensity: *maximum*;
- Image range containing the bolus: *first_imm* e *second_imm*;

[6] *bet Sheepn°_3DT1_timepoint.nii.gz Sheepn°_3DT1_timepoint_bet.nii.gz -f 0.4 -R -m where -f 0.4 indicates the fractional intensity threshold, -R allows to iterate different time the brain Centre-Of-Mass resulting in a better brain extraction and -m generates binary brain mask*

Particularly, the last parameter was set in order to reduce the computational costs of the algorithm, being the images with the bolus about 10% of the total volume (Table 3).

Bolus maximum voxel intensity was found through *'ITK-SNAP'* by creating a square 3D mask of size 10 voxels that can incorporate the whole bolus in the first post-infusion volume for each sheep, as appreciable in Figure 39. Subsequently, the maximum voxel intensity within the mask was extracted by means of *FSL* (Table 3).

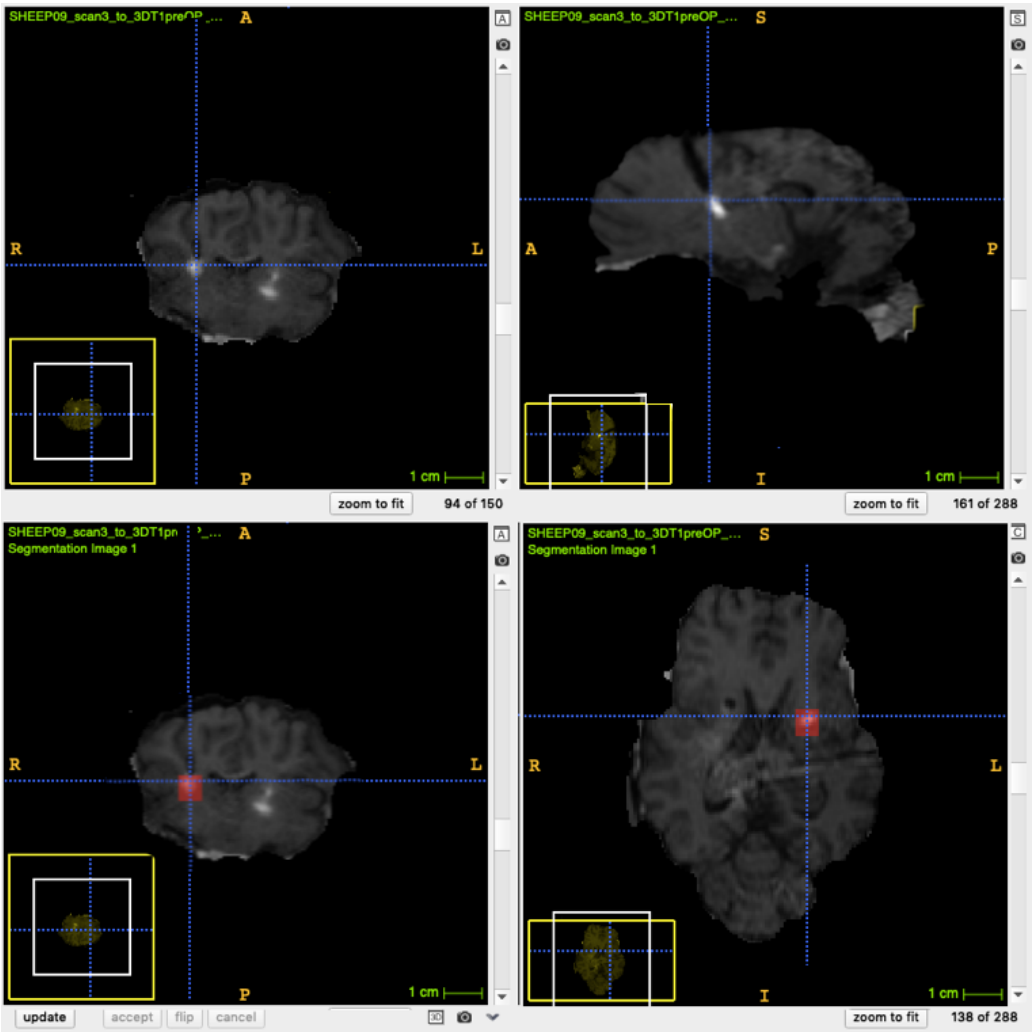

Figure 39. Identification of the regions containing the infusion bolus on ITK-SNAP.

The algorithm was instructed to limit the segmentations only to those voxels that displayed an intensity not inferior to the 33% of the maximum gadolinium intensity. Thus, until a 66% of intensity-decay, voxels were still automatically considered as part of the infused bolus, while voxels less intense than the threshold were not considered. This percentage was applied to all the maxima of different sheep, obtaining the thresholds for the automatic segmentation algorithm (Tab.7).

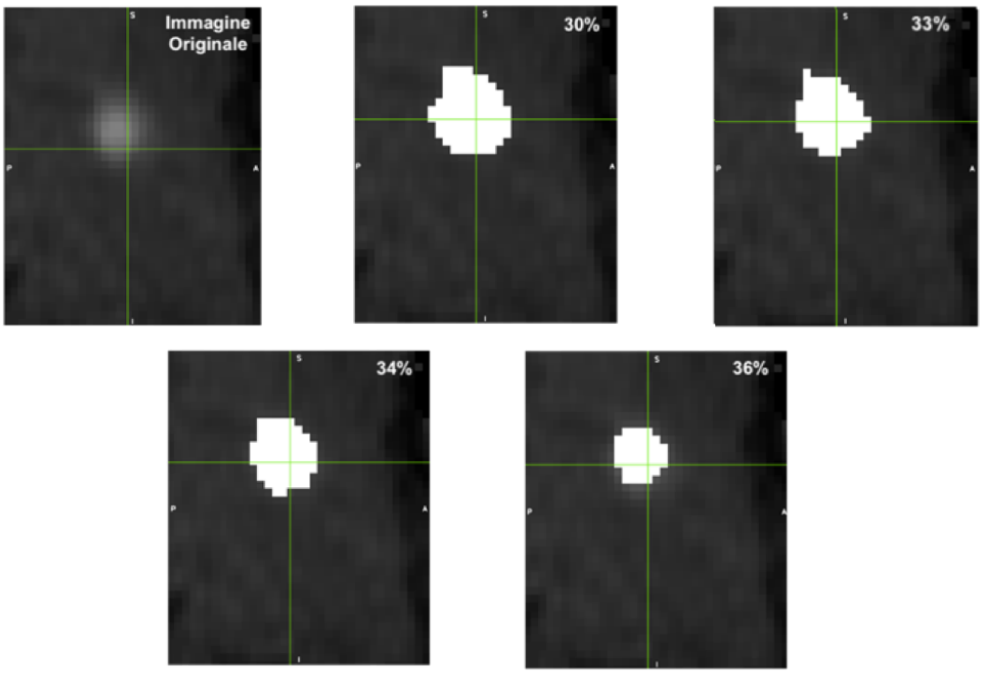

Figure 40. Mask visualization on FSLview for different threshold values. Threshold of 33% includes all the infusion bolus.

The *Matlab2019* code also allowed to save the bolus mask in '*Stereo lithography interface format'* (.stl) (Fig. 41) thanks to a function:

stlwrite (name, info, 'mode', 'ascii');

This function required different input such as name parameter to save the file with proper name, structure containing vertices and faces of the triangles that make up the surface of the bolus 'info', while the last two inputs were used to save the file in text format. The data contained in the 'info' structure were obtained from the *'isosurface'* function which required the set of images and a threshold. Since the binary masks were used, a threshold value of ½ has been set.

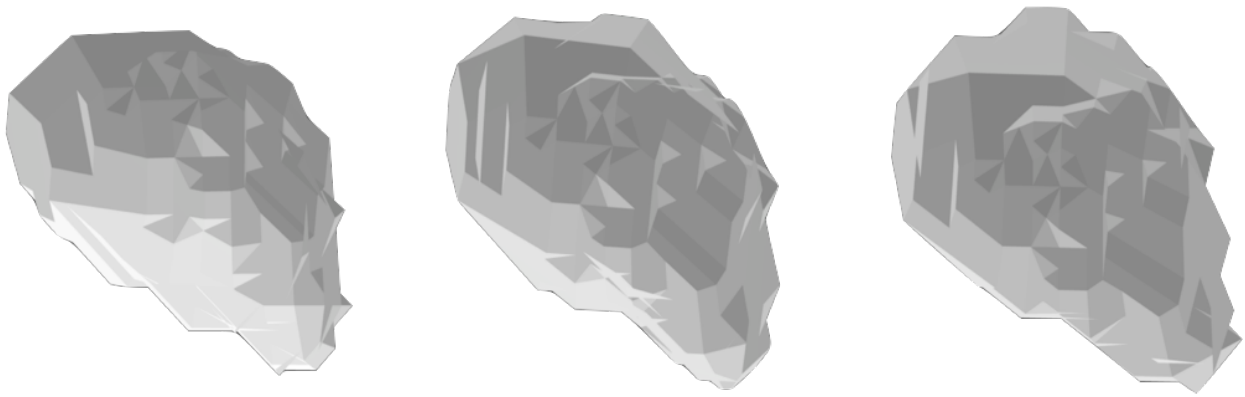

Figure 41. Graphical representation of MATLAB 'stlwrite' function. The image represent the .stl file converted by the binary mask.

6D- Catheter Segmentation

The last parameter needed to complete the dataset was the catheter shape estimation, obtained by semi-automatic segmentation by the '*3DSlicer*'tool *'Segment Editor',* that allowed to apply a voxel intensity threshold ranges and to manually crop the catheter shape (Fig. 42). In the following analysis, Catheter direction was extracted to differentiate between parallel and orthogonal infusions. Specifically, the catheter direction compared to CST fibers provided a more accurate indication of the actual orientation of the catheter with respect to the CST during pre-surgical step.

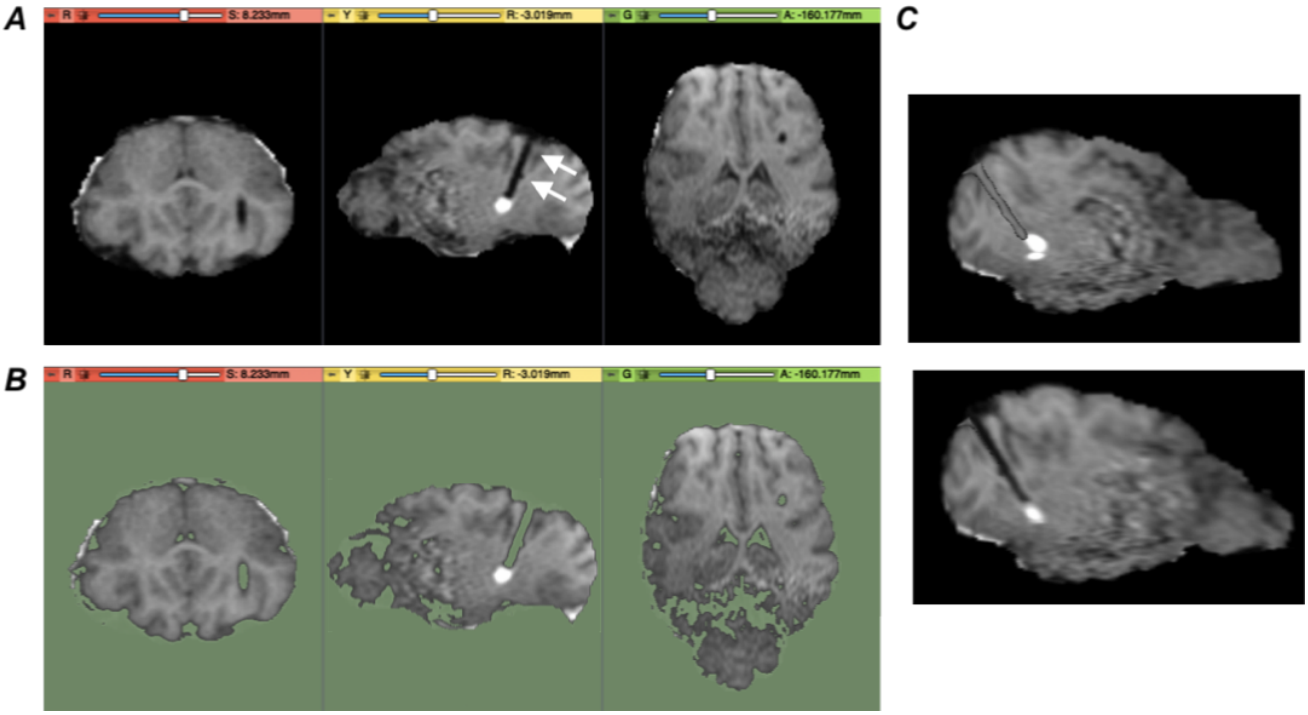

Figure 42. A) Post-infusion images with the catheter (white arrows) and its relative infusion; B) 3DSlicer segmentation through threshold range; C) Comparison between catheter segmentation and real catheter.

7A- Inclusion criteria for analysis

Not all the 14 (8 parallel and 6 perpendicular to CST) gadolinium-based infusions could be included in the definitive analyses, since the boli needed to fulfil the same inclusion criteria in order to guarantee homogenous and reproducible analyses. Two inclusion criteria were set, the first one based on a Fractional Anisotropy (FA) threshold, the second one based on explained variance. First, in order to be considered 'within the fibers', boli should display a mean FA that did not differ from the mean

FA of CSTs. This was carried out by multiplication[7] of FA maps with CST and bolus binary mask and next average[8] of not-zero voxels of the output by means of 'fslmaths'.

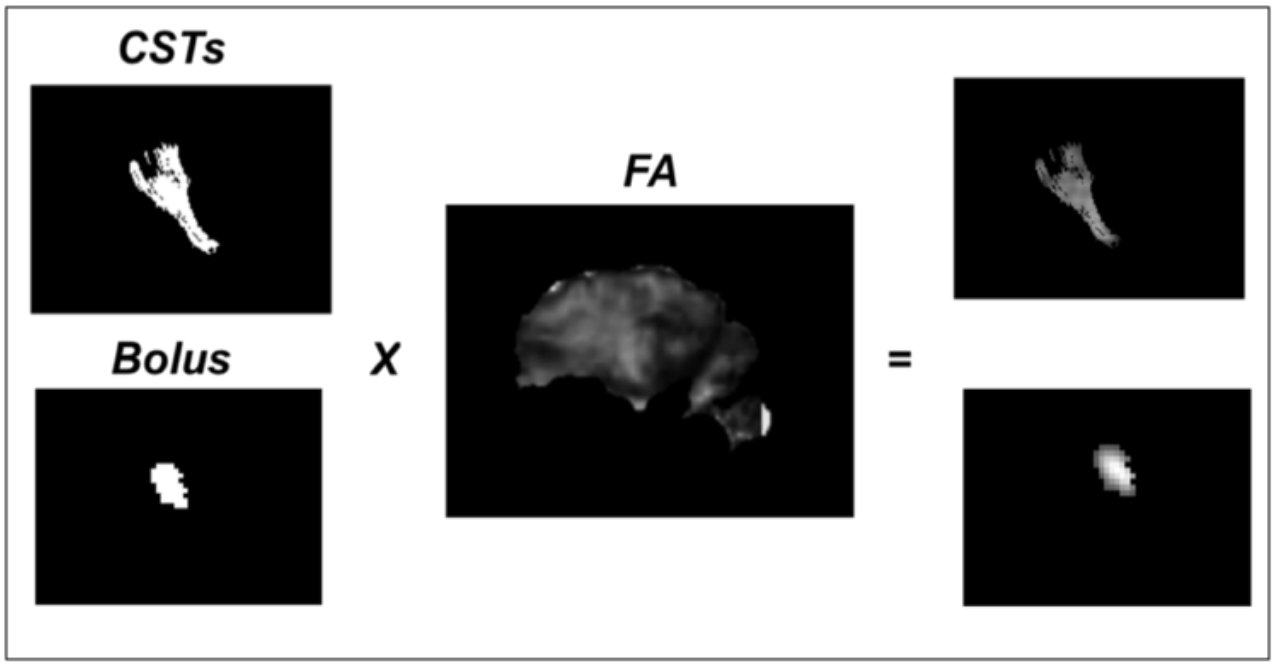

Figure 43. FSL process to extract FA mean value. After multiplication through fslmaths average of voxel greatest than 0 was carried out.

Second, in order for a 'principal' direction to be consistently identified within each bolus, boli should be unanimously oval. This inclusion criteria was set because subsequent studies were based on bolus principal component analysis. Accordingly, the explained variance (EV) of the principal components of all the boli needed to overcome the cutoff of 0.4 in order to be considered 'oval' and was calculated through the formula:

$$EV = \frac{Eigenvalue_{max}}{\sum_{i=1}^{3} Eigenvalue_i} \tag{28}$$

EV range is [0;1] where 0.33 indicates perfect sphere shape, so 0.4 is 20% more of the sphere shape. EV was calculated for each infusion at the first timepoints, still influenced by CED advective flow, while the shape of the boli through the next timepoints were influenced by diffusion motion only.

[7] *fslmaths SHEEP11_dti_FA_corr.nii -mul SHEEP11_LEFT_1st_timepoint_mask.nii SHEEP11_LEFT_1st_mask_FA.nii.gz*

[8] *fslstats SHEEP11_LEFT_1st_mask_FA.nii.gz -M*

Post-infusion image analyses

Post-infusion image analyses on the coregistered and intensity-normalized final dataset were completed by means of '*3DSlicer*' software, including a python module ('*Python interactor'* module) through which a python code created in collaboration with 'Politecnico di Milano' was launched for the analyses of every infusion at each timepoint. Post-infusion image analyses focused on different specific parameters based on the two experimental hypotheses (8-9 steps of workflow Fig.33):

1) Effects of microstructural constraints on diffusion;

2) Effects of catheter orientation on infusion.

Five 3D-vectors were extracted, one of which refers to the catheter direction, one refers to the principal component of the bolus at each timepoint, and 3 refer to the DTI-eigenvectors.
Catheter direction (*Cath_direction*) was obtained by computing the Principal Component Analysis (PCA) on the cloud of points making up the catheter (Fig.44 A).
PCA is capable to find the main direction of a cloud of points by finding the line that maximizes the sum of the squared distances between the projected points and the origin. After that, the second and third main directions are defined as the mutual perpendicular directions. In our experimental setting, the catheter was in a fixed position during the whole experiment duration, therefore *Cath_direction* vector remained constant for all the acquisitions at consecutive timepoints.
DTI eigenvectors ε_1, ε_2 and ε_3 and eigenvalues λ_1, λ_2, λ_3 were extracted only from the voxels situated in the portion of the tract overlapping with the infusion at the last timepoint. Once the voxels of interest were extracted from the DTI, the eigenvectors of each ellipsoid were weighted for the same-location FA voxel value, in order to give greater importance to the voxels with higher FA (and thus more probably within the tract) (Fig.44 B).
Finally, *ε_max_bolus* was the bolus principal components and it was obtained through PCA, the same method used for the extraction of *Cath_direction* (Fig.44 C) (Tab. 6). Bolus principal component was the only parameters that changed for every timepoint due to the bolus expansion during time.

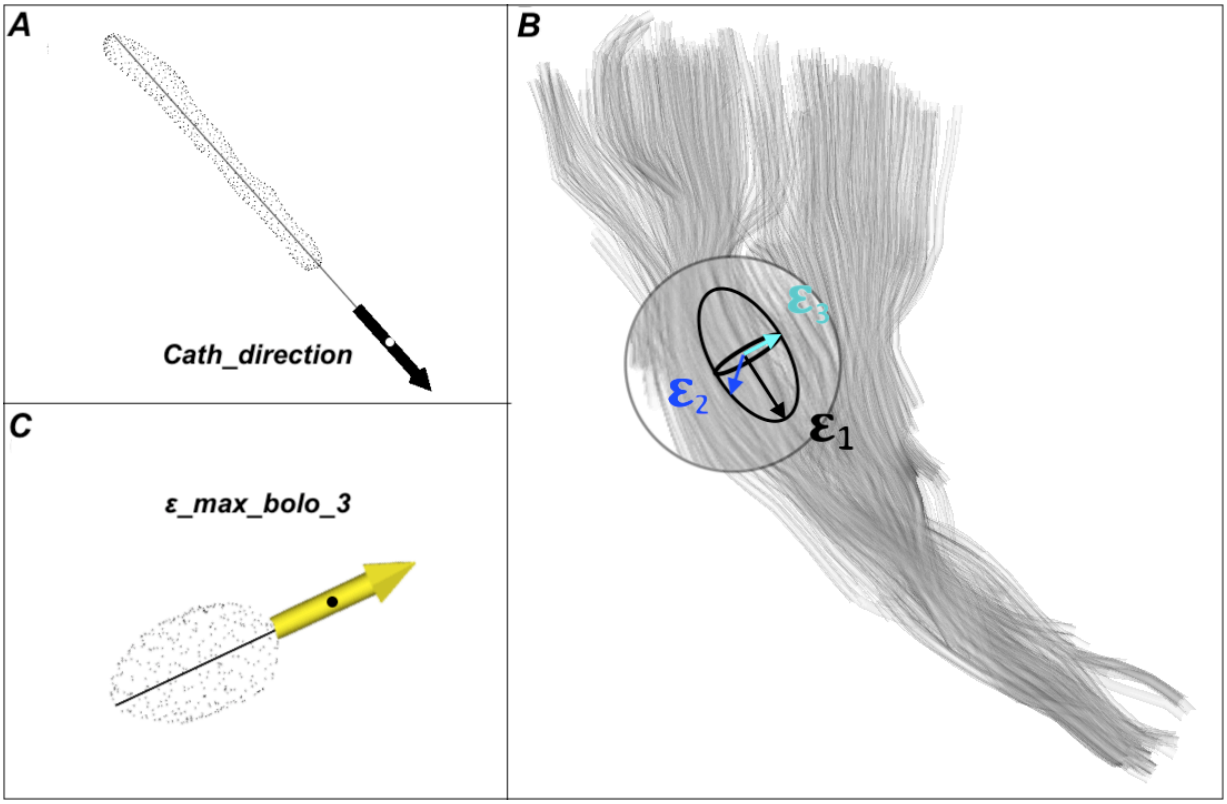

Figure 44. Parameter extraction. A) Cath_direction obtained by PCA calculation of points constructing catheter shape. B) Representation of tract to illustrate the DTI principal direction corresponding to the bolus position (ε_1, ε_2 and ε_3). C) Representation of ε_max_bolus_3, other parameters (ε_mid_bolus_3 and ε_min_bolus_3) are the second and third bolus principal components all respectively orthogonal.

Next, geometrical calculations between primary vectors allowed to obtain further parameters that were used for the analyses (Tab.2).

Particularly, in order to answer the experimental questions, absolute bolus lengths in the three DTI principal components (L) were extracted, as well as angles between DTI principal components and the PCA of the boli of the same sheep (Ω). Furthermore, differences in L were calculated in order to obtain the *delta* (ΔL) between the last timepoints and the first ones for each infusion, in order to calculate the elongation of the bolus during time.

1	Parameter Names	Description
	$\boldsymbol{\varepsilon}$**_max_bolus**	PCA relative to the maximal direction of the bolus
	Cath_direction	PCA relative to the catheter direction
	$\boldsymbol{\varepsilon_1}$	Primary eigenvector relative to the DTI voxels corresponding to the location of the infusion bolus at the last timepoint acquired at MRI
	$\boldsymbol{\varepsilon_2}$	Secondary eigenvector relative to the DTI voxels corresponding to the location of the infusion bolus at the last timepoint acquired at MRI
	$\boldsymbol{\varepsilon_3}$	Secondary and minimal eigenvector relative to the DTI voxels corresponding to the location of the infusion bolus at the last timepoint acquired at MRI
2	**Combination of Extracted Parameters**	
	$\boldsymbol{\Omega\_\varepsilon_1}$	Angle between ε_max_bolus and ε_1 [°]
	$\boldsymbol{\Omega\_\varepsilon_2}$	Angle between ε_max_bolus and ε_2 [°]
	$\boldsymbol{\Omega\_\varepsilon_3}$	Angle between ε_max_bolus and ε_3 [°]
	$\mathbf{L\_}\boldsymbol{\varepsilon_1}$	Absolute bolus length in the direction of ε_1 [mm]
	$\mathbf{L\_}\boldsymbol{\varepsilon_2}$	Absolute bolus length in the direction of ε_2 [mm]
	$\mathbf{L\_}\boldsymbol{\varepsilon_3}$	Absolute bolus length in the direction of ε_3[mm]
	$\boldsymbol{\Delta L\_\varepsilon_1}$	Bolus elongation between consecutive timepoints and the first timepoint in the ε_1 direction [mm]
	$\boldsymbol{\Delta L\_\varepsilon_2}$	Bolus elongation between consecutive timepoints and the first timepoint in the ε_2 direction [mm]
	$\boldsymbol{\Delta L\_\varepsilon_3}$	Bolus elongation between consecutive timepoints and the first timepoint in the ε_3 direction [mm]

Table 3. 1) Parameters extracted from the Final dataset by means of '3DSlicer' software through python script. 'Parameters Name' indicates the name of each parameters that is kept in the Result chapter. Cath_direction and ε_1, ε_2 and ε_3 are constant parameters while $\boldsymbol{\varepsilon}$_max_bolus changes for every timepoint. All of these parameters are 3D vectors. 2) Combinate parameters are calculated in the DTI main principal components, therefore their name include ε_1, ε_2 and ε_3 depending on the direction.

8- Extraction of parameters important to study the effects of microstructural constraints on diffusion: boli infused parallel and orthogonal to CST have been studied together

The *delta length (ΔL)* was calculated as the difference in absolute bolus length between consecutive timepoints in each DTI direction, taking the length of the first timepoint as a reference. In this regard, infusions that were analyzed by MRI imaging at one timepoint only were excluded from this analysis. Particularly, the infusion performed in the right hemisphere of sheep 8 and 10 was excluded by this analysis.

For the analyses, infusions parallel and orthogonal to CST could be considered all together because, after stopping CED, diffusion can be considered as the only force influencing the infusate diffusion (no more advection). The calculated *ΔL* for each infusion were plotted and then interpolated, through *Matlab2019* '*fit'* function, in each of the DTI components, as a linear function. Linear and quadratic interpolation has the same R^2, demonstrating that in a short time window, delta as a function of time can be represented by a line. What it is expected is that, due to lower flow resistance along the fiber direction, the diffusion velocity will result grater along the ε_1 rather than along ε_2 and ε_3.

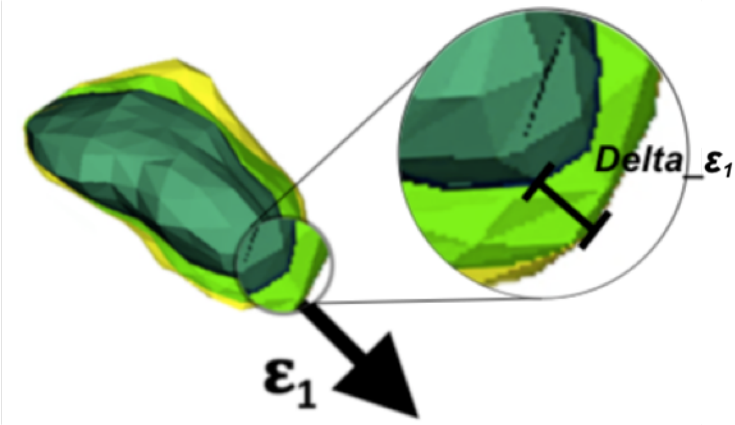

Figure 45. Visual representation of Delta between first and second timepoint along the principal component of the DTI. The bolus at 1st ,2nd and 3rd timepoints relative to parallel infusions (sheep 8,9,10 and 11) are represented through green, light green and yellow.

9- Extraction of parameters important to study the effects of catheter orientation on infusion: boli infused parallel to CST have been compared to boli infused orthogonal to CST

Angles Ω_ε_1, Ω_ε_2 and Ω_ε_3 represented the angles between each DTI principal component (ε_1, ε_2 and ε_3) and the bolus PCA (ε_max_bolus). They were calculated for each timepoint. Angles Ω were

calculated as the angle included between two 3D vectors through the formula (i.e. DTI main direction and bolus principal component):

$$\Omega = \cos^{-1}\left(\frac{\overrightarrow{\varepsilon_1} \cdot \overrightarrow{\varepsilon\_\max\_bolo}}{\|\varepsilon_1\| \ \|\varepsilon\_\max\_bolo\|} \right) \quad \text{(XX)}$$

On the other hand, L_ε_1, L_ε_2 and L_ε_3 indicated the bolus lengths in the three DTI eigenvectors. These three lengths were measured by calculating the maximal Euclidian 3D distance between two points of the projected bolus along the three DTI eigenvectors.

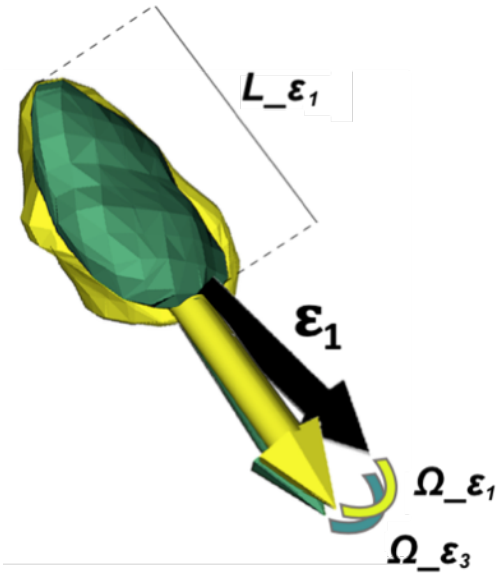

Figure 46. Visual representation of $L\_\boldsymbol{\varepsilon_1}$, $\Omega\_\boldsymbol{\varepsilon_1}$ and $\Omega\_\boldsymbol{\varepsilon_2}$. Green and yellow boli represent 1st ,2nd timepoint of parallel infusion respectively. $L\_\boldsymbol{\varepsilon_1}$ is the length of the $\boldsymbol{\varepsilon_1}$ DTI direction while $\Omega\_\boldsymbol{\varepsilon_1}$ is the angle included between bolus PCA at first timepoint and DTI main component. $\Omega\_\boldsymbol{\varepsilon_2}$ is the same as $\Omega\_\boldsymbol{\varepsilon_1}$ but referred at bolus PCA at second timepoint

The EVs that were calculated at the first timepoints for infusions parallel and orthogonal to CST were compared, in order to understand if the infusion directions affect the initial shape of the boli. Finally, angles between the main axis of the tensor and the bolus PCA (Ω_ε_1, Ω_ε_2 and Ω_ε_3) at the first and last time points were measured to evaluate the difference between parallel and orthogonal infusions and also to evaluate the alignment of the bolus to the CST fibers during time, both in cases of parallel and orthogonal infusions.

Statistical analysis

Statistical analyses were performed using Prism 8 (GraphPad Software). '*Shapiro-Wilk'* test (SWt) was used to study the normality distribution of the following data:

- L_ε_1, L_ε_2 and L_ε_3 for Parallel and Orthogonal infusion and for all the timepoints;
- Ω_ε_1, Ω_ε_2 and Ω_ε_3 for Parallel and Orthogonal infusion and for all the timepoints;
- Explained Variance (EV) for Parallel and Orthogonal infusion for the 1st timepoint only;

Since the distributions of lengths and angles were not normally distributed, non-parametric *'Wilcoxon matched-pairs signed rank test'* was applied to angles Ω and lengths L of the infusions parallel and orthogonal to CST. Non-parametric '*Mann-Whitney test'* was used to compare differences between parallel and orthogonal parameters.
Differently, *EV* data were normally distributed (SWt p-value for orthogonal = 0.83 , SWt p-value for parallel = 0.147). Due to different time-intervals between MRI acquisitions at consecutive timepoints, EVs of parallel and orthogonal infusions were compared by taking into account the time as a covariate, exploiting an *ANCOVA* test. *ANCOVA* assumption were respected [141]. Finally regression slopes were compared in GraphPad Prism 8 through linear regression analysis tool (ANCOVA test).

P-value < 0.05 was considered statistically significant.

Results

All animals successfully underwent preoperative 1.5T MRI according to the protocol described in the Methods, to guide the neurosurgical planning. DTI images were post-processed in all the seven animals, allowing the *in vivo* dissection of the corticospinal tract (CST) in each hemisphere of the ovine brain. DTI-based reconstruction of the CST was feasible in all the sheep and the course of the CST was reproducible and reliable across all the ovine animal model.

For each animal, CSTs were aligned to the preoperative 3DT1-FFE images and DTI-based planning of the neurosurgical procedure was performed for all the 14 infusions. Targeting the CST at the level of the internal capsule, the stereotactic placement of CED infusion catheters via a bespoke MRI-compatible ovine headframe and CRW stereotactic system was parallel to CST fibers in 8 cases and orthogonal to these in 6. A total of 10μL Gadolinium-based solution (Prohance®,1:80 in saline) was infused at rate of 3μL/min. 3DT1 preoperative images of each animal were taken as a reference space for all the DTIs and post-infusion images. Intra-sheep images were aligned to and normalized to a common baseline-intensity, to allow intra-sheep monitoring of infusate distribution over time. Before final analyses, automatic segmentation of infusions and inclusion criteria were applied to each infusion.

Automatic segmentation and Inclusion criteria

An automatic region-growing algorithm (Matlab R2019a, Mathworks inc.), instructed to limit the bolus segmentation only for voxels which intensity was not lower than 33% of the relative maximum, was applied at all the 14 infusions (Tab.7). In this way, binary masks of the infused boli were extracted. The 33% value was calculated as the average of the ROI maximum voxel intensity and manual minimum percentage (33.0% ± 3.28). This percentage was then applied to all the maxima, obtaining a standard procedure to find the growing thresholds for the automatic segmentation algorithm for all the post-infusion images.

Moreover, in order to guarantee homogeneous, reproducible and accurate analyses, bolus shape and location relative to DTI-based underlying tissue microstructure were evaluated, and two inclusion criteria (*FA* and *EV*) were defined in order to include the infused boli in the final analysis. In particular, a criterium was chosen in order to consider an infusion *within* the target or outside the target, due to the experimental inaccuracy of catheter positioning. As such, FA mean and standard deviation (SD) of the corresponding CSTs location were calculated (0.378 ± 0.026), then the mean

FA within each bolus at each timepoint was calculated by masking the FA map with the binary mask of the bolus, and if this value was lower than mean of CST - 2SD (i.e. 95.45% of the measurements), it was considered as outside the target. Particularly, three of the fourteen infusion resulted not completely in target (Tab.4), reducing the initial dataset to 11 infusions within the CST (6 parallel and 5 perpendicular).

Sheep N°	CST	CSTs FA mean	1st TP.	2nd TP.	3rd TP.	4th TP.
SHEEP08	L *	0.353	0,291	0,3039	0,323	--
	R		0,363	--	--	--
SHEEP09	L	0.409	0,524	0,519	--	--
	R		0,469	0,470	0,475	--
SHEEP10	L	0.351	0,402	0,380	0.351	--
	R		0,448	--	--	--
SHEEP11	L	0.392	0,572	0,529	--	--
	R*		0,304	0,315	--	--
SHEEP12	L	0.395	0,434	0,417	0,414	--
	R		0,416	0,411	0,410	--
SHEEP13	L	0.399	0,424	0,422	0,423	--
	R		0,356	0,362	0,358	--
SHEEP14	L*	0.348	0,250	0,257	0,259	--
	R		0,525	0,506	0,500	0,499

Table 4. Fractional anisotropy mean values along CSTs and within the boli. Asterisks (*) indicate the three infusions with FA mean value lower than CSTs mean - 2std, and thus considered outside the target.

According to the second criterium (*EV*), all the boli needed to have one of the principal components consistently greater than the other two. Therefore, boli required to overcome the cutoff of 0.4 of *EV* value in order to be considered 'oval'. This second criteria reduced the dataset to 10 definitive boli to be analyzed, 6 infused parallel and 4 infused perpendicular to CST fibers (Tab.5).
The three infusions not completely within the CST were excluded from the dataset and were analyzed separately from the infusions in-target.

Sheep N°	CST	1st TP.
SHEEP08	R	0.483
SHEEP09	L	0.543
	R	0.556
SHEEP10	L	0.536
	R	0.550
SHEEP11	L	0.668
SHEEP12	L	0.520
	R	0.467
SHEEP13	L*	0.380
	R	0.450
SHEEP14	R	0.498

Table 5. Explained variance of each bolus at first timepoint was calculated. Asterisks (*) indicates EV value lower than 20% of sphere shape (0.4).

Final dataset

The final dataset includes the following data for a total of 10 infusions (6 infused parallel to CST fibers and 4 perpendicular to them), that were intensity-normalized and coregistered to the reference 3DT1 pre-operative images (Tab.6). The dataset was composed by:

- Morphological volumes: 3DT1-FFE preoperative and post-operative consecutive scans, the latter acquired from 10 to 120 minutes after infusion;
- DTI *raw data* with their respective gradient values and directions, 'bvals' and 'bvecs' files;
- Fractional Anisotropy maps;
- Infusion boli in '.vtk'[9] format;
- Catheter segmentations in '.vtk' format.

[9] *Visualization toolkit format (.vtk) represents a geometric structure consisting of vertices, lines, polygons, and/or triangle strips. Point and cell attribute values are represented allowing simple analysis through Python programming.*

Sheep N°	CST	N° Timepoint	Direction
SHEEP08	R	1	‖
SHEEP09	L	2	‖
	R	3	‖
SHEEP10	L	2	‖
	R	1	‖
SHEEP11	L	2	‖
SHEEP12	L	3	⊥
	R	3	⊥
SHEEP13	R	3	⊥
SHEEP14	R	4	⊥

Table 6. Final dataset: Parallel (‖) and (⊥) infusions.

Preoperatively, the most compact portion of the CSTs at the level of the internal capsule was targeted for the infusions. Principal Component Analysis (PCA) was used to calculate the main direction of the CST at this level. Combination of this data with the catheter direction allows to verify if the infusions were actually performed parallel or orthogonal to the CST. The angle between these two 3D vectors was calculated for each infusion and averaged for parallel infusions (Mean ± SD = 33.5° ± 16.1°) and orthogonal infusions (Mean ± SD = 78.9° ± 6.9°). Statistical comparisons of infusion direction in respect to CST fibers between parallel and orthogonal infusions (Fig.47) show a significant difference (P=0.0007, unpaired t-test).

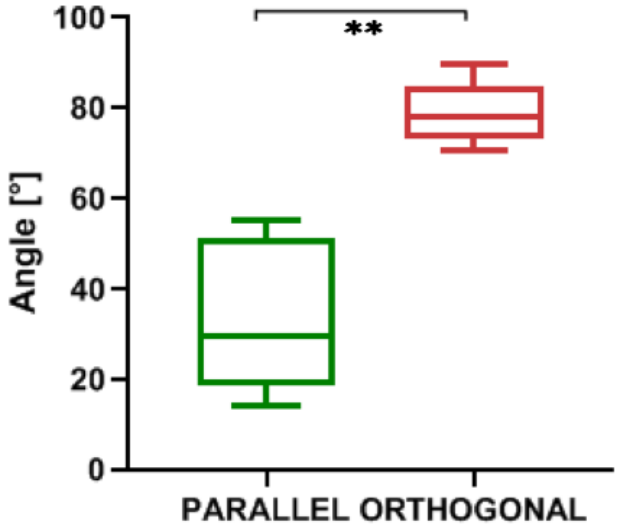

Figure 47. Angle between PCA of CST region and catheter direction. Green represent parallel infusion and red orthogonal ones.

	ROI Maximum voxel intensity		Manual minimum voxel intensity		Maximum Minimum percentage	Final Minimum		Image Range
SHEEP 08	LEFT	5.69	LEFT	1.80	31.61%	LEFT	1.72	[93; 107]
	RIGHT	7.89	RIGHT	2.83	35.86%	RIGHT	2.39	
SHEEP 09	LEFT	6.36	LEFT	2.53	39.75%	LEFT	1.92	[86; 101]
	RIGHT	5.17	RIGHT	1.48	28.72%	RIGHT	1.50	
SHEEP 10	LEFT	5.44	LEFT	1.69	31.09%	LEFT	1,65	[87; 99]
	RIGHT	5.17	RIGHT	1.57	30.41%	RIGHT	1.56	
SHEEP 11	LEFT	5.14	LEFT	1.47	28.56%	LEFT	1.55	[94; 107]
	RIGHT	8.00	RIGHT	3.05	38.12%	RIGHT	2.42	[89; 103]
SHEEP 12	LEFT	5.61	LEFT	1.85	33.00%	LEFT	1.70	[64; 81]
	RIGHT	5.52	RIGHT	1.90	34.5%	RIGHT	1.67	[71; 86]
SHEEP 13	LEFT	7.31	LEFT	2.54	34.81%	LEFT	2.21	[78; 94]
	RIGHT	5.55	RIGHT	1.71	30.83%	RIGHT	1.68	[83; 97]
SHEEP 14	LEFT	5.85	LEFT	1.90	32.5%	LEFT	1.77	[61; 84]
	RIGHT	5.91	RIGHT	1.89	31.95%	RIGHT	1.79	[66; 83]

Table 7. For each infusion, the maximum voxel intensity was measured by FSL and relative minimum voxel intensity was detected by visual inspection. Calculation of percentage between maximum and minimum voxel intensity was measured (Maximum-minimum percentage). Total percentage average was calculated (33.0% ± 3.28) and applied to all the maxima. Last column indicates the slice interval within which the bolus intensity was identifiable.

Infusate distributions within white matter fibers

Differences in the elongation of boli (ΔL), defined as the bolus elongation between consecutive timepoints and the first timepoint in the DTI main directions, were studied taking into account parallel and orthogonal infusion together under the assumption that only diffusion phenomenon was present. Each pair or triad of delta (ΔL_ε_1, ΔL_ε_2 and ΔL_ε_3) were plotted through the color-code relative to the three DTI directions (black, blue and cyan) while different markers were assigned to each sheep. Particularly, empty markers were assigned to parallel infusion while filled markers were relative to orthogonal infusions (Fig.48). Next, points relative to each DTI direction were fitted by linear interpolations of each ΔL in each direction and linear equations were compared. The slope of the line interpolating ΔL along ε_1 (black) is not statistically different from slope of the line interpolating ΔL along ε_2 (blue) (P=0.722, ANCOVA test) and from slope of the line interpolating ΔL along ε_3 (cyan) (P=0.741, ANCOVA test) for all infusions (Fig.48).

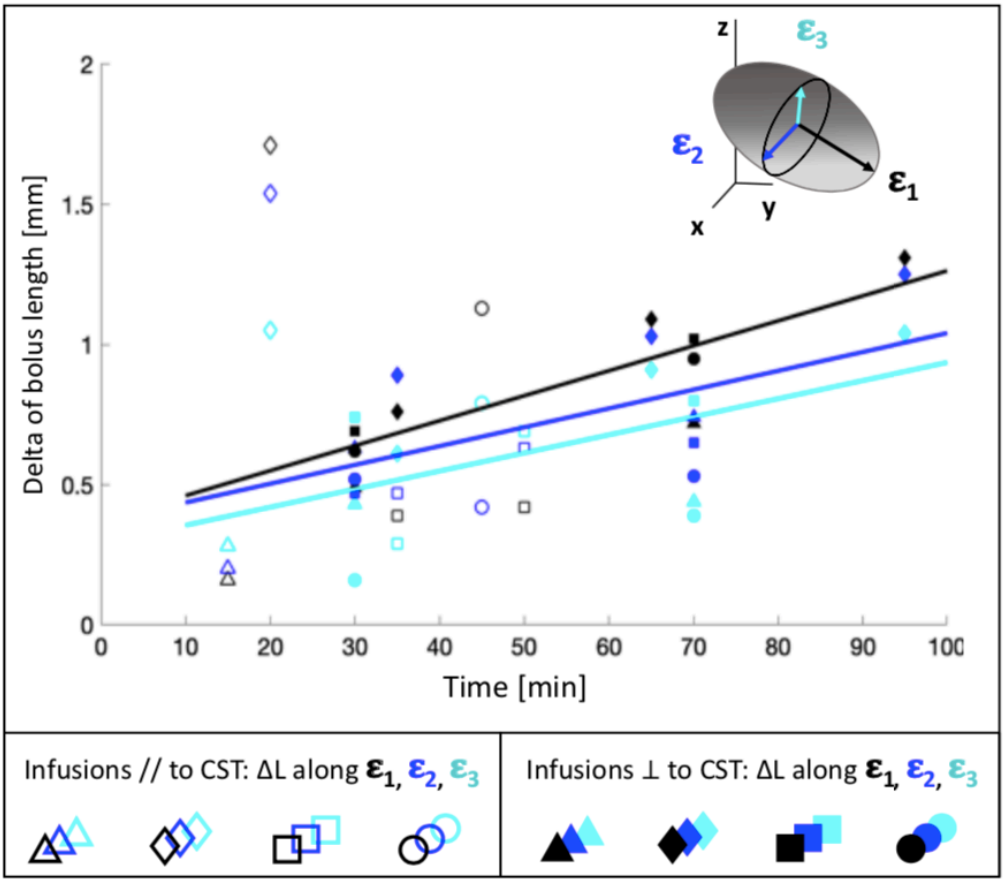

Figure 48. Differences in the elongation of the boli (delta lengths, ΔL) with respect to the first timepoint along DTI ε1, ε2, ε3. Different markers represent each animal (empty markers for parallel infusions and filled markers for orthogonal infusions) while the color-coding indicates DL along DTI main direction (ε1) in black, ΔL along ε2 in blue and ΔL along ε3 in cyan.

	ΔL_ε_1	ΔL_ε_2	ΔL_ε_3
Line equation ($x = \Delta L$ and $y = time$)	$y = 0.5346\ x + 0.372$	$y = 0.4027\ x + 0.369$	$y = 0.3871\ x + 0.29$
Linear interpolation Slope $\left[\frac{mm}{h}\right]$	0.5346	0.4027	0.3871

Table 8. Linear interpolation slopes of ΔL_ε_1, ΔL_ε_2 and $Delta\_\varepsilon_3$ indicated as $\left[{}^{mm}/_{h}\right]$. $\Delta L\ \_\varepsilon_1$ is greater than $\Delta L\ \_\varepsilon_2$ and ΔL_ε_3. R2 value is 0.25 for ΔL_ε_1 while it is 0.19 and 0.26 for ΔL_ε_2 and ΔL_ε_3 respectively.

Different slopes could be attributed to the anisotropy of fiber tracts, with high hydraulic conductivity along the axial fiber direction (ε_1) with respect to the radial (ε_2 and ε_3) ones.

Effects of catheter positioning on infusate distributions

Comparisons between infusions delivered parallel and orthogonal to white matter fibers allowed to define the effects of catheter positioning on Gadolinium distribution. This was evaluated through the analysis of the Explained Variance (EV), bolus lengths (L) and angles between DTI ε_1 and bolus principal component (Ω).

1- Explained Variance (EV) at first timepoint

As for the EV, the first timepoint was analyzed as it was the most influenced by the advection phenomenon of CED in respect to successive timepoints. Comparisons of EV at first timepoint between infusions delivered parallel and orthogonal to CST revealed that boli has an oval shape in both cases, but the former displays higher EV values, showing significant statistical difference between parallel (Mean ± SD = 0.55 ± 0.60) and orthogonal (Mean ± SD = 0.48 ± 0.31) infusions (P=0.008, ANCOVA test). Indeed, parallel bolus shape at first timepoint is more elongated than orthogonal one in the WM main direction (Fig.49).

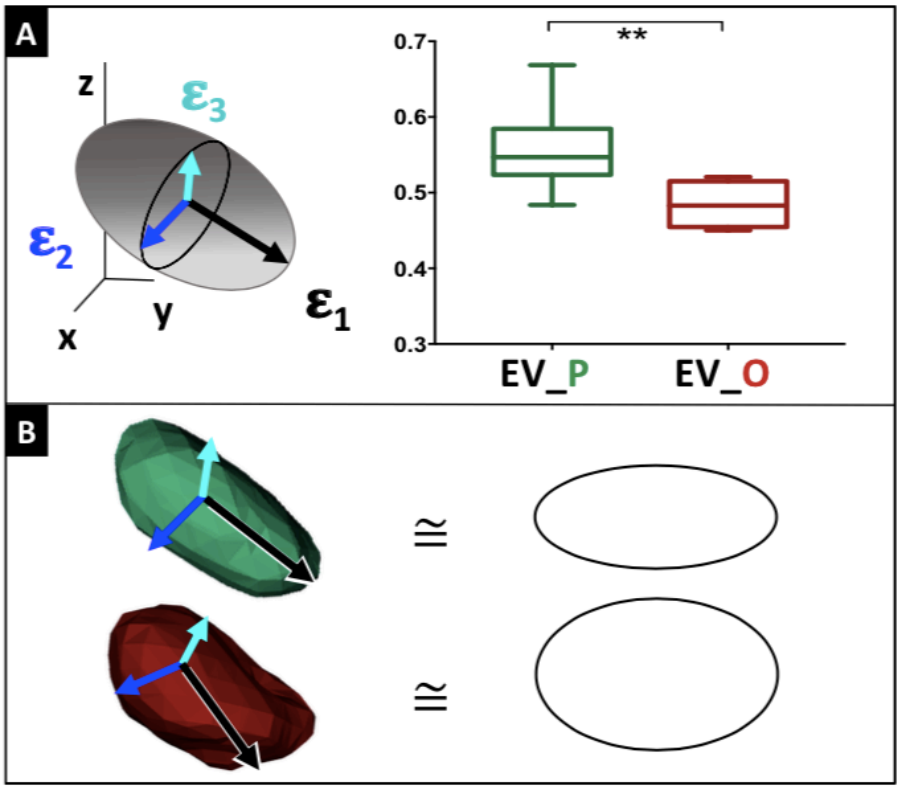

*Figure 49. Explained Variance (EV) of the boli parallel (green) and orthogonal (red) to the CST fibers at the first timepoints, showing that boli had an oval shape in both cases (A), but the former displayed higher EV (B), thus resulting significantly more elongated. (**$P \leq 0.01$).*

2- *Absolute Lengths L_ε_1, L_ε_2 and L_ε_3 at first and last timepoint*

Absolute lengths $L\_\varepsilon_1, L\_\varepsilon_2$ and L_ε_3 indicate the bolus lengths in the three DTI principal components. At first timepoint, L_ε_1 of parallel infusions (median=7.55 mm, range:[6.29-8.01]) appears significantly greater than L_ε_2 (median=5.49 mm, range:[4.14-6.49]) and L_ε_3 (median=5.63 mm, range:[4.13-6.07]) (L_ε_1 *vs* L_ε_2: P=0.031, L_ε_1 *vs* L_ε_3: P=0.031 at first timepoint, Wilcoxon test). The same trend can be observed in parallel infusions at last timepoint, with the same statistical significance level (L_ε_1 *vs* L_ε_2: *P=0.031*, L_ε_1 *vs* L_ε_3: P=0.031 at last timepoint, Wilcoxon test). (Fig.50A). On the other hand, orthogonal infusions exhibit a different behavior. At first timepoint, statistical comparisons between L_ε_1 of orthogonal infusions (median=6.48 mm, range:[5.7-6.88]), L_ε_2 (median=6.07 mm, range:[4.72-6.47]) and L_ε_3 (median=5.21 mm, range:[4.39-6.05]) were not significantly different at first timepoint (L_ε_1 *vs* L_ε_2: P=0.25, L_ε_1 *vs* L_ε_3: P=0.625 at first timepoint, Wilcoxon test) and neither in the last timepoint (L_ε_1 *vs* L_ε_2: P=0.125, L_ε_1 *vs* L_ε_3: P=0.125 at last timepoint, Wilcoxon test) (Fig.50B).

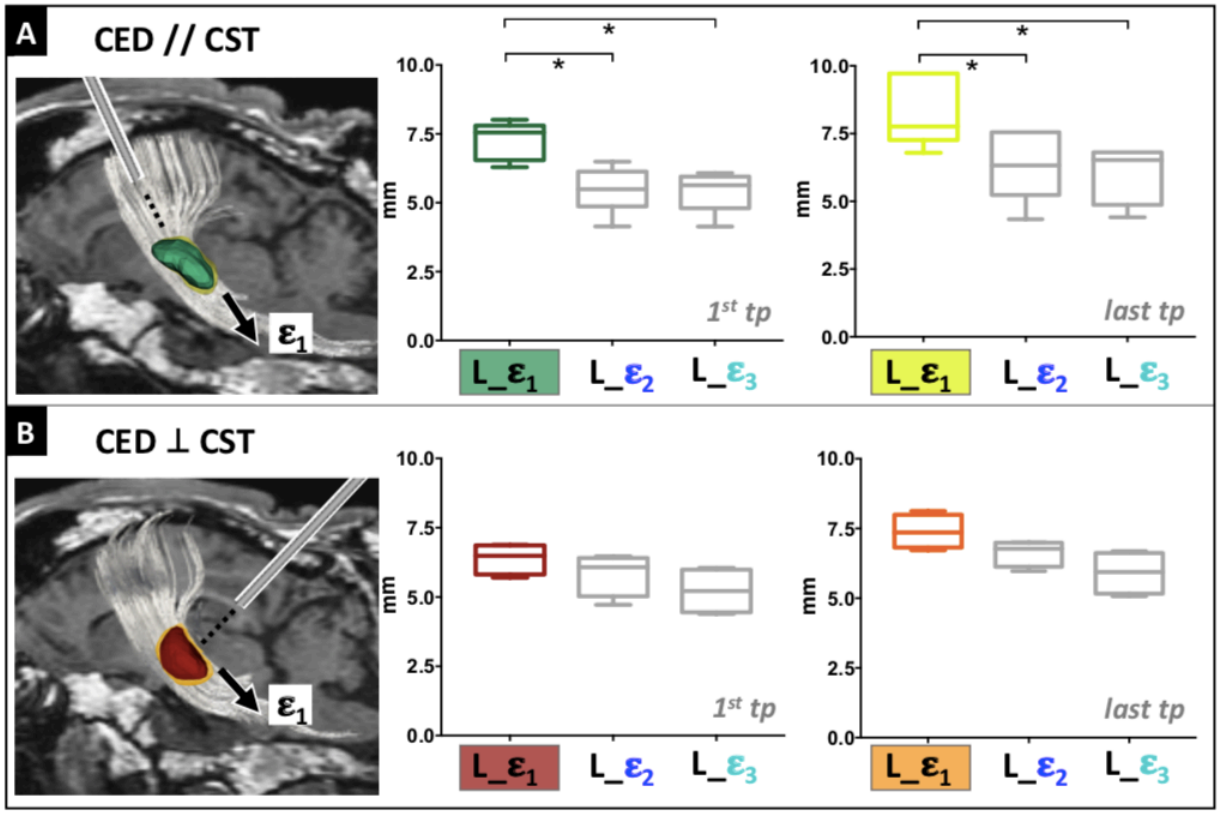

*Figure 50. A) Representation of a parallel infusion which include CST (in gray), catheter direction (black dotted line), DTI main direction ε_1 (black arrow), bolus at 1st timepoint (green) and bolus at last timepoint (yellow) overlaid to the morphological 3DT1 image. At first timepoint, boxplots show absolute lengths along DTI directions L_ε_1 (green), L_ε_2 and L_ε_3 (in gray). At last timepoint, boxplots show absolute lengths L_ε_1 (yellow), L_ε_2 and L_ε_3 (gray) (*P≤0.05, Wilcoxon test). B) Representation of an orthogonal infusion which include CST (in gray), bolus at 1st timepoint (red) and bolus at last timepoint (orange). At first timepoint, boxplots show absolute lengths L_ε_1 (red), L_ε_2 and L_ε_3 (gray). At last timepoint, boxplots show absolute lengths L_ε_1 (orange), L_ε_2 and L_ε_3 (gray).*

Statistical comparisons of absolute length between parallel and orthogonal infusions at first and last timepoint (Fig.51) was not statistical different (L_ε_1 for parallel vs L_ε_1 for orthogonal at first timepoint: P=0.114; L_ε_1 for parallel vs L_ε_1 for orthogonal at last timepoint: P=0.472, Mann-Whitney test). However, length L_ε_1 at first timepoint for parallel infusions (median=7.55 mm, range:[6.29-8.01]) is higher than L_ε_1 for orthogonal infusions (median=6.48 mm, range:[5.7-6.88]) while at last timepoint this difference become smaller (L_ε_1 at last timepoint for parallel median=7.76 mm, range:[6.79-9.72]; L_ε_1 at last timepoint for orthogonal infusions median=7.35 mm, range:[6.72-8.12]) (Fig.51).

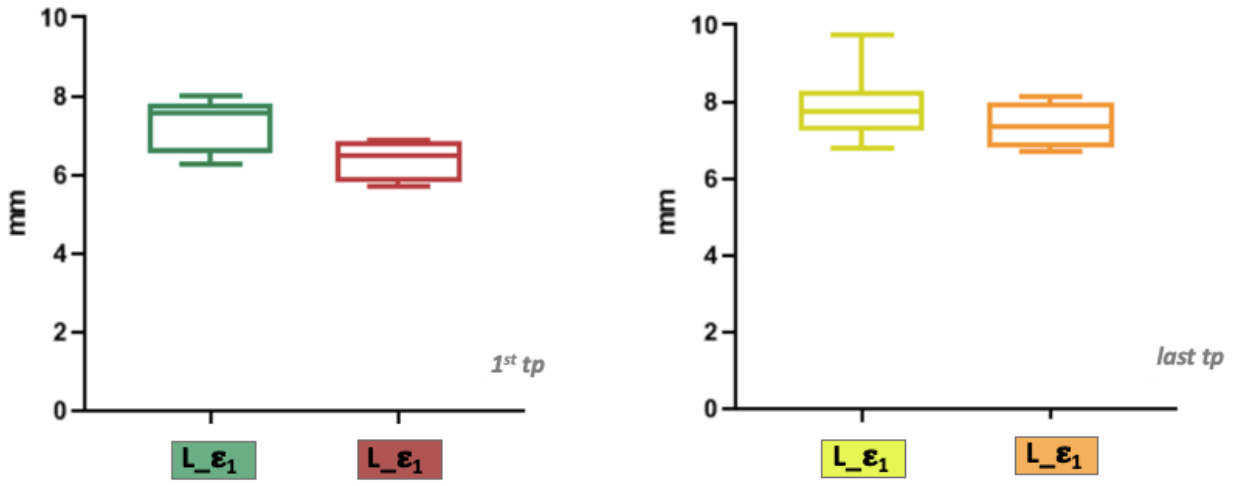

*Figure 51. Length along ε_1 for parallel and orthogonal at first (gray parallel and red orthogonal) and last (yellow parallel and orange orthogonal) timepoint. (*P≤0.05, Mann-Whitney test).*

3- *Angles Ω_ε_1, Ω_ε_2 and Ω_ε_3 at first and last timepoint*

Parameters Ω_ε_1, Ω_ε_2 and Ω_ε_3 represent the angles between bolus PCA and each DTI components. At first timepoint, the angle Ω_ε_1 of parallel infusions at first timepoint (median=25.43°, range:[7.88°-56.48°]) is significantly smaller than Ω_ε_2 (median=78.56°, range:[60.56°-87.77°]) and Ω_ε_3 (median=80.90°, range:[74.69°-89.51°]) (Ω_ε_1 vs Ω_ε_2: P=0.031; Ω_ε_1 vs Ω_ε_3: *P*=0.031, Wilcoxon test). Similarly, at last timepoint Ω_ε_1 (median=26.42°, range:[7.88°-52.14°]), Ω_ε_2 (median=71.44°, range:[55.9°-84.63°]) and Ω_ε_3 (median=69.35°, range:[79.09°-89.52°]) of parallel infusions present the same level of statistical significance (Ω_ε_1 vs Ω_ε_2: *P*=0.031; Ω_ε_1 vs Ω_ε_3: *P*=0.031, Wilcoxon test) and similar trend (Fig.52A). Conversely, orthogonal infusions exhibit a more uniform trend between the three DTI main directions. At first timepoint, the angle Ω_ε_1 of orthogonal infusions (median=54.58°, range:[16.61°-72.52°]) does not significantly differ from Ω_ε_2 (median=56.17°, range:[32.36°-82.82°]) and Ω_ε_3 (median=61.8°, range:[41.5°-85.2°]) (Ω_ε_1 vs Ω_ε_2: *P*=0.875; Ω_ε_1 vs Ω_ε_3: *P*=0.875, Wilcoxon test). At last timepoint, a trend toward a smaller Ω_ε_1 angle can be observed also in orthogonal infusion, as Ω_ε_1 median value decreases (median=44.59°, range:[14.41°-68.6°]), while Ω_ε_2 (median=62.01°, range:[35.50°-86.34°]) and Ω_ε_3 (median=69.54°, range:[44.64°-87.74°]) increase, although statistical comparisons do not reach significance (Ω_ε_1 *vs* Ω_ε_2: *P*=0.312; Ω_ε_1 *vs* Ω_ε_3: *P*=0.437, Wilcoxon test) (Fig.52B).

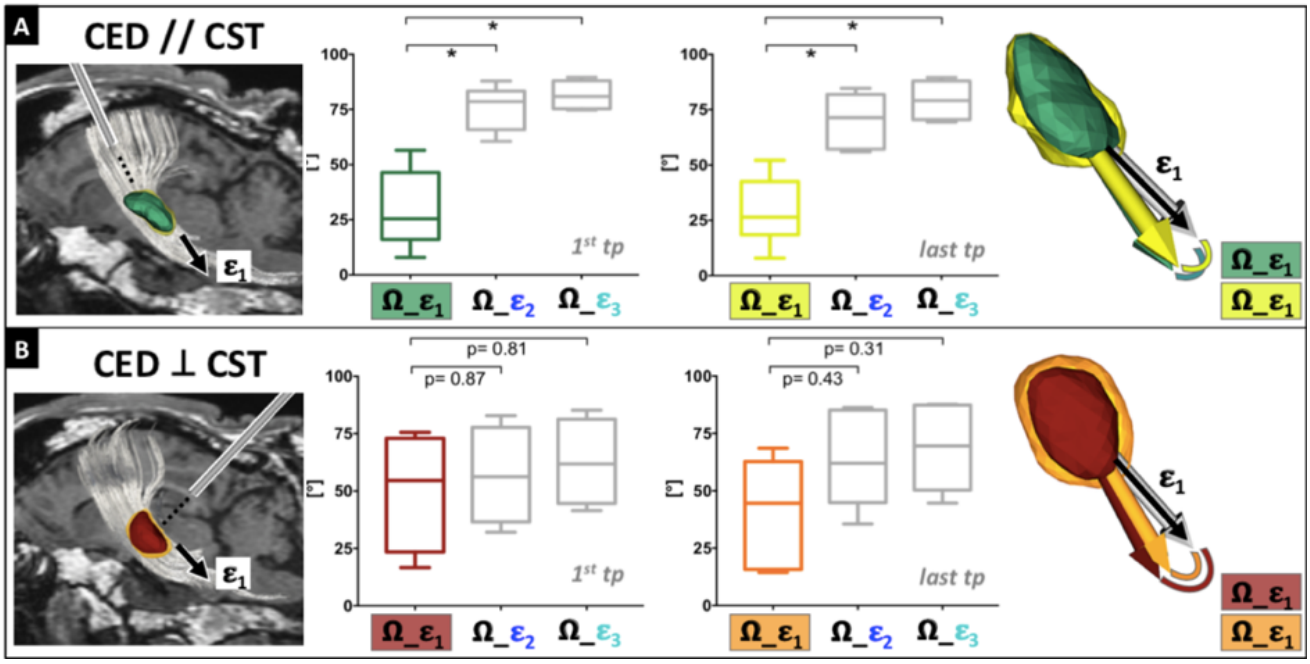

*Figure 52. A) Representation of a parallel infusion which include CST (in gray), catheter direction (black dotted line), DTI main direction ε_1 (black arrow), bolus at 1st timepoint (green) and bolus at last timepoint (yellow) overlaid to the morphological 3DT1 image. At 1st timepoint, boxplots show angles between bolus PCA and each DTI components Ω_ε_1 (green), Ω_ε_2 and Ω_ε_3 (gray). At last timepoint, boxplots show angles Ω_ε_1 (yellow), Ω_ε_2 and Ω_ε_3 (gray) (*P≤0.05, Wilcoxon test). B) Representation of an orthogonal infusion which include CST (in gray), catheter direction (black dotted line), DTI main direction ε_1 (black arrow), bolus at 1st timepoint (red oval) and bolus at last timepoint (orange). At last timepoint, boxplots show angles Ω_ε_1 (red), Ω_ε_2 and Ω_ε_3 (gray). At last timepoint, boxplots show angles Ω_ε_1 (orange), Ω_ε_2 and Ω_ε_3 (gray).*

Comparisons of angles between parallel and orthogonal infusions and DTI main direction (ε_1) were not significant in both first and last timepoint (Ω_ε_1 for parallel *vs* Ω_ε_1 for orthogonal at first timepoint: P=0.257*;* Ω_ε_1 for parallel *vs* Ω_ε_1 for orthogonal at last timepoint: P=0.536, Mann-Whitney test*)* (Fig.53).

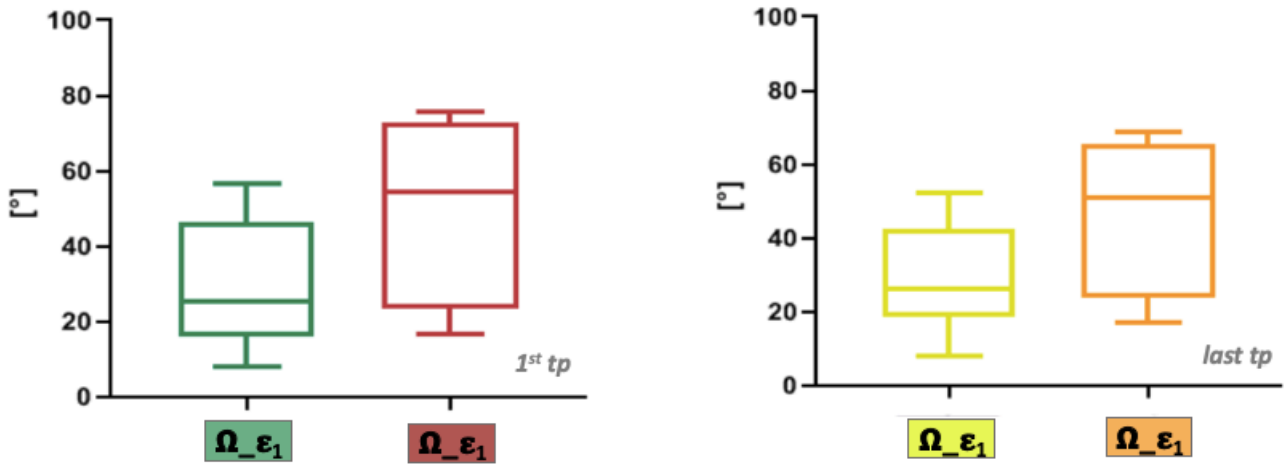

*Figure 53. Angles Ω along ε_1 for parallel and orthogonal at first (gray parallel and red orthogonal) and last (yellow parallel and orange orthogonal) timepoint. (*P≤0.05, Mann-Whitney test).*

Parallel (L)	Minimum	25% Percentile	Median	75% Percentile	Maximum
L_ε_1 1st TP [mm]	6.29	6.54	7.55	7.8	8.01
L_ε_2 1st TP [mm]	4.14	4.86	5.49	6.13	6.49
L_ε_3 1st TP [mm]	4.13	4.79	5.63	5.943	6.07
L_ε_1 last TP [mm]	6.79	7.26	7.76	9.72	9.72
L_ε_2 last TP [mm]	4.34	5.23	6.32	7.55	7.55
L_ε_3 last TP [mm]	4.41	4.86	6.52	6.81	6.81
Orthogonal (L)	Minimum	25% Percentile	Median	75% Percentile	Maximum
L_ε_1 1st TP [mm]	5.70	5.81	6.48	6.86	6.88
L_ε_2 1st TP [mm]	4.72	5.02	6.07	6.40	6.47
L_ε_3 1st TP [mm]	4.39	4.45	5.21	5.988	6.05
L_ε_1 last TP [mm]	6.72	6.81	7.35	7.99	8.12
L_ε_2 last TP [mm]	5.97	6.12	6.77	6.98	7.00
L_ε_3 last TP [mm]	5.07	5.16	5.935	6.62	6.68

Table 9. Descriptive statistics of the absolute lengths (L) along DTI directions of the parallel and orthogonal infusions at first and last timepoint.

Parallel (Ω)	Minimum	25% Percentile	Median	75% Percentile	Maximum
Ω_ε_1 1st TP [°]	7.88	16.06	25.43	46.41	56.48
Ω_ε_2 1st TP [°]	60.56	65.84	78.56	83.3	87.77
Ω_ε_3 1st TP [°]	74.69	75.27	80.90	87.89	89.51
Ω_ε_1 last TP [°]	7.88	18.45	26.42	42.53	52.14
Ω_ε_2 last TP [°]	55.90	57.13	71.44	81.86	84.63
Ω_ε_3 last TP [°]	69.35	70.53	79.09	87.89	89.52
Orthogonal (Ω)	Minimum	25% Percentile	Median	75% Percentile	Maximum
Ω_ε_1 1st TP [°]	16.61	23.43	54.58	72.96	75.52
Ω_ε_2 1st TP [°]	32.36	36.51	56.17	77.75	82.82
Ω_ε_3 1st TP [°]	41.50	44.61	61.8	81.32	85.2
Ω_ε_1 last TP [°]	14.41	15.75	44.59	62.77	68.6
Ω_ε_2 last TP [°]	35.50	44.85	62.01	85.17	86.34
Ω_ε_3 last TP [°]	44.64	50.34	69.54	87.41	87.74

Table 10. Descriptive statistics of the angles between bolus PCA and each DTI principal components of the parallel and orthogonal infusions at first and last timepoint.

Off-target infusions

As reported above, four procedures resulted off the planned target: CED infusions were thus delivered laterally to the CST (Fig. 51B). At first timepoint, the length L_ε_1 of these boli (median=5.89 mm, range:[5.72-7.37]) is not statistically different from L_ε_2 (median=4.45 mm, range:[4.2-5.03]) and L_ε_3 (median=4.94, range:[4.94-5.19]) (L_ε_1 *vs* L_ε_2: *P=0.25,* L_ε_1 *vs* L_ε_3: *P=0.25*, Wilcoxon test). Boli remained rounded over all the consecutive timepoints, indeed at last timepoint the length L_ε_1 of these boli (median=7.13 mm, range:[6.12-8.03]) remains not statistically different from L_ε_2 (median=5.17 mm, range:[4.4-5.99]) and L_ε_3 (median=5.93 mm, range:[5.15-5.61]) (L_ε_1 *vs* L_ε_2: *P*=0.25, L_ε_1 *vs* L_ε_3: *P*=0.5, Wilcoxon test) (Tab.11).

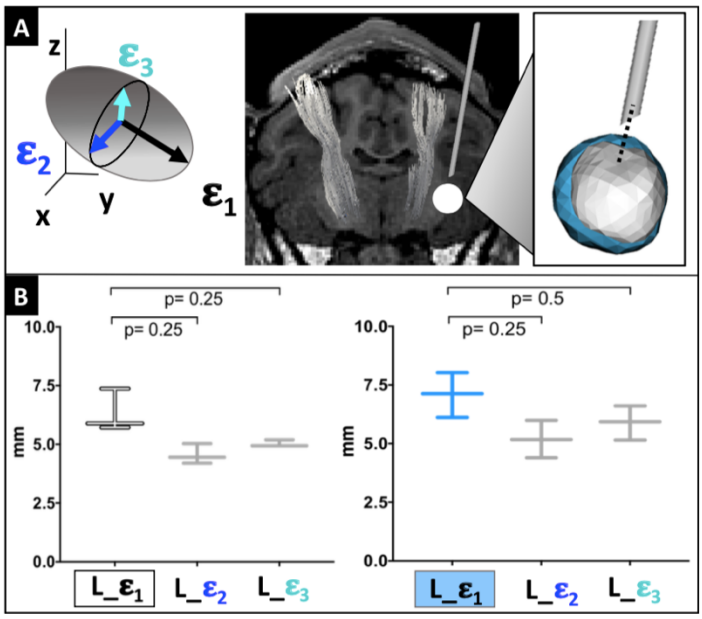

Figure 54. Infusion out of the CST (Sheep 8 left infusion). A) Representation of infusions outside the WM at first and last timepoints, which include DTI main directions, 3DT1 images with overlaid both the CSTs (in white), catheter (gray), bolus at 1st timepoint (white sphere) and bolus at last timepoint (light blue sphere). B) Non parametric 'Wilcoxon matched-pairs signed rank test' was performed for L_ε_1 *(white) with* L_ε_2 *and* L_ε_3 *(in gray) at 1st timepoint and* L_ε_1 *(light blue) with* L_ε_2 *and* L_ε_3 *(gray) at last timepoint.*

Off-Target	Minimum	25% Percentile	Median	75% Percentile	Maximum
L_ε_1 1st TP [mm]	5.72	5.72	5.89	7.37	7.37
L_ε_2 1st TP [mm]	4.2	4.2	4.45	5.03	5.03
L_ε_3 1st TP [mm]	4.94	4.94	4.94	5.19	5.19
L_ε_1 last TP [mm]	6.12	6.12	7.13	8.03	8.03
L_ε_2 last TP [mm]	4.4	4.4	5.17	5.99	5.99
L_ε_3 last TP [mm]	5.15	5.15	5.93	6.61	6.61

Table 11. Descriptive statistics of the absolute lengths (L) along DTI directions of the off-target infusions at first and last timepoint.

Discussion

Convection-enhanced delivery (CED) is an innovative technique for drug delivery directly into the human brain, bypassing the Blood-Brain-Barrier. CED aims to target pathological tissue of the CNS such as Parkinson's and Huntington's disease, epilepsy, brain tumors, and ischemic stroke. However due to lack of standardization of CED parameters such as appropriate needle diameter, flow rate, catheter positioning and patient-tailored protocols, CED based therapy has seen limited success. In this project, CED technique was exploited to target the CST of brain ovine animal at the level of internal capsule. The distribution of a known infusate at consecutive timepoints was compared to microstructural properties as depicted by DTI, demonstrating the impact of brain tissue features and catheter positioning on drug distribution *in vivo*.

Diffusion Tensor Imaging (DTI) successfully depicts microstructural properties of large animal model brain tissue *in-vivo* allowing reproducible tensor estimations as shown from previous study [148]. We prove the feasibility of a protocol to perform *in vivo* DTI tractography of the sheep model, providing a reliable reconstruction and 3D rendering of the cortical spinal tract (CST) with minimal inter-sheep variability. Further, the mean fractional anisotropy of the CST equal to (0.378 ± 0.026) was similar to what found by Pieri et al. in the same ovine models (0.483 ± 0.024). However small difference in mean fractional anisotropy of the CST may reflect different and limitative sample size. Furthermore, DTI-extracted parameters such as eigenvalue and eigenvector allow a DTI-based pre-surgical planning with different catheter placements in respect to WM fibers. Although accurate DTI-based presurgical planning, the difficulty of the surgical procedure leads to an included angle between catheter in parallel and orthogonal directions and underling fibers not actually completely 0° and 90° respectively (Fig.49) but still in a small range.

All animals successfully underwent MRI session and surgery procedure and no complications were met during CED infusion such as presence of air in the tip of the syringe. Particularly, backflow along the catheter, i.e. the tendency of the infusate to travel back up between the catheter and the tissue, was completely absent in parallel and orthogonal infusions likely due to low infusion rate (0.3 μL/min), small infusion inner silica diameter (0.3 mm) and WM high conductivity [14]. DTI images were corrected from eddy current and movement artefact and together with pre- and post-infusion 3D-T1 scans, intra-sheep images were aligned and normalized to a common baseline-intensity, to allow intra-sheep monitoring of infusate distribution over time. Interestingly, the absence of backflow allowed automatic infusion segmentation based on standardized parameters, leading to reproducible

analyses without any manual correction. In addition, inclusion criteria allowed to take into account only the boli that were within the CST, leading to replicable analyses. Infusions that were excluded from the inclusion criteria were analyzed distinctly.

Assessment of the impact of brain microstructural features, as depicted by DTI, on drug diffusion along the three principal WM directions was studied in this project. Results denote that brain tissue microstructure such as white and gray matter, may impact on drug volume of distribution within the brain. In agreement with past literature, analyses of ΔL along $\varepsilon 1$, $\varepsilon 2$, $\varepsilon 3$ during time of boli within CST demonstrate that microstructural constraints impact on drug diffusion, facilitating it along WM fiber main axial direction [38,100,103,109, 125-127] (Fig.47). This result is also supported by the absolute length and angles analysis showing lengthening and alignment of the infusate greater along $\varepsilon 1$ direction in respect to $\varepsilon 2$ and $\varepsilon 3$ directions. This preferentially flow path is related to the ordered arrangement of the myelinated fibers as well as microtubules and neurofilaments that behave as a barrier to diffusion in transverse direction (radial direction) while decrease hydraulic resistance in the fiber axial direction. Furthermore, axonal transport may accentuate diffusion along WM axial direction [38]. The relative contribution of these structures to anisotropy are not the same, indeed, the neural membranes are confirmed to be the primary determinant of anisotropic water diffusion while myelination can modulate the degree of anisotropy. All these characteristics confer to the WM a higher hydraulic conductivity in respect to the GM, allowing fluid flow preferentially along axons direction.

As shown by the explained variance (EV), catheter placed parallel to the WM fibers allows to the infusate to be more elongated in fiber axial direction than orthogonal one. Absolute lengths analysis in DTI main directions support previous results, in fact, infusions parallel to CST were already driven along fiber direction at the first timepoint, keeping expanding preferentially along ε1. Conversely, the convection exerted by infusions orthogonal to CST initially adversely impacts on the drug distribution along WM fibers, leading to smaller absolute lengths differences along the DTI principal directions than parallel infusions. Although parallel catheter placement with respect to CST fibers leads to a greater bolus elongation along $\varepsilon 1$ direction than orthogonal ones, their difference was not statistically different, thus demonstrating that microstructure effect is likely to be greater than catheter pose. Again, the trend appreciable in absolute lengths of orthogonal infusion might be due to the strongest effects of microstructure in comparison with the influences of catheter placement (Fig.50B). Although parallel catheter placement with respect to CST fibers leads to a greater alignment of boli with respect to fibers along $\varepsilon 1$ direction than orthogonal ones, the alignment between bolus and WM fibers in $\varepsilon 1$ direction ($\Omega\_\varepsilon 1$) for first and last timepoint for parallel and

orthogonal infusions within the CST became smaller over time (Fig.53), despite of their not statistically difference. Once again, the stronger trend in parallel than orthogonal infusions, suggests that catheter positioning influences drug distribution (Fig.52). However, the fact that *Ω_ε1* is lower than *Ω_ε2* and *Ω_ε3* in both parallel and orthogonal infusions, implies that microstructure effects is stronger than catheter orientation (Fig.52). Ultimately, considering infusions partially outside the WM, it is evident that boli expansion does not follow a preferential direction neither when stopping CED nor at consecutive timepoint (Fig.54).

All our findings are in agreement (*Ω, L and ΔL*), demonstrating a greater effect of hydraulic conductivity of microstructure in respect to advective bulk flow due to the pressure gradient of CED in WM infusions. Catheter orientations has only an influence in the initial drug distribution giving to the distribution of Gd-based solution a more elongated shape in the fiber main direction in case of parallel infusions, where convection effect may still play a role. Findings reported in this study may improve the treatment of various diseases, in particular brain tumor treatment that spreads along WM fibers. Brain tumor treatment using CED present difficult challenges due to tumor excessive vascularity and high interstitial fluid pressure (IFP) which in tumors is, on average, 50 times higher than normal brain tissue [2]. These tumor characteristics can result in the loss of infusate to circulation or outside the tumor. As shown in this investigation, parallel infusion, in which active CED pressure and WM fibers high hydraulic conductivity are acting synergistically may enhance the flow toward the WM longitudinal direction. In this concern, the combination of catheter placement parallel to white matter tract and the brain WM microstructure high conductivity may be used to improve the flow of the therapeutic agent in the axonal direction toward the tumor region exploiting inter or extra-tumoral infusions. Furthermore, drug molecules with high affinity, such as charge or surface proprieties, to the brain tumor tissue could slow down the rapid removal of drug from the tumor extracellular space, keeping the therapeutic drug inside the tumor for longer time and thus increasing its efficacy.

A potential limitation of this study can be represented by the restricted number of animals involved in the analyses. Nevertheless, considering that in vivo MRI studies on sheep are complex and demanding, as emphasized also by other reports [154,155], a sample size of 7 animals for a total of 14 infusions, may be considered valuable. Second, time acquisition of timepoint was not coherent for all the infusions and coherent timing between timepoint could likely leads to more robust results. However, first timepoints are all similar in a time acquisition range of 20 minutes and therefore they are more standard than last timepoint that present a more spread acquisition time across infusions. DTI spatial resolution also may influence accuracy of the results, considering that tractography is

based on DTI voxel approximately 2 x 2 x 2 mm^3, while WM fiber diameter is typically less than 10 μm. A further limit is associated with clinically compatible magnetic resonance imaging with a 1.5T scanner, which may hinder the representation of fine anatomical details of the tracts. More recent studies have used 3T scanner for the elaboration of tractography of WM tracts of large animal models [153,154]. However, nowadays, mainly because of the disproportionate costs compared to the clinical routine of veterinary practice, 3T MR scanners fully dedicated to veterinary imaging are rarely available in Italy and Europe. Another source of error might be the loss of intracerebral pressure due to surgery that leads to a brain shift causing little errors in images coregistration. However, the likelihood of coregistration errors due to animal brain shift are smaller than susceptibility artifacts that would be present in a second DTI image acquisition after surgery due to possible peri-catheter small hemorrhages caused by catheter insertion, and paramagnetic effects of gadolinium contrast agent. Nevertheless, in our study, high quality images and clinically compatible scanning were obtained. Finally, our results are relative to gadolinium-based solution and, as known, diffusion parameters change in respect to size, charge and other drug characteristics.

Future investigations will be aimed at exploring microstructural and catheter placements effects under different initial CED technical constraints such as *infusion rate* or the *volume of infusion* in order to understand if the effects of both microstructure and catheter placements are dependent on technical CED parameters and if both the effects are equally important to model drug distribution within the brain or if one effect can be neglected compared to the other. Further, different kind of therapeutics must be experimentally tested in order to understand how catheter placement and microstructure effects are related to the drugs characteristics such as size, charge etc. Finally, MRI diffusion tensor data are not always in agreement with experimental observations due to the lack of accuracy of Gaussian diffusion model of water in brain tissue [160]. Therefore, future investigation must take into account diffusion non-gaussianity in order to obtain reliable predictions that can be used in the clinic. In this way brain microstructure such as restriction and hindrance of brain tissue will be taken into account allowing better pre-surgical planning and future drug distribution prediction in mathematical models.

Conclusion

Diffusion Tensor Imaging (DTI) successfully depicts microstructural properties of large animal model brain tissue *in-vivo* allowing reproducible tensor estimations and a DTI-based pre-surgical planning with different catheter placements in respect to WM fibers. Our findings report a major impact of WM microstructure in respect to catheter placement on Gadolinium-based solution distribution delivered by CED technique. However, the catheter placement seems to have an impact at the beginning of the infusions especially in parallel infusion. Knowledge of these properties before applying CED may result essential to plan optimal catheter positioning before surgery on an individual patient basis and to more accurately predict final drug distribution in future computational modeling, leading to an improvement of CED in the clinics. Drug distribution in both parallel and orthogonal infusions with respect to the CST is preferentially elongated in WM main direction providing that microstructure effect is strongest than the effect of catheter placement in this setting.

References

1) Anoop P Patel, James L Fisher et al., Global, regional, and national burden of brain and other CNS cancer, 1990–2016: a systematic analysis for the Global Burden of Disease Study 2016, The Lancet Neurology, Volume 18, Issue 4, 2019, Pages 376-393,ISSN 1474-4422.
2) Ryuta Saito, Teiji Tominaga, Convection-Enhanced Delivery: From Mechanisms to Clinical Drug Delivery for Diseases of the Central Nervous System, Neurologia medico-chirurgica, 2012, Volume 52, Issue 8, Pages 531-538, Released August 24, 2012, Online ISSN 1349-8029, Print ISSN 0470-8105, https://doi.org/10.2176/nmc.52.531.
3) Bobo RH, Laske DW, Akbasak A, Morrison PF, Dedrick RL, Oldfield EH: Convection-enhanced delivery of macromolecules in the brain. Proc Natl Acad Sci USA 91: 2076–2080, 1994
4) Antonella Castellano, Lorenzo Bello, Caterina Michelozzi, Marcello Gallucci, Enrica Fava, Antonella Iadanza, Marco Riva, Giuseppe Casaceli, Andrea Falini, Role of diffusion tensor magnetic resonance tractography in predicting the extent of resection in glioma surgery, Neuro-Oncology, Volume 14, Issue 2, February 2012, Pages 192–202,
5) O. Bottema & B. Roth (1990). Dover Publications. reface. ISBN 0-486-66346-9.
6) Mark Jenkinson, Stephen Smith, A global optimisation method for robust affine registration of brain images,Medical Image Analysis,Volume 5, Issue 2,2001,Pages 143-156,ISSN 1361-8415,
7) J. P. W. Pluim, J. B. A. Maintz and M. A. Viergever, "Mutual-information-based registration of medical images: a survey," in IEEE Transactions on Medical Imaging, vol. 22, no. 8, pp. 986-1004, Aug. 2003. doi: 10.1109/TMI.2003.815867
8) Gadolinium-Based Contrast Agent Accumulation and Toxicity: An Update X J. Ramalho, X R.C. Semelka, X M. Ramalho, X R.H. Nunes, M. AlObaidy, and X M. Castillo
9) Traficante DD. Relaxation. Can T2 be longer than T1? Concepts Magn Reson 1991; 3:171-177.
10) Hennig J, Nauerth A, Friedburg H. RARE imaging - a fast imaging method for clinical MR. Magn Reson Med 1986; 3: 823-833.
11) Engelhard HH: The role of interstitial BCNU chemotherapy in the treatment of malignant glioma. Surg Neurol 53: 458–464, 2000
12) Krauze MT, Saito R, Noble C, Tamas M, Bringas J, Park JW, Berger MS, Bankiewicz K: Reflux-free cannula for convection-enhanced high-speed delivery of therapeutic agents. J Neurosurg 103: 923–929, 2005
13) Linninger AA XM: Drug delivery into the human 2009 brain. Drug Delivery 1985: 163–168, 2001
14) Raghavan R, Brady ML, Rodriguez-Ponce MI, Har- tlep A, Pedain C, Sampson JH: Convection-enhanced delivery of therapeutics for brain disease, and its optimization. Neurosurg Focus 20(4): E12, 2006
15) Murad GJ, Walbridge S, Morrison PF, Szerlip N, But- man JA, Oldfield EH, Lonser RR: Image-guided con- vection-enhanced delivery of gemcitabine to the brainstem. J Neurosurg 106: 351–356, 2007
16) Heiss JD, Walbridge S, Asthagiri AR, Lonser RR: Im- age-guided convection-enhanced delivery of mus- cimol to the primate brain. J Neurosurg 112: 790–795, 2010

17) Jahangiri, A., Chin, A. T., Flanigan, P. M., Chen, R., Bankiewicz, K., & Aghi, M. K. (2017). Convection-enhanced delivery in glioblastoma: a review of preclinical and clinical studies, Journal of Neurosurgery JNS, 126(1), 191-200. Retrieved Jul 25, 2019
18) Sillay KA, McClatchy SG, Shepherd BA, Venable GT, Fuehrer TS. Image-guided convection-enhanced delivery into agarose gel models of the brain. J Vis Exp 2014(87).
19) White E, Bienemann A, Malone J, Megraw L, Bunnun C, Wyatt M, et al. An evaluation of the relationships between catheter design and tissue mechanics in achieving high-flow convection-enhanced delivery. J Neurosci Methods. 2011; 199:87–97. [PubMed: 21549753]
20) Chen MY, Hoffer A, Morrison PF, Hamilton JF, Hughes J, Schlageter KS, Lee J, Kelly BR, Oldfield EH: Surface properties, more than size, limiting con- vective distribution of virus-sized particles and viruses in the central nervous system. J Neurosurg 103: 311–319, 2005
21) MacKay JA, Deen DF, Szoka FC Jr: Distribution in brain of liposomes after convection enhanced deliv- ery; modulation by particle charge, particle diameter, and presence of steric coating. Brain Res 1035: 139–153, 2005
22) Saito R, Krauze MT, Noble CO, Tamas M, Drum- mond DC, Kirpotin DB, Berger MS, Park JW, Bankie- wicz KS: Tissue affinity of the infusate affects the dis- tribution volume during convection-enhanced deliv- ery into rodent brains: implications for local drug delivery. J Neurosci Methods 154: 225–232, 2006
23) Mehta AI, Choi BD, Ajay D, et al. Convection enhanced delivery of macromolecules for brain tumors. Curr Drug Discov Technol 2012;9:305–310.
24) Raghavan R, Brady ML, Rodriguez-Ponce MI, Hartlep A, Pedain C, Sampson JH. Convection-enhanced delivery of therapeutics for brain disease, and its optimization. Neurosurg Focus 2006;20: E12.
25) Jain RK: Delivery of novel therapeutic agents in tumors: physiological barriers and strategies. J Natl Cancer Inst 81:570–576, 1989
26) Journal ArticleT, Convection-Enhanced Delivery A Mehta, A. M.A Sonabend, A. M.A Bruce, J. N J Neurotherapeutics 2017
27) Jahangiri A, Chin AT, Flanigan PM, Chen R, Bankiewicz K, Aghi MK. Convection-enhanced delivery in glioblastoma: a review of preclinical and clinical studies. J Neurosurg. 2017;126(1):191–200. doi:10.3171/2016.1.JNS151591
28) Yun J, Rothrock RJ, Canoll P, Bruce JN. Convection-enhanced delivery for targeted delivery of antiglioma agents: the translation- al experience. J Drug Deliv 2013;2013:107573.
29) Sonabend AM, Stuart RM, Yun J, et al. Prolonged intracerebral convection-enhanced delivery of topotecan with a subcutaneously implantable infusion pump. Neuro Oncol 2011;13:886–893.
30) Bleicher AG, and Kanal E. A serial dilution study of gadolinium-based MR imaging contrast agents. AJNR 2008
31) Deligianni, Fani et al. "NODDI and Tensor-Based Microstructural Indices as Predictors of Functional Connectivity." PloS one vol. 11,4 e0153404. 14 Apr. 2016, doi:10.1371/journal.pone.0153404
32) Burdette JH, Elster AD, Ricci PE. Acute cerebral infarction: quantification of spin-density and T2 shine-through phenomena on diffusion-weighted MR images. Radiology 1999; Aug;212(2):333-9.
33) Provenzale JM, Sorensen AG. Diffusion-weighted MR imaging in acute stroke: theoretic considerations and clinical applications. AJR Am J Roentgenol 1999; Dec;173(6):1459-67.

34) Le Bihan D, Breton E, Lallemand D, Grenier P, Cabanis E, Laval-Jeantet M. MR imaging of intravoxel incoherent motions: application to diffusion and perfusion in neurologic disorders. Radiology 1986; Nov;161(2):401-7.
35) Damion RA, Vennart W, Summers IR, Ellis RE. Water diffusion coefficient measurements in the finger by magnetic resonance imaging. Magn Reson Imaging 1994;12(6):873-9.
36) Melhem ER, Mori S, Mukundan G, Kraut MA, Pomper MG, van Zijl PC. Diffusion tensor MR imaging of the brain and white matter tractography. AJR Am J Roentgenol 2002; Jan;178(1):3-16.
37) Le Bihan D, Turner R, Douek P, Patronas N. Diffusion MR imaging: clinical applications. AJR Am J Roentgenol 1992; Sep;159(3):591-9.
38) Beaulieu C. The basis of anisotropic water diffusion in the nervous system - a technical review. NMR Biomed 2002; Nov-Dec;15(7-8):435-55.
39) Le Bihan D, Mangin JF, Poupon C, Clark CA, Pappata S, Molko N, et al. Diffusion tensor imaging: concepts and applications. J Magn Reson Imaging 2001; Apr;13(4):534-46.
40) Basser PJ, Pierpaoli C. Microstructural and physiological features of tissues elucidated by quantitative-diffusion-tensor MRI. J Magn Reson B 1996; Jun;111(3):209-19.
41) Basser PJ, Pajevic S, Pierpaoli C, Duda J, Aldroubi A. In Vivo Fiber Tractography Using DT–MRI Data. Magnetic Resonance in Medicine. 2000;44:625–632.
42) Pierpaoli C, Jezzard P, Basser PJ, Barnett A, Di Chiro G. Diffusion tensor MR imaging of the human brain. Radiology 1996; Dec;201(3):637-48.
43) Kingsley, P. B. (2006), Introduction to diffusion tensor imaging mathematics: Part I. Tensors, rotations, and eigenvectors. Concepts Magn. Reson., 28A: 101-122.
44) Pajevic S, Pierpaoli C. Color schemes to represent the orientation of anisotropic tissues from diffusion tensor data: application to white matter fiber tract mapping in the human brain. Magnetic Resonance in Medicine 2000. 1999;42:526–540.
45) Ulug AM, van Zijl PC. Orientation-independent diffusion imaging without tensor diagonalization: anisotropy definitions based on physical attributes of the diffusion ellipsoid. J Magn Reson Imaging 1999; Jun;9(6):804-13.
46) Douek P, Turner R, Pekar J, Patronas N, Le Bihan D. MR color mapping of myelin fiber orientation. J Comput Assist Tomogr 1991; Nov-Dec;15(6):923-9.
47) Pajevic S, Pierpaoli C. Color schemes to represent the orientation of anisotropic tissues from diffusion tensor data: application to white matter fiber tract mapping in the human brain. Magn Reson Med 1999; Sep;42(3):526-40.
48) Stejskal EO, Tanner JE. Spin diffusion measurements: spin echoes in the presence of a time-dependent field gradient. J Chem Phys 1965;42:288-92.
49) Mukherjee P, McKinstry RC (2006) Diffusion tensor imaging and tractography of human brain development. Neuroimaging Clin N Am 16:19–43, vii
50) Mori S, Crain BJ, Chacko VP, van Zijl PC. Three-dimensional tracking of axonal projections in the brain by magnetic resonance imaging. Ann Neurol 1999; Feb;45(2):265-9.
51) Xue R, van Zijl PC, Crain BJ, Solaiyappan M, Mori S. In vivo three- dimensional reconstruction of rat brain axonal projections by diffusion tensor imaging. Magn Reson Med 1999; Dec;42(6):1123-7.

52) Stieltjes B, Kaufmann WE, van Zijl PC, Fredericksen K, Pearlson GD, Solaiyappan M, et al. Diffusion tensor imaging and axonal tracking in the human brainstem. Neuroimage 2001; Sep;14(3):723-35.
53) Mori S, Kaufmann WE, Davatzikos C, Stieltjes B, Amodei L, Fredericksen K, et al. Imaging cortical association tracts in the human brain using diffusion-tensor- based axonal tracking. Magn Reson Med 2002; Feb;47(2):215-23.
54) Mori S, Wakana S, Nagae-Poetscher LM, van Zijl PCM. MRI Atlas of Human White Matter. Elsevier; 2005.
55) Conturo TE, Lori NF, Cull TS, Akbudak E, Snyder AZ, Shimony JS, et al. Tracking neuronal fiber pathways in the living human brain. Proc Natl Acad Sci U S A 1999; Aug 31;96(18):10422-7.
56) Mori S, Frederiksen K, van Zijl PC, Stieltjes B, Kraut MA, Solaiyappan M, et al. Brain white matter anatomy of tumor patients evaluated with diffusion tensor imaging. Ann Neurol 2002; Mar;51(3):377-80.
57) Wiegell MR, Larsson HB, Wedeen VJ. Fiber crossing in human brain depicted with diffusion tensor MR imaging. Radiology 2000; Dec;217(3):897-903.
58) Alexander AL, Hasan KM, Lazar M, Tsuruda JS, Parker DL. Analysis of partial volume effects in diffusion-tensor MRI. Magn Reson Med 2001; May;45(5):770-80.
59) Basser PJ, Jones DK. Diffusion-tensor MRI: theory, experimental design and data analysis - a technical review. NMR Biomed 2002; Nov-Dec;15(7-8):456-67.
60) Woods RP, Mazziotta JC, Cherry SR. MRI-PET registration with automated algorithm. J Comput Assist Tomogr 1993; Jul-Aug;17(4):536-46.
61) Jones DK, Horsfield MA, Simmons A. Optimal strategies for measuring diffusion in anisotropic systems by magnetic resonance imaging. Magn Reson Med 1999; Sep;42(3):515-25.
62) Papadakis NG, Xing D, Huang CL, Hall LD, Carpenter TA. A comparative study of acquisition schemes for diffusion tensor imaging using MRI. J Magn Reson 1999; Mar;137(1):67-82.
63) Spees WM, Buhl N, Sun P et al. Quantification and compensation of eddy-current-induced magnetic-field gradients. J Magn Reson 2011; 212:116-23.
64) Reese, T.G., Heid, O., Weisskoff, R.M., Wedeen, V.J., 2003. Reduction of eddy-current-induced distortion in diffusion MRI using a twice- refocused spin echo. Magn. Reson. Med. 49 (1), 177–182.
65) Chenevert, T.L., Pipe, J.G., 1991. Effect of bulk tissue motion on quantitative perfusion and diffusion magnetic resonance imaging. Magn. Reson. Med. 19 (2), 261–265.
66) Pipe, Jim. (2009). Pulse Sequences for Diffusion-Weighted MRI. 10.1016/B978-0-12-374709-9.00002-X.
67) Chien, D., Buxton, R.B., Kwong, K.K., Brady, T.J., Rosen, B.R., 1990. MR diffusion imaging of the human brain. J. Comput. Assist. Tomogr. 14 (4), 514–520.
68) Buonocore M.H., Gao L., Ghost artifact reduction for echo planar imaging using image phase correction. Magn Reson Med 1997; 38: 89-100.
69) Mansfield P. Snap-shot MRI. Nobel Lecture, 8 Dec 2003 from www.nobelprize.org Mansfield P. Multi-planar image formation using NMR spin echoes. J Phys C: Solid State Phys 1977; 10:L55-L58.
70) Elster AD. Sellar susceptibility artifacts: theory and implications. AJNR Am J Neuroradiol 1993; 14:129-136. (Explains the physical basis of an artifact at the skull base that can mimic a pituitary adenoma).

71) Schenck JF. The role of magnetic susceptibility in magnetic resonance imaging: MRI magnetic compatibility of the first and second kinds. Med Phys 1996;23:815-850. (Slightly dated, but an excellent and enduring explanation of susceptibility from a pioneer in MRI and first inductee in GE's Genius Hall of Fame).
72) [Andersson 2003] J.L.R. Andersson, S. Skare, J. Ashburner. How to correct susceptibility distortions in spin-echo echo-planar images: application to diffusion tensor imaging. NeuroImage, 20(2):870-888, 2003.
73) Seo, Young-Eun et al. "Nanomaterials for convection-enhanced delivery of agents to treat brain tumors." Current opinion in biomedical engineering 4 (2017): 1-12 .
74) Muti, Marco. (2014). Studio della riproducibilità in un protocollo fMRI su tomografo da 3 Tesla. 10.13140/2.1.4059.3925.
75) K. Jones, Derek. (2009). Gaussian Modeling of the Diffusion Signal. 10.1016/B978-0-12-374709-9.00003-1.
76) Carpenter, M. B. (1995). Fondamenti di neuroanatomia. Edises, 88-7959-056-1;
77) Fitzgerald, M. J. T. (2012). Neuroanatomia con riferimenti funzionali e clinici, Elsevier Masson, 9788821432712
78) Perentos, N., Nicol, A.U., Martins, A.Q., Stewart, J.E., Taylor, P., and Morton, A.J. (2017). Techniques for chronic monitoring of brain activity in freely moving sheep using wireless EEG recording. J Neurosci Methods279,87-100.
79) Finnie, J. (2001). Animal models of traumatic brain injury: a review. Aust Vet J79,628-633.
80) Morosanu, C.O., Nicolae, L., Moldovan, R., Farcasanu, A.S., Filip, G.A., and Florian, I.S. (2019). Neurosurgical cadaveric and in vivo large animal training models for cranial and spinal approaches and techniques - a systematic review of the current literature. Neurol Neurochir Pol53,8-17.
81) Stypulkowski, P.H., Stanslaski, S.R., Jensen, R.M., Denison, T.J., and Giftakis, J.E. (2014). Brain stimulation for epilepsy--local and remote modulation of network excitability. Brain Stimul7,350-358.
82) Nestler, E.J., and Hyman, S.E. (2010). Animal models of neuropsychiatric disorders. Nat Neurosci13,1161-1169.
83) Dai, J.X., Ma, Y.B., Le, N.Y., Cao, J., and Wang, Y. (2018). Large animal models of traumatic brain injury. Int J Neurosci128,243-254.
84) Karageorgos, L., Hein, L., Rozaklis, T., Adams, M., Duplock, S., Snel, M., Hemsley, K., Kuchel, T., Smith, N., and Hopwood, J.J. (2016). Glycosphingolipid analysis in a naturally occurring ovine model of acute neuronopathic Gaucher disease. Neurobiol Dis91,143-154.
85) Murray, S.J., Black, B.L., Reid, S.J., Rudiger, S.R., Simon Bawden, C., Snell, R.G., Waldvogel, H.J., and Faull, R.L.M. (2019). Chemical neuroanatomy of the substantia nigra in the ovine brain. J Chem Neuroanat97,43-56.
86) Reid, S.J., Mckean, N.E., Henty, K., Portelius, E., Blennow, K., Rudiger, S.R., Bawden, C.S., Handley, R.R., Verma, P.J., Faull, R.L.M., Waldvogel, H.J., Zetterberg, H., and Snell, R.G. (2017). Alzheimer's disease markers in the aged sheep (Ovis aries).Neurobiol Aging58,112-119.
87) Capitanio, J.P., and Emborg, M.E. (2008). Contributions of non-human primates to neuroscience research. Lancet371,1126-1135.
88) Jacqmot, O., Van Thielen, B., Fierens, Y., Hammond, M., Willekens, I., Van Schuerbeek, P., Verhelle, F., Goossens, P., De Ridder, F., Clarys, J.P., Vanbinst, A., and De Mey, J. (2013).

Diffusion tensor imaging of white matter tracts in the dog brain. Anat Rec (Hoboken)296,340-349.

89) Anaya Garcia, M.S., Hernandez Anaya, J.S., Marrufo Melendez, O., Velazquez Ramirez, J.L., and Palacios Aguiar, R. (2015). In vivo study of cerebral white matter in the dog using diffusion tensor tractography. Vet Radiol Ultrasound56,188-195.

90) John, S.E., Lovell, T.J.H., Opie, N.L., Wilson, S., Scordas, T.C., Wong, Y.T., Rind, G.S., Ronayne, S., Bauquier, S.H., May, C.N., Grayden, D.B., O'brien, T.J., and Oxley, T.J. (2017). The ovine motor cortex: A review of functional mapping and cytoarchitecture. Neurosci Biobehav Rev80,306-315.

91) Nucifora, Paolo G. P. et al. "Diffusion-tensor MR imaging and tractography: exploring brain microstructure and connectivity." Radiology 245 2 (2007): 367-84 .

92) Masutani Y, Aoki S, Abe O, Hayashi N, Otomo K. MR diffusion tensor imaging: re- cent advance and new techniques for diffu- sion tensor visualization. Eur J Radiol 2003; 46:53– 66.

93) Okada T, Miki Y, Fushimi Y, et al. Diffu- sion-tensor fiber tractography: intraindi- vidual comparison of 3.0-T and 1.5-T MR imaging. Radiology 2006;238:668 – 678.

94) D. C. Alexander, C. Pierpaoli, P. J. Basser and J. C. Gee, "Spatial transformations of diffusion tensor magnetic resonance images," in IEEE Transactions on Medical Imaging, vol. 20, no.11, pp. 1131-1139, Nov. 2001.doi: 10.1109/42.963816.

95) J.E. Tanner E.O. Stejskal. Spin diffusion measurements: spin echoes in the presence of a time-dependent field gradient. Journal of Chemical Physics, 42:288–292, 1965.

96) P. F. Morrison, M. Y. Chen, R. S. Chadwick, R. R. Lonser, and E. H. Oldfield, "Focal delivery during direct infusion to brain : Role of flow rate, catheter diameter, and tissue mechanics," Amer. J. Physiol., vol. 277, pp. R1218–1229, 1999.

97) M. Sarntinoranont, R. K. Banerjee, R. R. Lonser, and P. F. Morrison, "A computational model of direct infusion of macromolecules into the spinal cord," Ann. Biomed. Eng., vol. 31, pp. 3217–335, 2003.

98) Y. Zhang, J. Luck, M. W. Dewhirst, and F. Yuan, "Interstitial hydraulic conductivity in a fibrosarcoma," Amer. J. Physiol. Heart Circulat. Phys-iol., vol. 279, pp. H2726–H2734, 2000.

99) Johansen-Berg, H., and T. E. J. Behrens. Diffusion MRI. London, UK: Academic Press, 2009.

100) Sykova, E., and C. Nicholson. Diffusion in brain extra- cellular space. Physiol. Rev. 88(4):1277–1340, 2008.

101) Geer, C. P., and S. A. Grossman. Interstitial fluid flow along white matter tracts: a potentially important mecha- nism for the dissemination of primary brain tumors. J. Neurooncol. 32(3):193–201, 1997.

102) Wood, J. D., R. R. Lonser, N. Gogate, P. F. Morrison, and E. H. Oldfield. Convective delivery of macromolecules into the naive and traumatized spinal cords of rats. J. Neuro- surg. 90(1):115–120, 1999.

103) Morrison, Paul Frederick et al. "High-flow microinfusion: tissue penetration and pharmacodynamics." The American journal of physiology 266 1 Pt 2 (1994): R292-305 .

104) Gill SS, Patel NK, Hotton GR, et al. Direct brain infusion of glial cell line-derived neurotrophic factor in Parkinson disease. Nat Med 2003;9:589–595.

105) Tsujiuchi T, Natsume A, Motomura K, et al. Preclinical evaluation of an O(6)-methylguanine-DNA methyltransferase-siRNA/liposome complex administered by convection-enhanced delivery to rat and porcine brains. Am J Transl Res. 2014;6(2):169–178. Published 2014 Jan 15

106) Raghu Raghavan and Martin Brady 2011 Quantifying Fluid Infusion and Tissue Expansion in Brain Phys. Med. Biol. 56 6179
107) Reulen H J, Graham R, Spatz M and Katzo I 1977 Role of pressure gradients and bulk flow in dynamics of vasogenic brain edema J. Neurosurg. 46 24–35
108) Sarntinoranont M, Banerjee A, Lonser R R and Morrison P F 2003b A computational model of direct interstitial infusion of macromolecules into the spinal cord Ann. Biomed. Eng. 31-448 61
109) Kim, Jung Hwan et al. "Voxelized computational model for convection-enhanced delivery in the rat ventral hippocampus: comparison with in vivo MR experimental studies." Annals of biomedical engineering vol. 40,9 (2012): 2043-58.
110) Sato Y, Murase K, Kato J, Kobune M, Sato T, Kawano Y, Takimoto R, Takada K, Miyanishi K, Matsunaga T, Takayama T, Niitsu Y. Resolution of liver cirrhosis using vitamin A-coupled liposomes to deliver siRNA against a collagen-specific chaperone. Nat Biotechnol. 2008;26:431–442
111) Lidar Z, Mardor Y, Jonas T, et al. Convection-enhanced delivery of paclitaxel for the treatment of recurrent malignant glioma: a phase I/II clinical study. J Neurosurg 2004;100:472–479.
112) Lopez KA, Tannenbaum AM, Assanah MC, et al. Convection-enhanced delivery of topotecan into a PDGF-driven model of glioblastoma prolongs survival and ablates both tumor-initiating cells and recruited glial progenitors. Cancer Res 2011;71:3963–3971.
113) Ung TH, Malone H, Canoll P, Bruce JN. Convection-enhanced delivery for glioblastoma: targeted delivery of antitumor therapeutics. CNS Oncol 2015;4:225–234.
114) Sampson JH, Archer G, Pedain C, et al. Poor drug distribution as a possible explanation for the results of the PRECISE trial. J Neurosurg 2010;113:301–309.
115) Mueller S, Polley MY, Lee B, et al. Effect of imaging and catheter characteristics on clinical outcome for patients in the PRECISE study. J Neurooncol 2011;101:267–277.
116) Bruce JN, Fine RL, Canoll P, et al. Regression of recurrent malignant gliomas with convection-enhanced delivery of topotecan. Neurosurgery 2011;69:1272–1279.
117) Laske DW, Youle RJ, Oldfield EH. Tumor regression with regional distribution of the targeted toxin TF-CRM107 in patients with malignant brain tumors. Nat Med 1997;3:1362–1368.
118) Duke Today. Poliovirus vaccine trial shows early promise for recurrent glioblastoma. Medicine, Academics, Research. Available at: https://today.duke.edu/2013/07/poliovirus-vaccine-trial-shows-promise-recurrent-glioblastoma. Accessed February 26, 2017.
119) Van der Bom IMJ, Moser RP, Gao G, et al 'Frameless multimodal image guidance of localized convection-enhanced delivery of therapeutics in the brain' Journal of NeuroInterventional Surgery 2013;5:69-72.
120) Le Bihan D: Molecular diffusion, tissue microdynamics and microstructure. NMR Biomed 1995, 8(7–8):375–386.
121) Background Information on GDNF – a timeline: Parkinson's Disease Foundation. Available at: http://www.pdf.org/en/science_news/release/pr_1216665220. Accessed June 26, 2016.
122) De Nunzio G, Cataldo R, Carlà A. Robust Intensity Standardization in Brain Magnetic Resonance Images. J Digit Imaging. 2015;28(6):727–737. doi:10.1007/s10278-015-9782-8
123) Lee W, Lee SD, Park MY, et al. Functional and diffusion tensor magnetic resonance imaging of the sheep brain. BMC Vet Res. 2015;11:262. Published 2015 Oct 14. doi:10.1186/s12917-015-0581-8
124) Messaritaki E, Rudrapatna SU, Parker GD, Gray WP, Jones DK. Improving the Predictions of Computational Models of Convection-Enhanced Drug Delivery by Accounting for Diffusion

Non-gaussianity. Front Neurol. 2018;9:1092. Published 2018 Dec 18. doi:10.3389/fneur.2018.01092
125) Chen MY, Lonser RR, Morrison PF, Governale LS, Oldfield EH: Variables affecting convection-enhanced delivery to the striatum: a systematic examination of rate of infusion, cannula size, infusate concentration, and tissue- cannula sealing time. J Neurosurg 90:315–320, 1999
126) Lonser RR, Gogate N, Morrison PF, Wood JD, Oldfield EH: Direct convective delivery of macromolecules to the spinal cord. J Neurosurg 89:616–622, 1998
127) Lonser RR, Weil RJ, Morrison PF, Governale LS, Oldfield EH: Direct convective delivery of macromolecules to peripheral nerves. J Neurosurg 89:610–615, 1998
128) Singleton WG, Collins AM, Bienemann AS, et al. Convection enhanced delivery of panobinostat (LBH589)-loaded pluronic nano-micelles prolongs survival in the F98 rat glioma model. Int J Nanomedicine. 2017;12:1385–1399. Published 2017 Feb 21. doi:10.2147/IJN.S125300
129) Endo, T., Fujii, Y., Sugiyama, S., Zhang, R., Ogita, S., Funamoto, K., Saito, R., & Tominaga, T. (2016). Properties of convective delivery in spinal cord gray matter: laboratory investigation and computational simulations, Journal of Neurosurgery: Spine SPI, 24(2), 359-366. Retrieved Sep 18, 2019
130) Brian M. Dale, Mark A. Brown, and Richard C. Semelka. 2015. MRI: Basic Principles and Applications (5th ed.). Wiley Publishing.
131) Jim Pipe,Chapter 2 - Pulse Sequences for Diffusion-Weighted MRI,Editor(s): Heidi Johansen-Berg, Timothy E.J. Behrens,Diffusion MRI (Second Edition),Academic Press,2014, Pages 11-34.
132) Traficante, D. D. (1991), Relaxation. Can T2, be longer than T1?. Concepts Magn. Reson., 3: 171-177. doi:10.1002/cmr.1820030305
133) The Basics of MRI, Joseph P. Hornak, Ph.D.
134) Nuclear magnetic resonance and its applications to living systems, D.G. Gadian 1982.
135) Principles, Techniques, and Application of T2*-based MR Imaging and Its Special Applications. Govind B. Chavhan, Paul S. Babyn, Bejoy Thomas, Manohar M. Shro□, E. Mark Haacke. 5, 2009, RadioGraphics, Vol. 29, pp. 1433-1449.
136) Elster AD. An index system for comparative parameter weighting in MR imaging. J Comput Assist Tomogr 1988; 12:130-134.
137) Bottomley PA, Foster TH, Argersinger RE, Pfeiffer LM. A review of normal tissue hydrogen NMR relaxation times and relaxation mechanisms from 1–100 MHz: Dependence on tissue type, NMR frequency, temperature, species, excision, and age. Med Phys 1984;11:425-448.
138) Plewes DB. Contrast mechanisms in spin-echo MR imaging. Radiographics 1994:14:1389-1404.
139) Nitz WR, Reimer P. Contrast mechanisms in MR imaging. Eur Radiol 1999;9:1032-1046. Perman WH, Hilal SK, Simon HE, Maudsley AA. Contrast manipulation in NMR imaging. Magn Reson Imaging 1984; 2:23-32.
140) Rohrer M, Bauer H, Mintorovitch J, et al. Comparison of magnetic properties of MRI contrast media solutions a different magnetic field strengths. Invest Radiol 2005; 40:715-724.
141) Lomax, R. G., & Hahs-Vaughn, D. L. (2012). Statistical concepts: A second course (4th ed.). New York, NY, US: Routledge/Taylor & Francis Group.
142) Le Bihan D (2003) Looking into the functional architecture of the brain with diffusion MRI. *Nat Rev Neurosci* **4**: 469-480
143) Thomsen C, Henriksen O, & Ring P (1987) In vivo measurement of water self-diffusion in the human brain by magnetic resonance imaging. *Acta Radiol* **28**: 353-361
144) Basser PJ, Mattiello J, & LeBihan D (1994a) Estimation of the effective self-diffusion tensor from the NMR spin echo. *J Magn Reson B* **103**: 247-254

145) Basser PJ, Mattiello J, & LeBihan D (1994b) MR diffusion tensor spectroscopy and imaging. *Biophys J* **66**: 259-267
146) Le Bihan D, Mangin JF, Poupon C, Clark CA, Pappata S, Molko N, & Chabriat H (2001) Diffusion tensor imaging: concepts and applications. *J Magn Reson Imaging* **13**: 534-546
147) Mori S & van Zijl PC (2002) Fiber tracking: principles and strategies - a technical review. *NMR Biomed* **15**: 468-480
148) Pieri Valentina, Trovatelli Marco, Cadioli Marcello, Zani Davide Danilo, Brizzola Stefano, Ravasio Giuliano, Acocella Fabio, Di Giancamillo Mauro, Malfassi Luca, Dolera Mario, Riva Marco, Bello Lorenzo, Falini Andrea, Castellano Antonella. In vivo Diffusion Tensor Magnetic Resonance Tractography of the Sheep Brain: An Atlas of the Ovine White Matter Fiber Bundles , Frontiers in Veterinary Science,VOLUME=6, 2019, DOI=10.3389/fvets.2019.00345, ISSN=2297-1769
149) Mori, S., Xue, R., Crain, B.J., Solaiyappan, M., Chacko, V.P., & Zijl, P.C. 3d Reconstruction of Axonal Fibers from Diffusion Tensor Imaging Using Fiber Assignment by Continuous Tracking (fact).
150) Linninger AA, Somayaji MR, Erickson T, Guo X, Penn RD: Computational methods for predicting drug transport in anisotropic and heterogeneous brain tissue. J Biomech 41:2176–2187, 2008;
151) Rosenbluth KH, Eschermann JF, Mittermeyer G, Thomson R, Mittermeyer S, Bankiewicz KS: Analysis of a simula- tion algorithm for direct brain drug delivery. Neuroimage 59:2423–2429, 2012
152) Sarntinoranont M, Iadarola MJ, Lonser RR, Morrison PF: Direct interstitial infusion of NK1-targeted neurotoxin into the spinal cord: a computational model. Am J Physiol Regul Integr Comp Physiol 285:R243–R254, 2003
153) Wright AK, Theilmann RJ, Ridgway SH, Scadeng M. Diffusion tractography reveals pervasive asymmetry of cerebral white matter tracts in the bottlenose dolphin (Tursiops truncatus). Brain Struct Funct. (2018) 223:1697–711. doi: 10.1007/s00429-017-1525-9
154) Lee W, Lee SD, Park MY, Foley L, Purcell-Estabrook E, Kim H, et al. Functional and diffusion tensor magnetic resonance imaging of the sheep brain. BMC Vet Res. (2015) 11:262. doi: 10.1186/s12917-015-0581-8
155) Dai JK, Wang SX, Shan D, Niu HC, Lei H. A diffusion tensor imaging atlas of white matter in tree shrew. Brain Struct Funct. (2017) 222:1733–51. doi: 10.1007/s00429-016-1304-z
156) GBD 2015 Neurological Disorders Collaborator Group, Global, regional, and national burden of neurological disorders during 1990–2015: a systematic analysis for the Global Burden of Disease Study 2015. Lancet Neurol. 2017; 16: 877-897
157) Global, regional, and national burden of brain and other CNS cancer, 1990–2016: a systematic analysis for the Global Burden of Disease Study 2016, Patel, Anoop P et al., The Lancet Neurology, Volume 18, Issue 4, 376 - 393
158) Reardon DA, Rich JN, Friedman HS, Bigner DD. Recent advances in the treatment of malignant astrocytoma. J Clin Oncol 2006;24:1253–1265.
159) Stine Caleb A., Munson Jennifer M.,Convection-Enhanced Delivery: Connection to and Impact of Interstitial Fluid Flow, Frontiers in Oncology, Volume 9, 2019; 2234-943X.
160) Messaritaki E, Rudrapatna SU, Parker GD, Gray WP and Jones DK (2018) Improving the Predictions of Computational Models of Convection-Enhanced Drug Delivery by Accounting for Diffusion Non-gaussianity. Front. Neurol. 9:1092. doi: 10.3389/fneur.2018.01092
161) Ferlay J, Colombet M, Soerjomataram I, Mathers C, Parkin DM, Piñeros M, et al. Estimating the global cancer incidence and mortality in 2018: GLOBOCAN sources and methods. Int J Cancer. 2019;144(8):1941–53.